

Engineering Nanoparticulate Antigens for Enhanced Follicular Accumulation and Immunogenicity

By

Benjamin J. Read

B.S. Bioengineering

University of Washington, Seattle, 2015

SUBMITTED TO THE HARVARD-MIT DIVISION OF HEALTH SCIENCES AND TECHNOLOGY IN PARTIAL FULFILLMENT OF THE REQUIREMENTS FOR THE DEGREE OF

DOCTOR OF PHILOSOPHY IN MEDICAL ENGINEERING AND MEDICAL PHYSICS
AT THE
MASSACHUSETTS INSTITUTE OF TECHNOLOGY

JUNE 2021

©2021 Massachusetts Institute of Technology. All rights reserved.

The author hereby grants MIT permission to reproduce and to distribute publicly paper and electronic copies of this thesis document in whole or in part in any medium now known or hereafter created.

Signature of Author: _____
Harvard-MIT Division of Health Sciences and Technology
May 24, 2021

Certified by: _____
Darrell J. Irvine, PhD
Professor of Biological Engineering and Materials Science & Engineering
Thesis Supervisor

Accepted by: _____
Emery N. Brown, MD, PhD
Director, Harvard-MIT Program in Health Sciences and Technology
Professor of Computational Neuroscience and Health Sciences and Technology

Engineering Nanoparticulate Antigens for Enhanced Follicular Accumulation and Immunogenicity

By

Benjamin J. Read

Submitted to the Harvard-MIT Division of Health Sciences and Technology on May 24, 2021, in partial fulfillment of the requirements for the degree of Doctor of Philosophy in Medical Engineering and Medical Physics

ABSTRACT

In vaccine design, antigens are often arrayed in a multivalent nanoparticle form, but *in vivo* mechanisms underlying the enhanced immunity elicited by such vaccines remain poorly understood. In this thesis, we began by examining two model, HIV-immunogen-bearing nanoparticles that displayed an unusually high degree of immunogenicity. We found that these nanoparticles accumulated selectively within the follicular dendritic cell network of draining lymph nodes, and discovered that this trafficking pattern was dependent on complement recognition mediated by mannose-binding lectin (MBL) binding to glycans on the surface of the nanoparticles. Accumulation within follicles was positively associated with multiple immune response outputs. Trafficking was found to occur in a variety of nanoparticles of different sizes and compositions, and the primary factor that allowed for trafficking to occur was the presence of high-mannose glycans on the surface of the nanoparticles. Several clinically-relevant nanoparticle antigens were also found to traffic in an MBL-dependent fashion, suggesting that this mechanism could be utilized to improve the efficacy of a variety of important nanoparticulate antigens. We also utilized DNA origami nanoparticles as a model system to probe critical parameters of nanoparticle vaccine design, including antigen density, antigen spacing, nanoparticle geometry, and overall antigen concentration. Initial *in vivo* studies are described, as are suggestions for future experiments to further the design and functionality of these particles for vaccination. Overall, these studies have elucidated a number of design principles that should aid in the engineering of next generation vaccines to provide protection against a variety of possible pathogens.

Thesis Supervisor: Darrell J. Irvine

Title: Professor of Biological Engineering and Materials Science & Engineering

Acknowledgments

This thesis and the work described within it are the results of help and support from a wide range of people who have contributed in a variety of ways, both big and small, to helping me grow and develop as a person and a researcher over the years.

Firstly, I would like to thank Darrell, who has been an incredible thesis advisor and mentor during my years of graduate school. Darrell has consistently provided feedback, advice, and motivation as I've struggled through my research, and during times when the research path forward was unclear he was always able to help me find a direction forward. His support and willingness to let me explore independently have been foundational, and I cannot imagine having completed this work without him.

My thesis committee, Sangeeta Bhatia and Facundo Batista, have also been instrumental in the completion of this thesis. They routinely provided useful advice and suggestions that influenced the direction of this work and its presentation, and I am extremely grateful for their willingness to lend their time and energy to supporting me.

Since joining the Irvine lab in late 2016, I have been surrounded by a group of friendly people all eager to conduct research and help others do the same. Thank you Aereas Aung, Anasuya Mandal, Andrew Zmolek, Angela Zhang, Anna Romanov, Archana Boopathy, Ashely Lemnios, Ayush Thomas, B.J. Kim, Ben Cossette, Bingxu Liu, Brittany Hartwell, Chensu Wang, Chris Jones, Coralie Backlund, Dan Garafola, Eric Dane, Hannah Watkins, Heikyung Suh, Ina Sulkaj, Ivan Susin Pires, Jake Martin, Jason Chang, Joesetta Adams, Kaiyuan Ni, Kavya Rakhra, Kelly Moynihan, Kristen Rodrigues, Laura Maiorino, Lauren Milling, Leyuan Ma, Libin Zhang, Luciano Santollani, Mariane Melo, Mariann Murray, Mark Miller, Martin Kraemer, Maurice Bukenya, Michael Fichter, Murillo Silva, Na Li, Nathan Donahue, Naveen Mehta, Nikki Thai, Nitasha Bennett, Ozgun Kocabiyik, Parastoo Amlashi, Parisa Yousefpour, Ryan Hosn, Sabrina Yang, Sasan Jalili Firoozinezhad, Sachin Bhagchandani, Shengwei Wu, Shuhao Xiao, Simon Liang, Sudha Kumari, Talar Tokatlian, Tanaka Remba, Tanmay Dichwalkar, Tyson Moyer, Val Corapie, Wuhbet Abraham, Yash Agarwal, and Yingzhong Li for all that you have done/are still doing to make the Irvine lab the welcoming, fun, and energizing environment it is, both inside the lab and at critical research meetings.

There are a few people that I wanted to single out for their contributions to my research and growth during my graduate works. Talar and Chris took me under their wings during my first months in the lab and helped get me on my feet, teaching me many of the fundamental techniques that I've used for years. Jason and Aereas have both helped a great deal microscopy over the years, for which I am very grateful. Eric at multiple times was willing to provide help by rapidly synthesizing nanoparticles when reviewers were unforgiving with the timetables they set. Dan would often come and stare at me while I was trying to work, but he made up for this by providing beautiful original pieces of art and placing them around the lab without anyone's permission or request. Coralie taught me the joys of HPLC, of which there are very few, but it's been a useful skill to know nonetheless. Lori Won, an undergraduate I had the privilege to work with for the past two years, was a pleasure to work with and often helped keep me focused with her keen questions and discussion about our research and miscellany in general.

I have also been fortunate to work with several fantastic research collaborators. Thank you to Mark Bathe, Eike-Christian Wamhoff, Grant Knappe, Neil King, Jake Kraft, Isaac Sappington, and Bill Schief for being willing to let me share in our exciting discoveries together. In particular, I'd like to thank Eike for his indomitably cheerful disposition and willingness to brainstorm on topics even beyond the scope of our collaboration.

I never would have made it to graduation, let alone to graduate school in the first place, without the support of my family. Thank you to Mom, Dad, Matt, Kristine, Dan, Arundhati, Edwin,

Lisa, and Chris (and Othello, Ophelia, Cordelia, and Toi) for the constant love. I can't wait to see everyone again soon.

For the last ~2.5 years or so I've been a GRA in Simmons, one of the undergraduate dorms on campus. It has been an incredibly fun and rewarding experience, and I'm grateful to both my fellow members of the house team for being a wonderful group of people to work with and to the residents, who are an amazing group of people that would often infect me with their boundless enthusiasm and excitement for the world.

Friends beyond the Irvine lab have been an enormous support during the last six years. Thank you to Ryan, Kait, Kamran, Erin, Jerry, Michael, Mel, Dan, Joanna, Engi, Chauncey, and Cate for helping to remind me that there is a whole wide world outside of lab. You all helped immeasurably to keep me from tunneling on research and to keep me sane, especially during the pandemic. Special thanks to Takeshi Hongo and his eyebrows for providing the perfect role model of a person and scientist.

I would also like to acknowledge all of the animals used in my studies throughout graduate school. Their bodies and lives were used to advance our scientific knowledge and hopefully save lives in the future, and I am extremely grateful.

Last but certainly not least, I have been exceedingly lucky to get to go through graduate school with an incredible partner by my side. Thank you so much to Melisa, for celebrating my successes, sympathizing with my failures, unconditional support and understanding during the weeks of 12-hour days, listening to me sing when I didn't feel like going in to lab, and all around being just about the best stand-up gal anyone could hope to marry. I love you, toots.

Table of Contents

Title Page	1
Abstract	2
Acknowledgments	3
Chapter 1: Introduction	7
1.1 Vaccines in health	7
1.2 Hurdles to the creation of an HIV-1 vaccine.....	9
1.3 Lessons learned from efforts to create an HIV-1 vaccine.....	11
1.4 Rationale for nanoparticle vaccine formulations.....	14
1.5 Motivation and thesis overview	17
Chapter 2: Investigation of the efficacy of nanoparticulate HIV immunogens	19
2.1 Introduction.....	19
2.2 Nanoparticulate HIV immunogens elicit strong antigen-specific immune responses	20
2.3 Nanoparticulate HIV immunogens selectively accumulate within draining lymph node follicles.....	22
2.4 Follicular trafficking of nanoparticles is complement dependent.....	26
2.5 <i>In vitro</i> complement deposition on nanoparticles is dependent on binding of mannose- binding lectin	29
2.6 Deglycosylation of eOD-60mer leads to decreased MBL recognition	30
2.7 Follicular trafficking of nanoparticles is dependent on MBL recognition.....	34
2.8 Immune responses to nanoparticle immunogens correlate with follicular trafficking.....	36
2.9 Discussion	38
2.10 Materials and methods	39
Chapter 3: Assessment of generalizability of MBL-mediated nanoparticle trafficking	49
3.1 Introduction.....	49
3.2 Generation and investigation of differentially glycosylated eOD-60mers.....	49
3.3 MD39-bearing liposomes traffic to lymph node follicles.....	53
3.4 Development and analysis of mannosylated, non-antigen-bearing nanoparticles	54
3.5 <i>In vitro</i> MBL binding to serially mannosylated nanoparticles	57
3.6 Trafficking and immunogenicity of HA-8mer nanoparticles.....	58
3.7 Trafficking and immunogenicity of HPV16 L1 and HBsAg AD nanoparticles.....	60
3.8 Discussion	63
3.9 Materials and methods	65

Chapter 4: DNA origami for probing of nanoparticle vaccine design parameters	71
4.1 Introduction.....	71
4.2 <i>In vitro</i> validation of eOD-conjugated DNA nanoparticles.....	72
4.3 Activation of B cells by varied nanostructures	74
4.4 Antigen density dependence of <i>in vitro</i> antigen-specific B cell activation	77
4.5 Effects of stabilization and antigen attachment method on B cell activation	79
4.6 Preliminary <i>in vivo</i> studies of eOD-conjugated DNA nanoparticles	82
4.7 <i>In vitro</i> validation of peptide-conjugated DNA nanoparticles	86
4.8 Discussion	87
4.9 Materials and methods	89
Chapter 5: Conclusion and future work	96
Appendix	98
eOD-GT8 amino acid sequence	98
eOD-60mer amino acid sequence	99
eOD-GT8-PADRE amino acid sequence	100
p5 amino acid sequence.....	101
p31 amino acid sequence.....	102
Lymph node solvent-based clearing protocol.....	103
Bilayer interferometry protocol	106
Calcium flux assay protocol	109
References	111

1. Introduction

1.1 Vaccines in Health

Vaccines are a cornerstone of modern public health, and the development of vaccines against endemic pathogens has had a major impact on global mortality and morbidity from infectious diseases¹. Many of the great terrors of only a span of decades ago, such as polio² and measles³, have seen their prevalence dramatically reduced, while the once widespread smallpox has been successfully eradicated in nature⁴. While it can be disheartening to see antivax sentiments continuing to be propagated, the track record of vaccination is quite clear. Compared to rates prior to the introduction of vaccines against hepatitis A, acute hepatitis B, varicella, and Haemophilus influenzae type B, total cases as well as mortality have been reduced by more than 80%⁵. Few other health interventions can boast of such a track record, and this past success provides impetus for the continued research and development of vaccines against other clinically-relevant infectious diseases.

Vaccines function by exposing the immune system to antigens, molecules that are usually part of or made by pathogenic viruses or organisms. When immune cells encounter these antigens and are stimulated by danger signals, an adaptive immune response begins. B cells will begin to rapidly divide and undergo somatic hypermutation to create a diverse pool of potential antibodies. B cells mutate their antigen receptor in a specialized site within the lymph nodes termed the germinal center, which form within lymph node follicles. These B cells then migrate into contact with follicular dendritic cells (FDCs), which display captured antigens on their surface. The mutated B cell receptors then have an opportunity to bind with the captured antigens, and depending on the affinity of the binding interaction the B cell will either undergo apoptosis or receive survival signals from a follicular helper T cell (T_{fh} cell). When one of these B cell receptors is found to have a high affinity for the antigen, that B cell will begin dividing and producing mature antibodies as a plasma cell⁶⁻⁹ (Figure 1). Should a pathogen bearing the original pathogen then

infect the host, the pre-existing antibodies will enable a rapid secondary immune response to clear the pathogen efficiently. By tricking the immune system into thinking it was infected during vaccination, the morbidities and mortalities that can be caused by a primary infection of the real pathogen can be avoided.

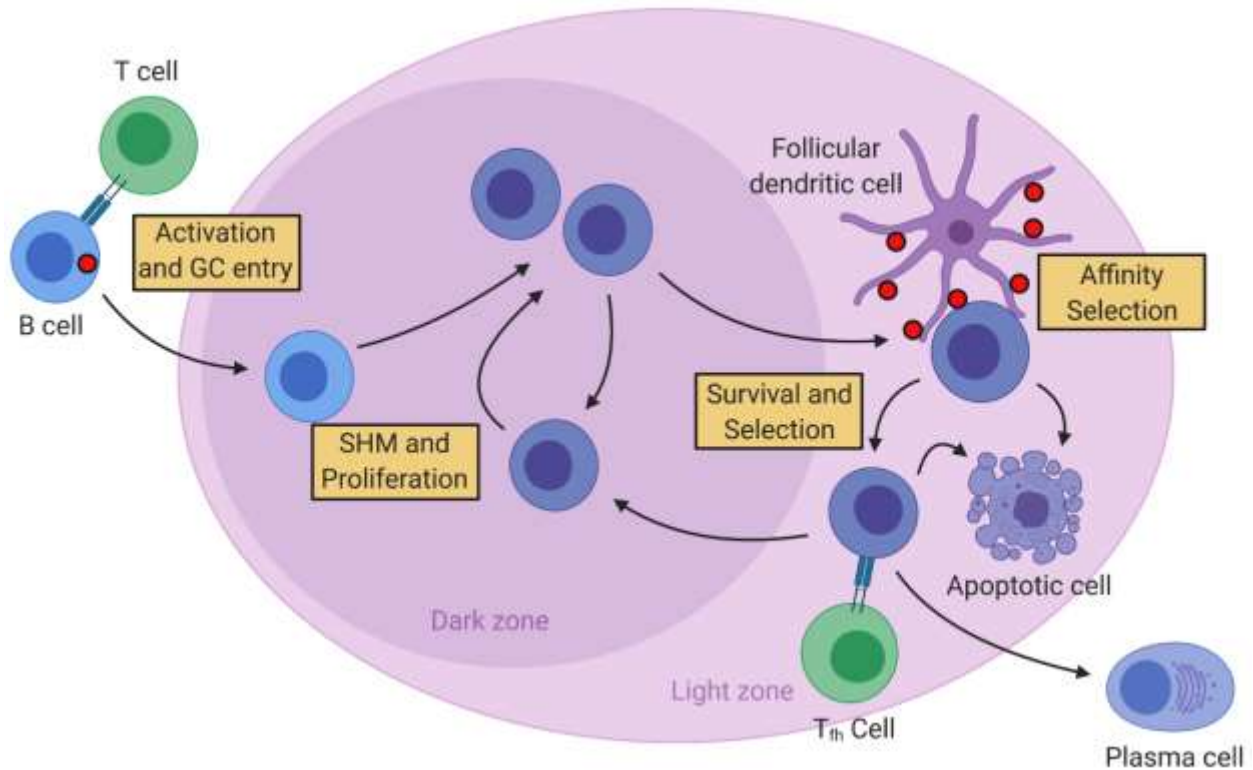


Figure 1. Schematic of the germinal center reaction. After encountering an antigen for which its BCR has some affinity, naïve B cells are activated with T cell help and begin to form a germinal center (GC) by rapidly dividing and undergoing somatic hypermutation (SHM). B cells will periodically test their B cell receptors against antigen immobilized on follicular dendritic cells. B cells with high affinity receptors receive survival signals from follicular helper T cells (T_h cells) and exit the GC as antibody producing plasma cells.

The majority of vaccines in use today were developed prior to the fruition of immunology as a field and were created in an empiric manner. Such vaccines primarily utilize live attenuated pathogens, whole killed pathogens, or pathogen toxoids and were discovered through relatively

simple inoculation studies¹⁰. These early vaccines were followed by the subunit class of vaccines, consisting of a recombinantly produced protein or polysaccharides from a pathogenic organism. Together, these classes make up nearly all clinically used vaccines today. In only the last few years, several new vaccine technologies have begun to appear in clinical use, most notably the SARS-CoV-2 mRNA vaccines¹¹.

Though vaccines have had a major impact in reducing mortality and morbidity against diseases against which they were developed, there are far more potentially vaccinatable diseases than there are clinically used vaccines. In the United States, there are currently FDA approved vaccines against only 27 different pathogens. The reasons for this are multifaceted and are influenced by scientific, regulatory, and fiscal factors¹²⁻¹⁶. Despite the many barriers to creating new vaccines, much research is ongoing in this area, with a significant portion of the overall vaccine development effort focusing on the creation of a vaccine to protect against HIV-1.

1.2 Hurdles to the creation of an HIV-1 vaccine

Despite the recent focus on the ongoing SARS-Cov-2 pandemic, HIV-1 has been pandemic across the globe for decades and is responsible for a large morbidity and mortality burden¹⁷. Major strides in prevention, treatment, education and destigmatization have helped to make the disease manageable in areas with sufficient health infrastructure, but many of the regions of the world most heavily affected lack this infrastructure¹⁸. Without drastic economic and policy changes, the prospect of ending the pandemic in these regions of high burden with current technologies is daunting. In a parallel effort to combat the disease, much energy has been focused on creating a protective vaccine against HIV-1, and it is now a commonly held notion that such a vaccine will be a necessity for ending the pandemic¹⁹.

The development of such a vaccine, however, has been challenging for a number of reasons. Many of these challenges are rooted in the molecular structure of the HIV-1 virion; HIV-1 is an enveloped virus consisting of host cellular membrane, and the only viral protein present

on the surface is the gp160 glycoprotein spike, making it the primary viable target for any antibody-based protective immunity^{20,21}. This protein, however, is quite resistant to being effectively targeted by antibodies. Possibly the most difficult barriers to overcome are the rapid mutation rate of HIV and the relatively small number of conserved regions on gp160. These two facts mean that antibodies developed naturally during the course of an infection are specific against only a small subset of viral variants within an infected individual²². In order to elicit a humoral immune response that is protective against a wide range of HIV-1 strains, broadly neutralizing antibodies that target one of the few conserved regions on gp160 are required^{23,24}. This reality prevents simple killed virus or subunit vaccines from reliably providing broad protection, as was seen during several of the first clinical trials of candidate HIV-1 vaccines^{25,26}.

Other factors of gp160 glycoprotein biology make it a difficult antigen for the generation of a broadly neutralizing response. gp120, the outer portion of the greater gp160 glycoprotein spike, has a large degree of conformational flexibility²⁷. This flexibility necessitates that any antibody recognition of this domain must first overcome major entropic barriers and be precisely matched to target sites, a phenomenon that is uncommon in the germline B cell receptor repertoire^{28,29}. Other, non-neutralizing epitopes often have a smaller mutational requirement for antibody recognition and can be especially plentiful due to the poor stability of the envelope trimer, which can lead to the production of breakdown products that present distracting targets for immune recognition³⁰. Additionally, gp160 is heavily glycosylated, with more than 50% of its mass coming from glycans across its surface³¹. These glycans can mask more immunogenic protein surface underneath, providing a physical barrier between antibodies and their target sites³². Finally, the low density of gp160 on the surface of HIV-1 virions is unfavorable for activation of B cells, which often requires B cell receptor crosslinking as observed in the case of other viruses such as influenza and polio³³⁻³⁵.

These numerous barriers to the creation of a protective gp160-based vaccine echo hurdles seen in the development of vaccines against other pathogens^{36,37}, and have necessitated research in antigen design, formulation, and delivery to discover a reliable method to generate broadly neutralizing antibodies. Through investment in research to develop methods and technologies to create a clinically-viable HIV-1 vaccine, a great deal of fundamental knowledge within the field of vaccine development as a whole has been derived.

1.3 Lessons learned from efforts to create an HIV-1 vaccine

Due to the aforementioned barriers to using native gp160 or whole virions for vaccination against HIV-1, efforts to develop a protective vaccine have by necessity focused on presenting either modified HIV immunogens or native HIV immunogens displayed to the immune system in unique ways. These efforts have taught the field of vaccinology as a whole a great deal about how similar techniques could be utilized against other pathogens as well.

A prevalent theme among candidate vaccination strategies for HIV-1 is the necessity of sequential immunizations to achieve protective immunity. Due to the large number of immunogenic but non-neutralizing epitopes on native HIV-1 gp160 trimers, immunizing with only these glycoproteins or recombinantly expressed versions fails to elicit the required broadly neutralizing antibody responses³⁸⁻⁴¹. Instead, if immunogens that are progressively more native-like and share the same conserved, broadly neutralizing epitope are delivered in series, the developing antibody responses can be groomed, hopefully resulting in antibodies that are more and more similar to clinically-isolated broadly neutralizing antibodies⁴²⁻⁴⁸ (Figure 2).

In such a serial vaccination scheme, the first immunogen must be recognized by germline (i.e. unmutated) B cell receptors with similarities to known broadly neutralizing antibodies. However, for many broadly neutralizing epitopes on the virus, the associated B cell receptors do not have measurable affinities for gp140 or gp160 trimer, indicating the large amount of somatic hypermutation required for broadly neutralizing antibodies to be developed⁴⁹. It is therefore

necessary to design the initial immunogen specifically so that it can engage with these populations of germline B cells, expanding their population and mutational space to prepare for the next antigen. Several such germline-targeting HIV-1 antigens, including the engineered outer domain of gp120 (eOD), have been developed and have been shown to expand the desired B cell populations in humanized mouse models⁵⁰⁻⁵³.

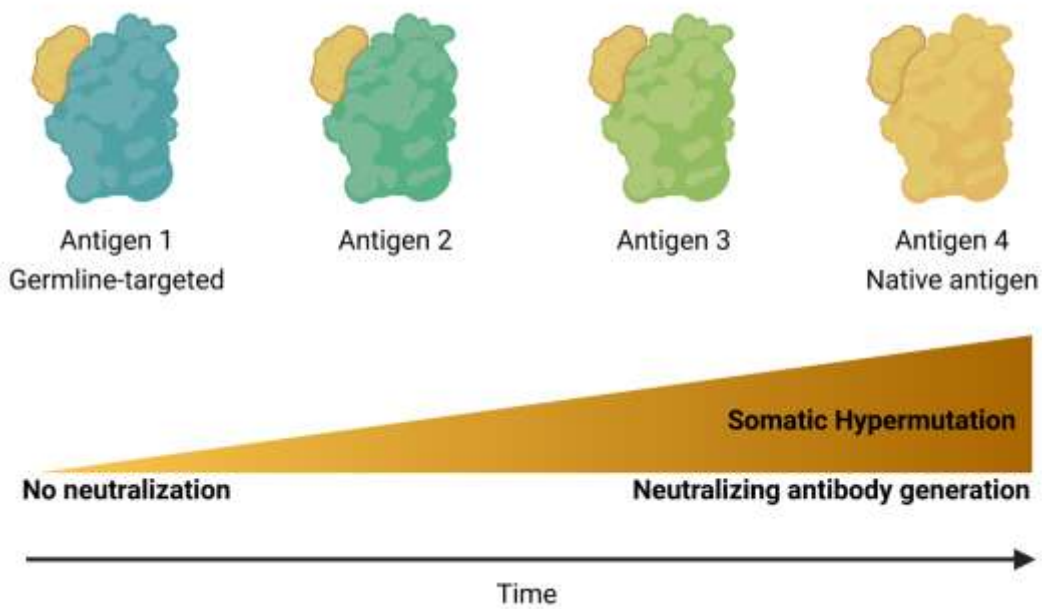


Figure 2. Schematic of a sequential immunization. A sequential immunization scheme would begin with an antigen designed to target germline B cell receptors in a naïve host containing a neutralizing epitope (tan). After allowing for time and the generation of B cells specific against this first antigen, a second antigen is injected, this one containing the same or similar neutralizing epitope on a different, more native-like protein scaffold. The B cells previously primed will be more likely to reform germinal centers, as their B cells receptors will have some affinity for the conserved epitope. This sequential immunization process is repeated until B cell maturation has been sufficiently guided that a final immunization with a native antigen will lead to the formation of antibodies specific against the neutralizing epitope when displayed on the native antigen, leading to the formation of efficacious neutralizing antibodies.

Since native gp160 does not elicit broadly neutralizing antibodies targeted to one of the few conserved epitopes on the glycoprotein, numerous iterations of different antigen designs have been created. One promising class is the recombinant native gp120 trimer family of immunogens, which retain many of the conserved, broadly neutralizing antibody target epitopes of native HIV-1 trimers⁵⁴. This direction of research has led to several related branches of modified HIV trimer immunogens, including BG505 SOSIPs, stabilized gp140 trimers that retain conformations thought to match the native viral spike in a stable, soluble glycoprotein form⁵⁵⁻⁵⁸. SOSIP trimers have continued to be refined over the years, resulting in more stable trimers, such as BG505 MD39 (MD39), that have fewer non-neutralizing epitopes present^{59,60}.

In addition to the rational design of novel antigens, the route of delivery and timing of administration has been a research focus in the HIV-1 vaccine field as well. Most vaccines currently in the clinical utilize a one-time bolus injection of antigen to induce a response, but this type of immunization may fail to recapitulate immune responses during infections, in which the pathogenic organism provides a continuous source of intact, nondegraded antigen over the course of days to weeks⁶¹⁻⁶³. The importance of intact antigen is particularly important in the case of HIV-1 immunogens, since degraded or misfolded antigen can sometimes be immunodominant and elicit off-target antibody responses⁶⁴. By delivering antigen slowly, through a series of exponentially-increasing immunizations or continuous release via osmotic pumps, immune responses against HIV-1 immunogens can be significantly enhanced^{65,66}. However, these strategies suffer from the need for either an implantable depot of antigen or numerous injections over only a few days, both of which limit their potential clinical feasibility.

One effective method for improving the humoral response to HIV-1 immunogens has been to display them on the surface of nanoparticles. This strategy has been taken with several different immunogens. eOD can be recombinantly expressed connected with lumazine synthase, a protein that self-assembles into a 60 subunit homomultimer, to form the aptly named eOD-60mer. This

particle has been found to be significantly more immunogenic than monomer eOD^{51,67,68}. Similarly, MD39 has been recombinantly expressed connected to ferritin, a protein that self-assembles into a 24 subunit homomultimer, to form the similarly aptly named MD39-8mer with eight copies of the full MD39 trimer displayed on the particle surface. Again, this particle has been shown to be more immunogenic than soluble MD39 trimer^{69,70}. While these studies present individual cases in which nanoparticulate display of antigen enhance immunogenicity, there is a wealth of literature highlighting way in which this type of formulation can be beneficial in vaccine design.

1.4 Rationale for nanoparticle vaccine formulations

Vaccine-elicited immunity is impacted by a number of factors, including the use of adjuvants, choice of immunization regimens, and structural design of the immunogen. One particularly effective strategy for enhancing humoral responses is via formulation of antigens in a multivalent particulate structure, mimicking the structure of a virus. Nanoparticle vaccines have a number of theoretical advantages for immune stimulation relative to soluble immunogens, including enhanced lymphatic trafficking, increased capture in lymph nodes by antigen presenting cells, and increased activation of antigen-specific B cells through receptor crosslinking⁷¹ (Figure 3). Formation of particulate antigens can be achieved by fusing immunogens to a protein that undergoes self-assembly with other subunits to form a nanoparticle, or through chemical linkage to synthetic lipid vesicles, polymer particles, or other inert materials. Vaccine nanoparticles are typically designed with diameters or ~100 nm or smaller, as particles in this size range exhibit effective drainage from injection sites into lymphatic vessels for enhanced trafficking to draining lymph nodes^{71,72}. Particulate formulation has a demonstrated track record of efficacy in humans, as demonstrated by the licensed human papillomavirus and hepatitis B virus vaccines, which are based on virus-like particle immunogens.

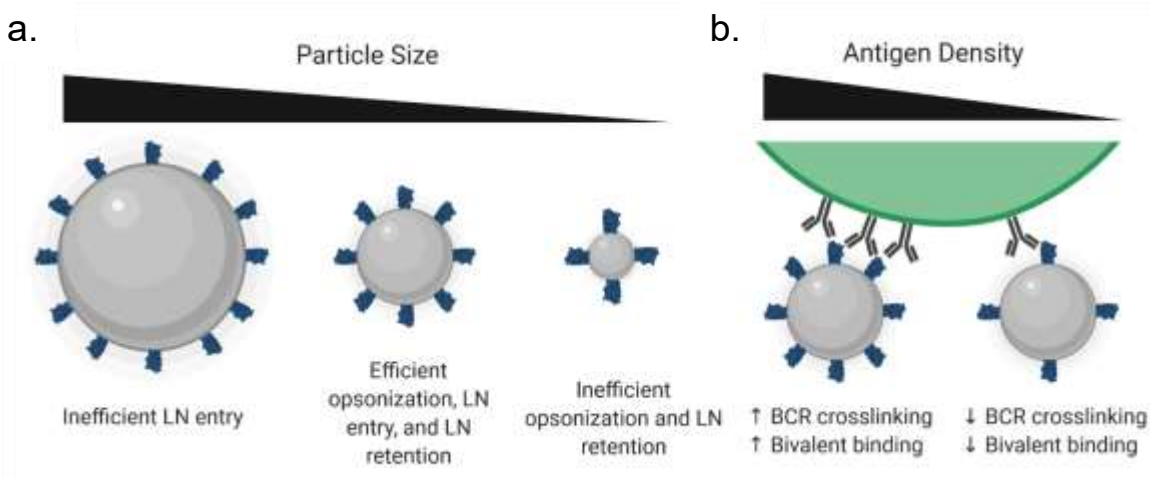


Figure 3. Impact of nanoparticle design on *in vivo* fate. **a** Small nanoparticles and monomeric antigens are often inefficiently opsonized and have poor retention within lymph nodes, while large nanoparticles are unable to effectively enter lymph nodes. Nanoparticles of an intermediate size (20-100 μm) are often able to be opsonized effectively while also entering and being retained in lymph nodes. **b** A high density of antigen on a particle surface can enhance B cell receptor crosslinking, activating B cells more strongly, while a low density of antigen on a particle surface or monomeric antigen is unable to crosslinking receptors, resulting in weaker B cell activation.

Display of immunogens in a dense array on the surface of a particle is often effective at increasing their immunogenicity. For example, minimal peptide immunogens that elicit poor humoral responses due to rapid clearance *in vivo* and lack repetitive epitopes have been demonstrated to generate strong antigen-specific antibody responses when multimerized on a particle scaffold^{73,74}. Nanoparticle display also enhances responses to T-independent immunogens, as demonstrated in the case of pneumococcal glycans; their delivery on gold nanoparticles or liposomes leads to robust class-switched antibody responses in mice^{75,76}.

Nanoparticle scaffolds can also increase the stability of immunogens and maintain desired epitope conformations. Fusion of HIV glycoprotein trimer subunits with self-assembling protein scaffolds has been successfully employed to ensure the antigen maintains the correct conformation^{69,77,78}. Stabilizing an antigen on a particle scaffold can also prevent off-target responses against artificial or undesirable epitopes, helping to focus the immune response on the

antigenic site of interest⁷⁹. In the case of transmembrane antigens, an engineered lipid bilayer can be used to maintain the native conformation of an antigen that would otherwise be unstable *in vivo*^{80,81}.

Details of how antigen is arrayed are important in shaping the humoral response to nanoparticle vaccines. High antigen surface density appears to be important. Particles displaying antigen at a spacing allow bivalent recognition by an individual B cell receptor increasing binding avidity⁷⁸. Using a modular multicomponent protein nanoparticle system, it was shown that antigen density correlated with neutralizing responses to a respiratory syncytial virus immunogen in mice, with optimal particles also eliciting strong neutralizing responses in non-human primates⁸². Similarly, dense multimerization of engineered HIV envelope trimers on liposomes has been shown to enhance triggering of antigen-specific B cells^{79,83}. Nanoparticle display has also been shown to impact humoral responses in non-human primates^{74,84}. In some cases, nanoparticle immunization is able to elicit antibody and germinal center responses in non-human primates in as little as seven days following immunization⁸⁵.

Nanoparticle carriers also enable multiple antigens to be displayed simultaneously to a single B cell. For example, presentation of multiple strains of influenza hemagglutinin in close proximity on a single nanoparticle favors the expansion of B cells that recognize epitopes conserved between the distinct strains, promoting neutralizing antibody breadth⁸⁶. Sequential immunization with liposomes bearing a series of HIV trimers or mixtures of trimers as heterologous boosts was similarly able to elicit antibodies exhibiting broad neutralization in rabbits⁸⁷.

A challenge particularly for protein nanoparticles is the development of strong humoral responses against the 'core' scaffold itself, which might immunodominant over desired epitopes on the immunogen^{82,88,89}. These responses arise in part due to the use of non-self and engineered proteins to form particle cores, and incomplete particle self-assembly in some systems^{89,90}. Targeting of the particle scaffold can be minimized by using particles with nonimmunogenic

compositions, such as liposomes, through engineering particle structures where the core is sterically inaccessible, or through glycan or polymer masking of the nanoparticle core. Another strategy is to design a particle composed entirely of antigen, eliminating additional material that could elicit an off-target response altogether⁹¹.

1.5 Motivation and thesis overview

Despite the successes described above, there remain many open questions about optimal design principles for nanoparticle immunogens, and how these vaccines interact with the immune system. While numerous preclinical and a few clinical nanoparticle vaccines have been successfully developed, there are few guiding principles in the rational design of these vaccines other than that a high antigen density is desirable and that the particle core should be below 100 nm in diameter. However, if more guiding principles or generalizable design concepts were developed, this could expedite the creation of new nanoparticle vaccines for clinical use to better protect populations against diseases for which no vaccines currently exist. It was in the spirit of uncovering such principles that the work in this thesis was conceived and carried out.

When I initially joined the Irvine lab in 2016, our collaborators in the effort to create a functional HIV-1 vaccine had already created several promising antigens, including the engineered outer domain of gp120 (eOD) and a stabilized full gp120 trimer, BG505 MD39 (MD39)^{50,51,59,60}. Nanoparticle formulations of these same antigens, dubbed eOD-60mer and MD39-8mer, had also been successfully created and shown to provoke strong antigen-specific immune responses *in vivo*^{51,67-70}. What was surprising, however, was the degree to which these particles outperformed their soluble counterparts. I joined the lab with the goal of determining just what about these particles made them so effective and immunogenic and to see if lessons from their design could then be applied to other types of nanoparticle vaccines as well.

After reproducing the immune responses our collaborators had found, we sought to investigate if there was a difference in how the antigens were trafficked depending on their

formulation (Chapter 2). We found that the nanoparticle formulations rapidly accumulated within lymph node follicles while monomeric formulations failed to do so. We hypothesized that this accumulation could be responsible for the enhanced immunogenicity of the particles, since an increase in antigenic material within follicles during a germinal center reaction could mean that the reaction would be able to last for a longer time and produce a greater population of antigen-specific B cell receptors. Through *in vitro* experiments and trafficking studies in knockout mouse models, we found that this trafficking was dependent on mannose-binding lectin (MBL) recognition of glycans on the particle surfaces, and that the trafficking did indeed correlate with numerous enhanced immune outputs⁹⁰.

Having identified this trafficking pathway, we then sought to further examine the parameters determining whether or not particles could be trafficked and if different types of particles could be trafficked in a similar way (Chapter 3). We determined that the trafficking results in significantly enhanced total antigen accumulation in lymph nodes, and that this trafficking necessitated a sufficiently high density of high-mannose glycans on the surface of the nanoparticles. Further, numerous different types of nanoparticles were found to traffic in either MBL- or complement-specific manners to lymph node follicles, demonstrating that this pathway is not specific to only HIV immunogen-bearing particles.

Other important factors regarding nanoparticle vaccine design were explored using DNA origami virus-like particles as a model system (Chapter 4). These particles can be varied with a high degree of specificity, allowing for panels to be created that vary in only a single or few key characteristics. Utilizing these particles allowed us to explore the importance of antigen density and placement on a three-dimensional structure with regards to how those structures are able to interact with antigen-specific B cells.

2. Investigation of the Efficacy of HIV Nanoparticle Immunogens

2.1 Introduction

The immune system has evolved to recognize and respond to nano- and micrometer-sized particles such as viruses and bacteria. Notably, nanoparticles can be engineered to have several characteristics that have been shown in numerous preclinical studies to be advantageous to the development of a robust humoral immune response, including selective trafficking to lymphoid tissues through afferent lymph, improved internalization and processing for antigen presentation by dendritic cells, and enhanced B cell activation via cross-linking of antigen-specific B cell receptors⁹². Despite these features, there are no antigen-displaying nanoparticles in the clinical today with the exception of simple homomultimer virus-like particles in the case of human papillomavirus and hepatitis B virus^{93,94}.

The theoretical advantages of nanoparticulate display of antigen for vaccination have motivated a number of new studies for several key disease settings^{50,86,95,96}. With respect to HIV, evidence from preclinical animal models indicates that nanoparticulate HIV immunogens can more effectively activate low-affinity germline precursor B cells than monomeric antigens^{50,60,83,97}, promote enhanced follicular helper T (T_{fh}) cell induction and germinal center (GC) responses^{79,83,98}, and enhance the induction of neutralizing antibody responses^{69,83,99}. However, the mechanisms by which such adaptive immunity is influenced by the physical form of immunogens remain poorly understood.

To define pathways regulating immune response to multivalent particulate antigens *in vivo*, we examined the fates of two distinct HIV envelope proteins as soluble monomers or as protein nanoparticles. We compared a germline-targeting engineered outer domain of gp120 (eOD-GT8, herein referred to as eOD) and a gp140 envelope trimer (MD39)^{50,51,67,68}. This trimer is an improved version of BG505 SOSIP gp140 with enhanced thermal stability and expression level and reduced exposure of the V3 loop^{59,60}. We selected these two antigens as representatives

of “reductionist” antigens designed to elicit an immune response against a particular neutralizing epitope and of whole-envelope protein immunogens bearing multiple neutralizing sites, respectively.

To generate the protein nanoparticles, eOD was formulated as a 32-nm-diameter nanoparticle (eOD-60mer) by fusion to a bacterial protein, lumazine synthase, which self-assembles into a 60-mer^{51,67,68}. By contrast, a 40-nm-diameter nanoparticle form of MD39 (MD39-8mer) was generated by fusing the MD39 gp140 chain to an archaeal ferritin; 24 subunits of ferritin self-assemble to form a nanoparticle displaying eight copies of gp140 trimer^{69,100} (Figure 4).

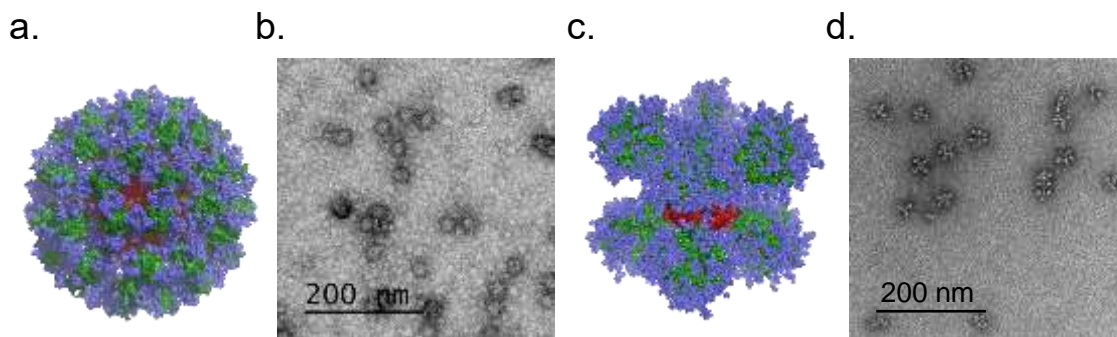


Figure 4. eOD-60mer and MD39-8mer. Cartoon schematics of **a** eOD-60mer and **c** MD39-8mer, showing core particle protein in red, antigenic protein in green, and surface glycosylation in blue. Cryogenic transmission electron microscopy images of **b** eOD-60mer and **d** MD39-8mer.

2.2 Nanoparticulate HIV immunogens elicit strong antigen-specific immune responses

Mice were immunized with monomeric or particulate forms of both antigens along with adjuvant via subcutaneous injection at the tail-base. Serum samples were collected weekly and antigen-specific IgG titers were assessed by ELISA. For both eOD and MD39, the nanoparticle formulations elicited much higher titers than the monomeric formulations. Indeed, monomers

failed to generate detectable antibody titers in half of the mice immunized (Figure 5a-b). Additionally, analysis of pooled antibodies from mice immunized with eOD or eOD-60mer revealed that antibodies from eOD-immunized mice had significantly higher off rates than those from eOD-60mer-immunized mice, indicating a difference in the binding capabilities of these antibodies (Figure 5c).

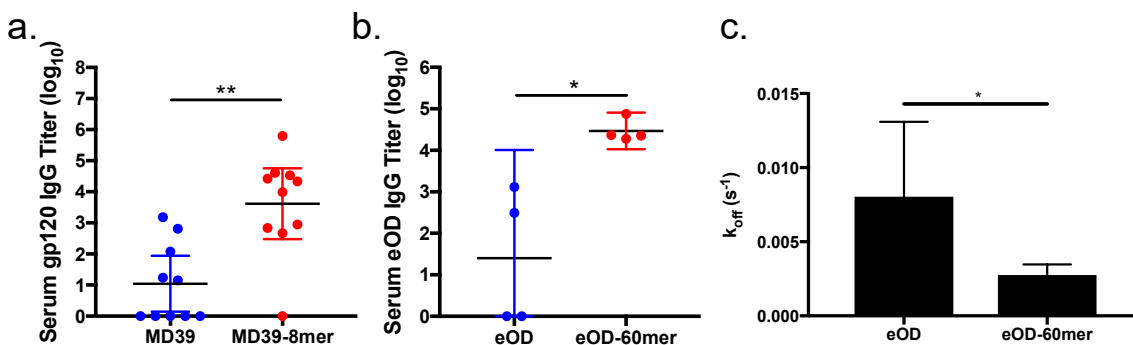


Figure 5. Antibody responses following MD39 and eOD immunization. **a** BALB/c mice were immunized with 1 μ g of MD39 or an MD39 equivalent amount of MD39-8mer together with saponin adjuvant and received a booster immunization at 6 weeks; individual gp120-specific IgG titers were analyzed 3 weeks post-booster immunization by ELISA. Data shows the means with 95% confidence intervals (CI) from one of three independent experiments. **b** BALB/c mice were immunized with 2 μ g of eOD monomer (blue) or an eOD equivalent amount of eOD-60mer (red) together with saponin adjuvant; individual eOD-specific IgG titers were analyzed one month postimmunization by ELISA. Data shows the means with 95% CI from one of five independent experiments. **c** Dissociation rates (k_{off}) of day 21 purified polyclonal IgG bound to immobilized eOD analyzed via biolayer interferometry for mice immunized with eOD or eOD-60mer. Shown are means and SD from one of three independent experiments. * $p < 0.05$; ** $p < 0.01$, by Mann-Whitney test.

GC and T_{fh} responses were also analyzed in these mice seven days post immunization. Both nanoparticle formulations showed much larger GC responses than their monomeric equivalents, suggesting that more widespread and/or robust germinal center reactions were ongoing in these mice. However, there was no significant difference in T_{fh} responses between particles and monomers (Figure 6a-d).

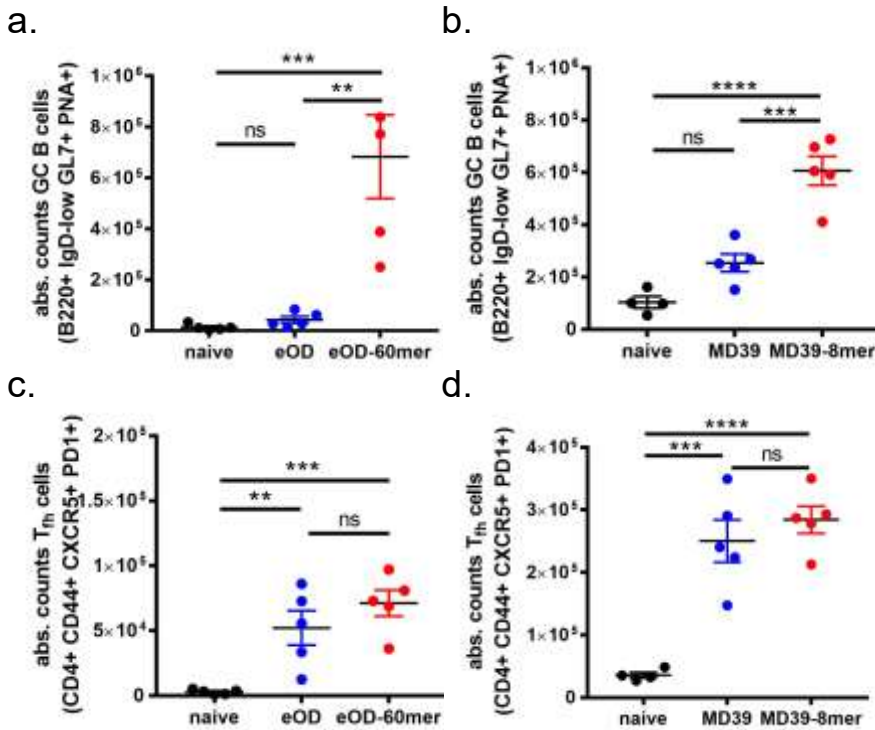


Figure 6. GC and T_{fh} responses to eOD and MD39 immunizations.

Mice were immunized with eOD or MD39 formulations as described in Figure 4; shown are absolute counts of **a,b** germinal center B cells and **c,d** follicular helper T cells as determined by flow cytometry on day 7. Shown are the means with SD from one of three independent experiments.

2.3 Nanoparticulate HIV immunogens selectively accumulate within draining lymph node follicles

Because nanoparticles are known to traffic different than smaller monomers due to their larger size, we hypothesized that differences in antigen fate within the lymph node could explain some of the differences that we had observed between nanoparticles and soluble antigen. We first evaluated this hypothesis by conjugating an infrared dye to the antigens, immunizing mice with these dye-labeled proteins, excising draining lymph nodes at various time points, and assessing these lymph nodes for total fluorescence at the dye's wavelength. Both particles were found to be present in lymph nodes in much greater amounts than monomers at multiple time points, suggesting that the antigen formulation has a major impact on ultimate antigen fate within the nanoparticle (Figure 7).

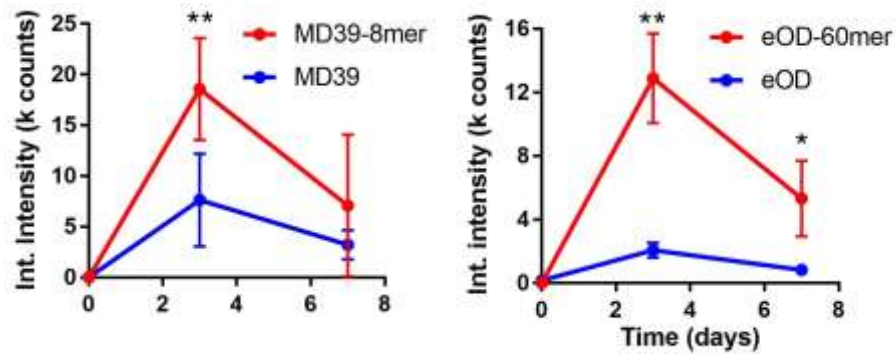


Figure 7. Bulk trafficking of MD39 and eOD formulations to draining lymph nodes. BALB/c mice were immunized with IR dye-labeled MD39, MD39-8mer, eOD, or eOD-60mer, and total fluorescence integrated (int.) intensity in draining lymph nodes was recorded over time. Shown are the means and SD from one of two independent experiments. k counts, 1000 counts. Each time point also contained lymph nodes from mice immunized with unlabeled antigen (data not shown).

We then conducted additional trafficking studies of dye-labeled antigen, this time processing lymph nodes to optically clear them in order to perform confocal microscopy throughout a substantial portion of each node. From this method, we determined that eOD and MD39 are present in the lymph node only in small amounts and are diffusely present throughout the medulla. MD39-8mer and eOD-60mer, however, rapidly accumulate within lymph node follicles, showing some localization at days one and three and being nearly completely localized within the follicles at later time points (Figure 8a-d). Higher magnification imaging revealed that eOD-60mer appears to colocalize directly with CD35, a marker expressed on follicular dendritic cells (FDCs), suggesting that the nanoparticles observed are being bound by FDCs for displaying to maturing B cells in a germinal center reaction (Figure 8e). This was further supported by additional staining for active GCs, which revealed eOD-60mer to localize to the light zone of germinal centers (Figure 8f).

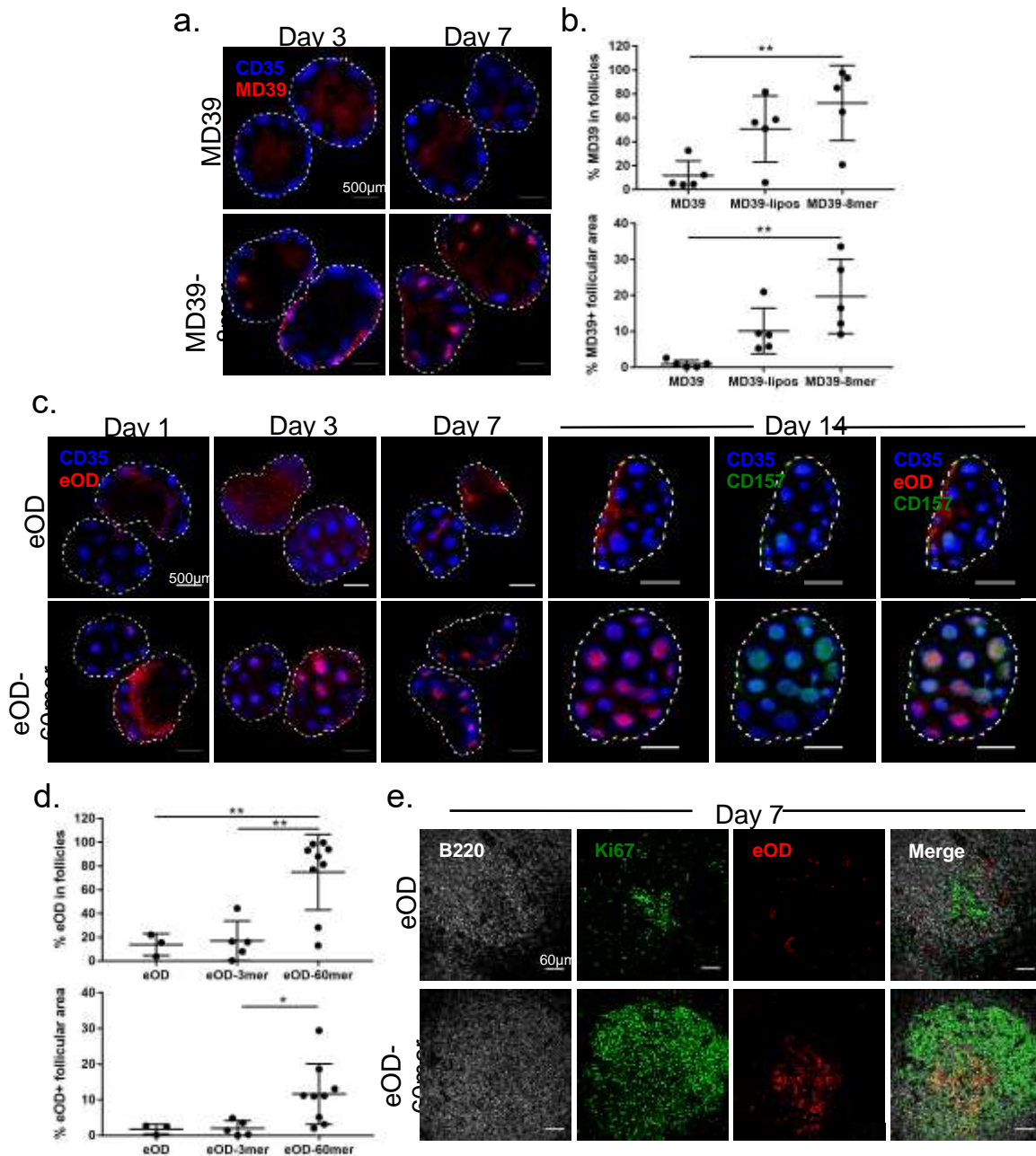


Figure 8. Nanoparticle eOD and MD39 immunogens are targeted to lymph node follicles. **a,b** BALB/c mice were immunized with 5 μ g fluorescent MD39 or MD39-8mer and adjuvant. Follicular dendritic cells were labeled *in situ* with anti-CD35 antibody, excised draining lymph nodes were cleared, **a** imaged by confocal microscopy, and **b** colocalization of antigen within follicles was quantified by the percentage of MD39 signal within follicles and by the percentage of follicular area that contained MD39. Shown are the means and SD from one of three independent experiments. **c-e** BALB/c mice were immunized with 2 μ g eOD and adjuvant. Follicular dendritic cells and/or germinal centers were labeled *in situ* with anti-CD35 and anti-CD157, respectively, and excised draining lymph nodes were cleared and **c** imaged by confocal microscopy. **e** Colocalization of antigen with follicles was quantified as in panel b. **e** Draining lymph nodes were cut into 100 μ m thick slices and stained with anti-B220 and anti-Ki67, and individual follicles were imaged by confocal microscopy. * $p < 0.05$; ** $p < 0.01$, by one-way ANOVA followed by Tukey's multiple comparison's test.

Importantly, an eOD trimer demonstrated localization comparable to that of eOD monomer, suggesting that a high valency is required trafficking to follicles to occur (Figure 9a). Further, bare lumazine synthase particles, with no displayed antigen on their surface, also failed to accumulate within lymph node follicles (Figure 9b). Follicular accumulation did occur when eOD-60mer was used to immunize a mouse in the absence of an adjuvant, indicating that this trafficking process is not dependent on factors beyond the physical form of the antigen (Figure 9c). These data collectively indicate that the trafficking phenomenon is dependent on a highly multivalent display of antigen.

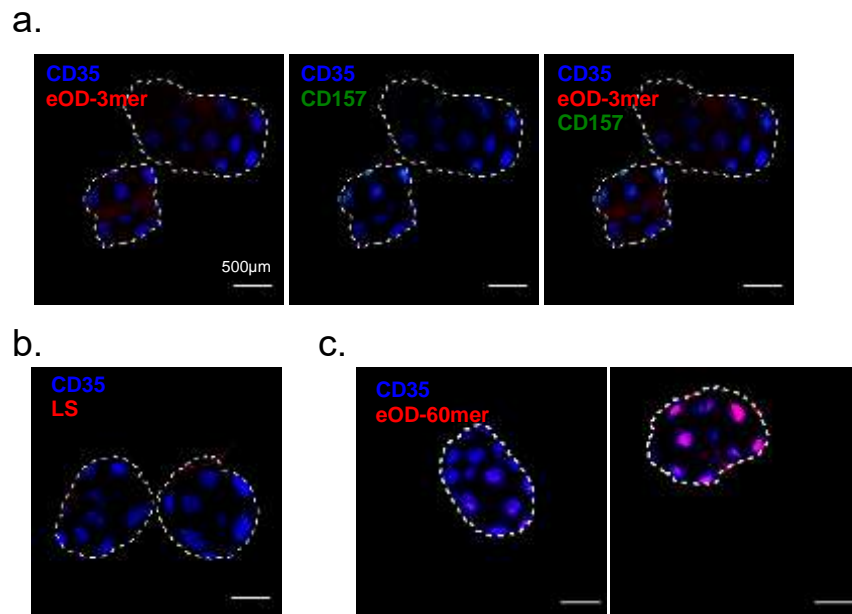


Figure 9. Trafficking is dependent on multivalent antigen display. **a** BALB/c mice were immunized with 2 µg eOD-3mer and adjuvant. Follicular dendritic cells and germinal centers were labeled *in situ* with anti-CD35 and anti-CD157, respectively. Draining lymph nodes were recovered after seven days, cleared, and imaged by confocal microscopy. **b** BALB/c mice were immunized with 2 µg bare lumazine synthase and adjuvant. Follicular dendritic cells were labeled *in situ* with anti-CD35. Draining lymph nodes were excised after seven days, cleared, and imaged by confocal microscopy. **c** BALB/c mice were immunized with 2 µg eOD displayed on eOD-60mer without (left) or with (right) saponin adjuvant. Draining lymph nodes were excised after one day, cleared, and imaged by confocal microscopy.

2.4 Follicular trafficking is complement dependent

Targeting to FDCs and GCs is not a generic property of nanoparticles in naïve animals, as many vaccine studies have shown particles of diverse sizes and material compositions to localize in a manner suggesting exclusion rather than enrichment in B cell follicles^{101–104}. By contrast, immune complexes, mesh-like networks of antigen and antibody bound together, have been reported to elicit a similar type of antigen delivery to FDCs^{105–107}. Immune complex trafficking to FDCs is mediated by the relay of complexes from subcapsular sinus macrophages to migrating B cells, which in turn transfer antigen to FDCs, in a complement- and complement receptor-dependent manner^{105–107} (Figure 10).

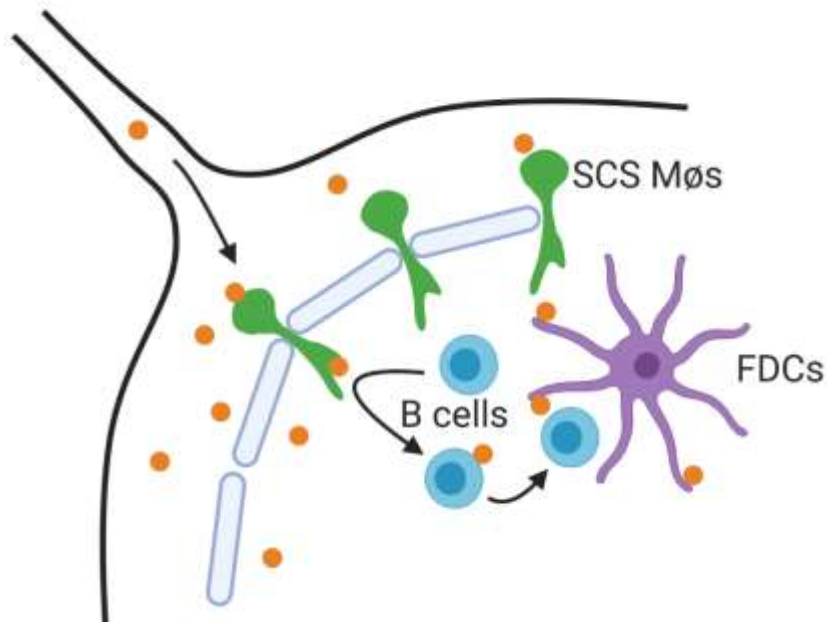


Figure 10. Immune complex shuttling to follicular dendritic cells. Immune complexes (orange) are opsonized by complement factors and drain through afferent lymph vessels to lymph nodes, encountering the subcapsular sinus. Subcapsular sinus macrophages (green, SCS Mφs) bind the immune complexes using complement receptors and transcytose them to the interior of the sinus. Migrating B cells (blue) then bind the complexes and transport them to follicular dendritic cells (purple, FDCs), where they are deposited on complement receptor 2 for display to B cells undergoing somatic hypermutation.

The complement system is one of the evolutionary oldest parts of the immune system and functions to recognize conserved non-self epitopes and danger signals to provide early protection while an adaptive immune response can be mounted. The complement cascade can be activated in three primary ways: 1) the classical pathway, in which complement proteins recognize conformational changes at the Fc region of antibodies when they have bound an antigen, as in the case of immune complexes; 2) the alternative pathway, in which complement spontaneously degrades on the surface of a pathogen and initiates a cascade due to a lack of suppression on the pathogen's surface, and; 3) the lectin pathway, in which soluble, glycan-binding lectins recognize sugar residues on an antigen or pathogen. Each of these pathways eventually lead to the cleavage of the C3 protein, which in turn leads to the release of pro-inflammatory cytokines, cellular recognition of complement-opsonized material, and clearance of foreign material^{108,109}.

To determine whether complement is also involved in the recognition of these nanoparticles and to test whether particle trafficking is mediated by interactions with complement receptors, we immunized mice lacking the C3 component of the complement system (C3 knockout [KO] mice) and mice lacking key complement receptors present on FDCs and other immune cell populations (Cr1/2 KO mice) with eOD-60mer or MD39-8mer. Both nanoparticles again strongly localized with FDCs in wild-type mice, but in both knockout strains only low levels of diffuse antigen were detected (Figure 11a,b). In mice unable to produce the secreted form of IgM (μ IgM KO mice), however, trafficking of eOD-60mer was present, suggesting that the classical pathway of complement activation is not the primary mediator of this trafficking phenomenon (Figure 11c). Further evidence against the classical pathway being a key instigator of trafficking was found by investigating the binding of natural IgM, preexisting antibodies that are generated at low levels without prior antigen exposure¹¹⁰, to eOD-60mer. Naïve wild-type mouse serum was not found to have any IgM recognition to eOD-60mer, demonstrating that murine natural antibodies do not have affinity against this nanoparticle (Figure 11d).

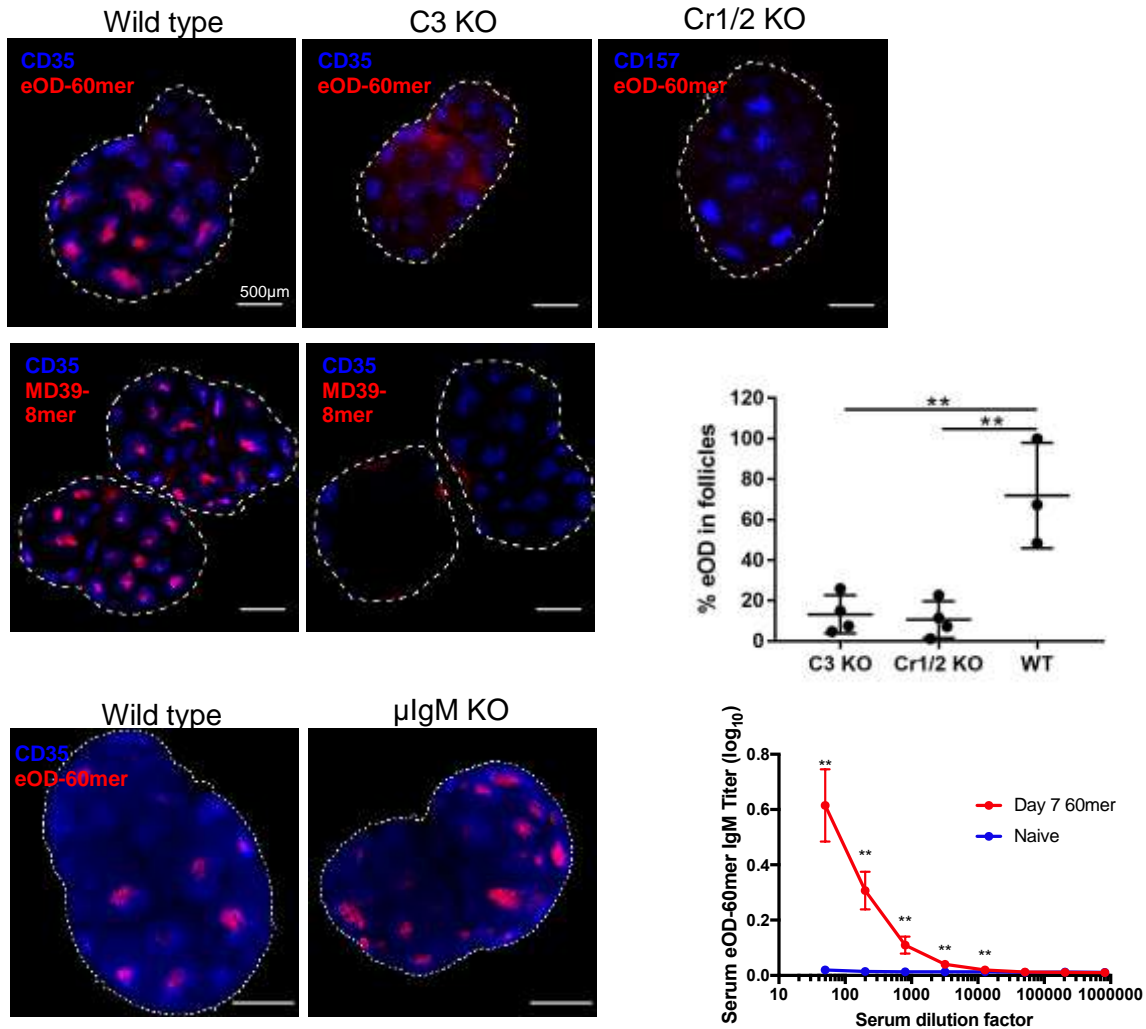


Figure 11. Nanoparticle trafficking is dependent on non-classical complement activation. **a** Wild-type C57BL/6, C3 KO, or Cr1/2 KO mice were immunized with 2 μ g equivalent fluorescent eOD-60mer or 5 μ g equivalent MD39-8mer and adjuvant. Draining lymph nodes were excised after seven days, cleared, and imaged by confocal microscopy. **b** eOD localization in follicles in wild-type vs KO mice was quantified by the percentage of eOD signal within follicles. Shown are means and SD from one of two independent experiments. ****** $p < 0.01$ by one-way ANOVA followed by Tukey's multiple comparisons test. **c** Wild-type C57BL/6 and μ IgM KO mice were immunized with 2 μ g equivalent fluorescent eOD-60mer and adjuvant. Draining lymph nodes were excised after seven days, cleared, and imaged by confocal microscopy. **d** Wild-type mice were immunized with 2 μ g equivalent eOD-60mer and adjuvant and serum was collected seven days later from these mice as well as naïve mice. eOD-specific IgM titers were analyzed by ELISA. ****** $p < 0.01$ by unpaired Mann-Whitney test.

2.5 *In vitro* complement deposition on nanoparticles is dependent on binding of mannose-binding lectin

Having determined that complement is implicated in the trafficking of these nanoparticles, we next sought to determine how complement is recognizing them. By ELISA, we found that C3 from wild-type serum deposited readily on eOD-60mer but did not bind to either eOD monomer or eOD trimer, suggesting that multivalency is critical for this complement recognition step (Figure 12a). However, while this assay indicated complement was binding to eOD-60mer, it did not directly support either the alternative or lectin pathways as being the primary mediator of complement deposition. To investigate this, we obtained serum from mice lacking both murine forms of mannose-binding lectin (MBL, [MBL KO mice]) and compared C3 deposition to eOD-60mer and MD39-8mer between MBL KO and wild-type sera. In both cases, exposure to MBL KO serum resulted in significantly less C3 deposition on the nanoparticles (Figure 12b). These results clearly implicated the lectin pathway as being the primary mode of complement recognition and potentially trafficking.

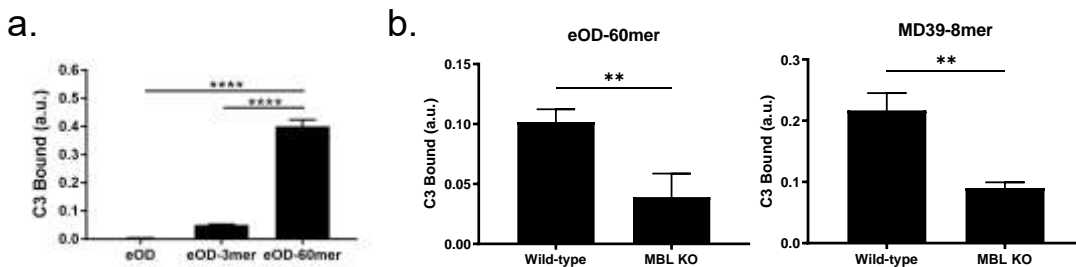


Figure 12. Complement binds nanoparticles in an MBL-dependent fashion. **a** Wild-type mouse serum was added to ELISA plates coated with eOD monomer, eOD-3mer, or eOD-60mer, followed by detection of deposited C3 by ELISA. **b** Wild-type or MBL KO mouse serum was added to ELISA plates coated with eOD-60mer or MD39-8mer, followed by detection of deposited C3 by ELISA. ** $p < 0.01$; **** $p < 0.0001$, by one-way ANOVA followed by Tukey's multiple comparisons test or Mann-Whitney test.

2.6 Deglycosylation of eOD-60mer leads to decreased MBL recognition

The lectin pathway is mediated by soluble lectins and is primarily instigated by MBL^{111,112}. MBL itself is a large macromolecular complex composed of multimers of trimeric lectin stalks, which achieve high-avidity binding to pathogens through multivalent engagement with large patches of dense sugars^{111,113,114}. Upon binding, MBL complexes with several MBL-associated serine proteases (MASPs), which become activated and can activate the complement cascade by either directly cleaving C3 or by cleaving C4 and C2 to form a C3 convertase. By either mechanism, C3b will be deposited on the surface recognized by MBL and C3a will be released¹¹⁵. Structural studies have shown that the three carbohydrate binding domains (CBDs) at the end of each stalk in the MBL multimer are arranged in a triangular configuration, separated by 4.5 nm¹¹⁶. The distance between each stalk of the MBL multimer, however, is poorly defined but expected to be of a similar order or larger¹¹⁷. Individual CBDs recognize mannose, fucose, glucose, and n-acetylglucosamine with a very weak affinity of K_D (dissociation constant) $\sim 10^{-3}$ M¹¹⁸, but stable binding to larger patches of glycans is thought to be achieved by the avidity effect of engaging multiple trimeric stalks of MBL multimers.

These considerations suggest that MBL will be unable to bind multiple stalks to an eOD monomer (diameter 7.5 nm) and may be capable of engaging only a few stalks on MD39 trimers (diameter 15 nm) simply due to an insufficient glycosylated surface area. The nanoparticle formulations, however, present much larger surfaces for MBL to potentially interact with glycans and could provide sufficient multivalency for a stable, long-lived interactions between nanoparticle and MBL (Figure 13).

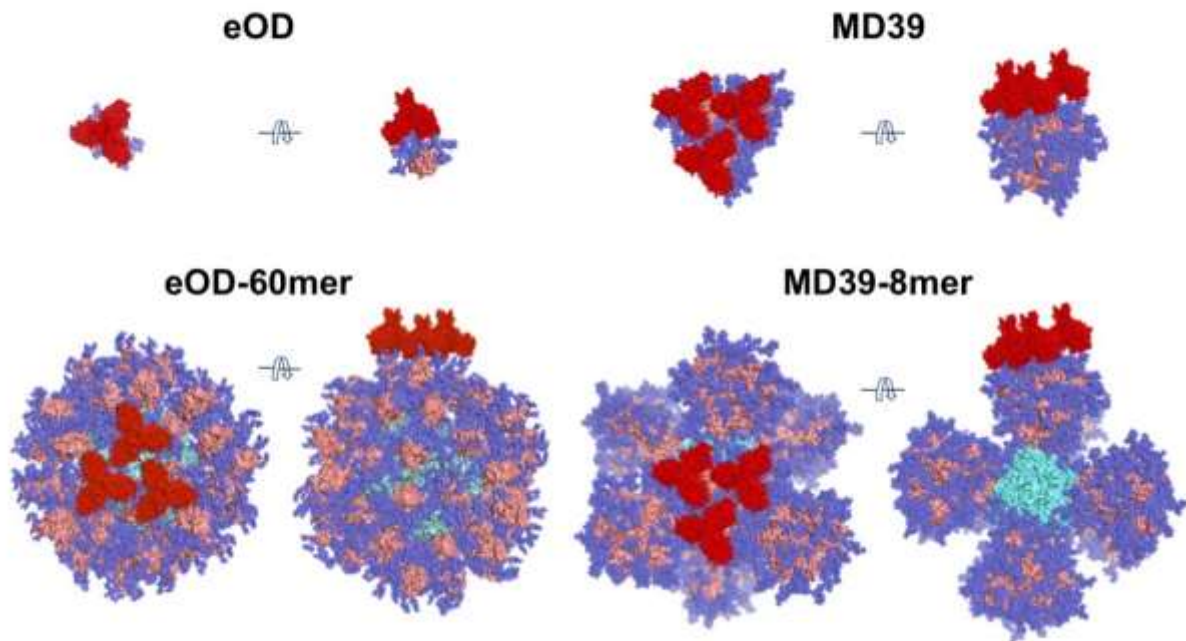


Figure 13. Structural models of trimeric stalks of MBL carbohydrate binding domains interacting with the glycans of eOD or MD39 antigens. The crystal structure of the trimeric carbohydrate binding domain (CBD) from one stalk of mannose binding lectin (PDB: 1HUP) was oriented either alone or as a hypothetical arrangement of three stalks onto structural models of eOD, eOD-60mer, MD39, or MD39-8mer, to illustrate at scale potential interactions between one trimeric stalk or three trimeric stalks of MBL and the immunogens. The modeling suggested that the small size of eOD monomer prevents it from interacting with more than one stalk, whereas MD39 trimer could potentially interact with several stalks and both eOD-60mer and MD39-8mer could potentially interact with an even larger number of trimeric stalks (only three are shown).

In agreement with these arguments, in an ELISA-type assay murine and human MBLs bound to immobilized eOD-60mer readily but exhibited only weak recognition of eOD monomer or eOD trimer (Figure 14a). Biolayer interferometry measurements of immobilized murine MBL binding to eOD, MD39, and their nanoparticle formulations further supported the hypothesized need for a high degree of multivalency for MBL binding. In both cases, binding to soluble antigen was low to undetectable, while robust binding was observed to eOD-60mer and MD39-8mer (Figure 14b). Notably, MBL binding to eOD-60mer did not obscure recognition of the primary antigenic epitope of eOD, suggesting that innate recognition of glycans would not inhibit on-target

antibody responses (Figure 14c). Notably, however, the binding of several broadly neutralizing antibodies was reduced when MD39-8mer was exposed to serum and coated in MBL and complement (Figure 14d). This has also been observed by other groups and suggests that in some cases excess glycosylation may be disadvantageous for the induction of desirable antibody responses¹¹⁹.

To provide further confidence that the binding was mediated by glycans present on the surface of the antigens, eOD-60mer and MD39-8mer were each treated with peptide:N-glycosidase F (PNGase F), a non-specific endoglycosidase capable of removing all N-linked glycosylation from most proteins^{120,121}. PNGase F treatment of eOD-60mer was found to not alter eOD-60mer structure or presentation of antigen and resulted in an ablation of MBL binding, while MD39-8mer was found to not be fully deglycosylated by PNGase F activity, possibility due to the recently described process N-glycanation¹²² (Figure 14e). Further experiments utilizing deglycosylated HIV antigen-bearing nanoparticles were focused on eOD-60mer exclusively.

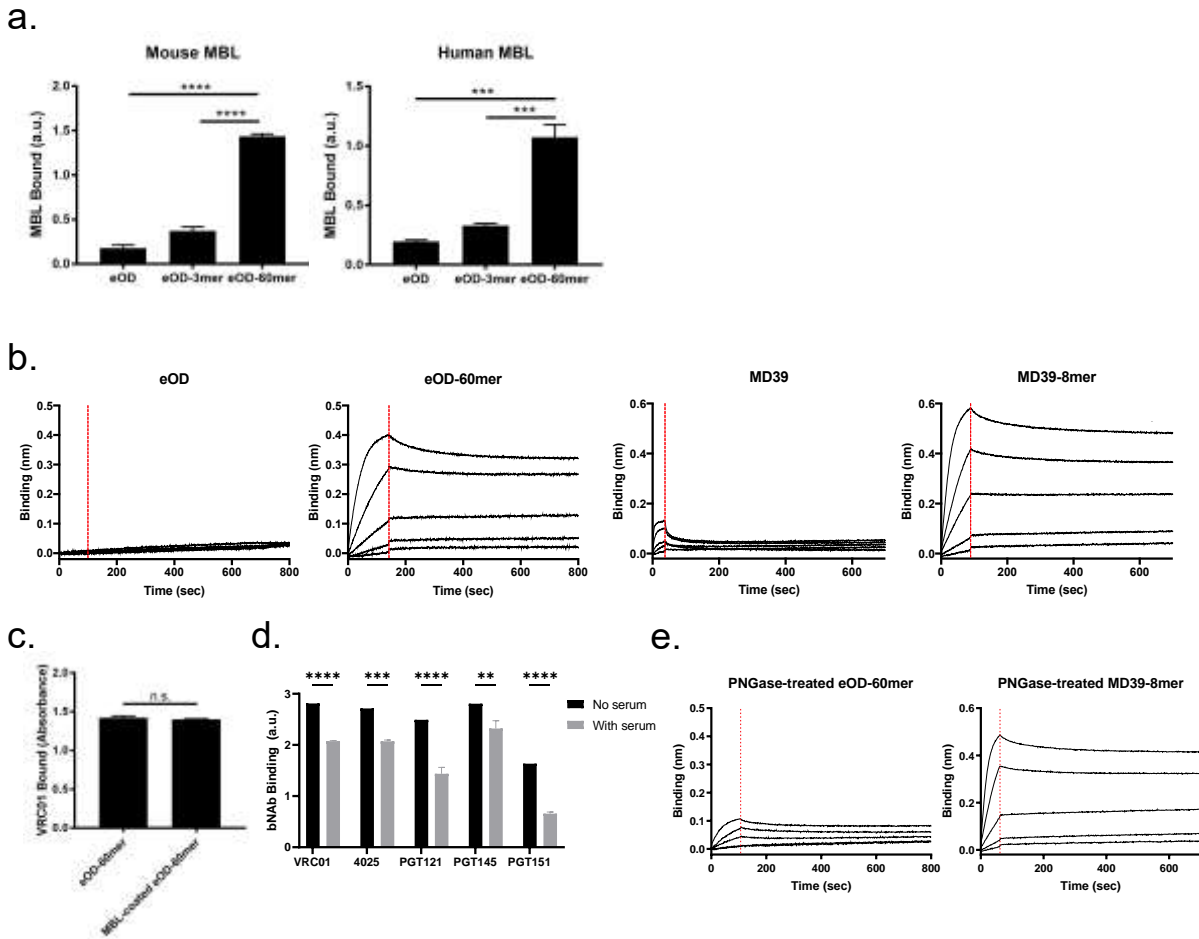


Figure 14. MBL binding to immunogens and its effect on antibody recognition of immunogens. **a** Mouse (200 ng/ml) or human (7.5 μ g/ml) MBL were added to ELISA plates coated with eOD monomer, eOD-3mer, or Eod-60mer, followed by detection of bound MBL by ELISA. **b** Biolayer interferometry binding and unbinding curves for eOD, eOD-60mer, MD39, and MD39-8mer binding to immobilized recombinant mouse MBL. **c** VRC01 was coated to eOD-60mer or eOD-60mer precoated with mouse MBL and bound VRC01 was detected by ELISA. **d** VRC01, 4025, PGT121, PGT145, or PGT151 were coated to MD39-8mer or MD39-8mer pre-exposed to 2% mouse serum for two hours and bound antibody was detected by ELISA. **e** Biolayer interferometry binding and unbinding curves for PNGase-F treated eOD-60mer and MD39-8mer binding to immobilized recombinant mouse MBL. Shown are means and SD, ns=not significant; $p^{**}<0.01$; $p^{***}<0.001$; $p^{****}<0.0001$, by one-way ANOVA followed by Tukey's multiple comparisons test or Mann-Whitney test.

2.7 Follicular trafficking of nanoparticles is dependent on MBL recognition

To evaluate whether MBL is involved in trafficking of nanoparticles to FDCs *in vivo*, we immunized MBL KO mice with eOD-60mer or MD39-8mer. Draining lymph nodes were found to contain only low levels of antigen with no significant accumulation in the FDC network (Figure 15a-b). To evaluate whether FDC localization was immunogen glycan dependent, we deglycosylated eOD-60mer with PNGase F and immunized mice as before. Deglycosylated eOD-60mer exhibited low accumulation in lymph nodes of wild-type mice with little to no FDC localization (Figure 15c). These data imply that dense arrays of glycans trigger MBL-mediated innate immune recognition of nanoparticles.

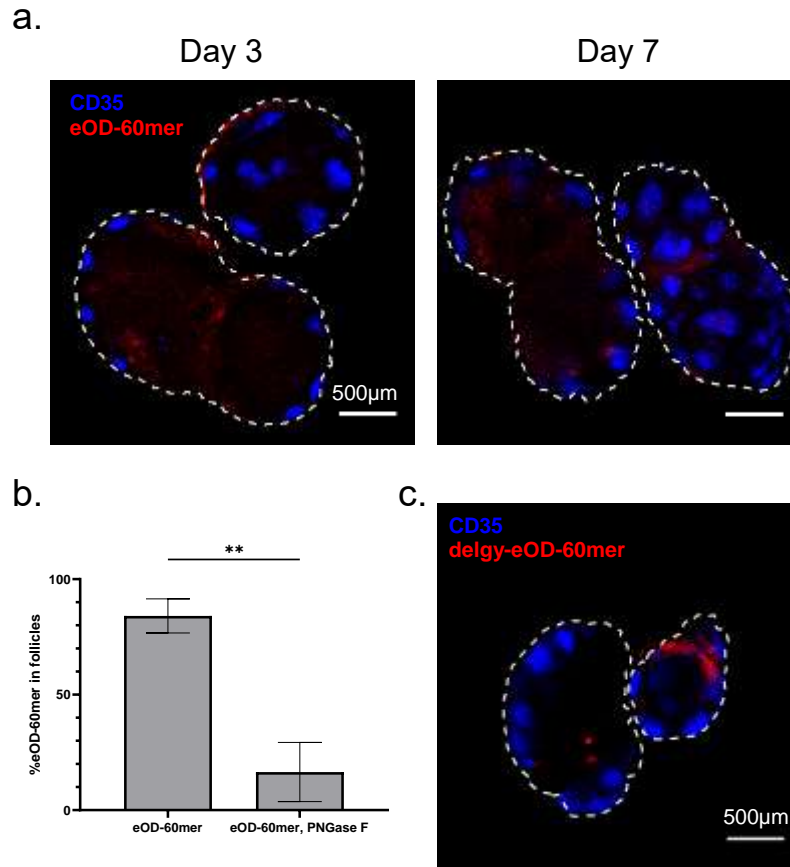


Figure 15. eOD-60mer fails to traffic to follicles in absence of MBL recognition. **a** MBL KO mice were immunized with 2 μ g eOD equivalent fluorescent eOD-60mer and adjuvant. Lymph nodes were excised, cleared, and imaged by confocal microscopy. eOD brightness was increased to allow for visualization. **b** Colocalization of eOD-60mer within follicles was quantified by the percentage of total eOD signal within follicles. Shown are the means and SD from one of three independent experiments. **c** Wild-type mice were immunized with 2 μ g eOD equivalent fluorescent PNGase F-treated eOD-60mer and adjuvant. Lymph nodes were excised, cleared, and imaged by confocal microscopy.

2.8 Immune responses to nanoparticle immunogens correlate with follicular trafficking

We then assessed the immunological effects of MBL recognition and FDC targeting. Wild-type mice immunized with nanoparticle eOD-60mer showed an IgG response two times that elicited by deglycosylated eOD-60mer (Figure 16a). Further, responses to eOD-60mer were stronger in wild-type mice than in MBL KO mice by several measures, with 53% greater T_{fh} cell responses, 43% greater GC B cell responses, and IgG titers about five times as high across multiple antibody isotypes (Figure 16b-e). IgG binding to plates coated with a low versus high density of antigen was also proportionally weaker for sera from MBL KO animals than for sera from wild-type mice, suggesting a lower mean avidity of IgG elicited in MBL KO animals (Figure 16f). Eight weeks postimmunization, wild-type mice also had approximately double the population of bone marrow-resident eOD-specific antibody-secreting cells as compared to MBL KO animals (Figure 16g). Furthermore, antibody titer differences were found to be present irrespective of the adjuvant used in the immunization, demonstrating that the immune benefit of follicular targeting is a property of the nanoparticle structure rather than other elements of the vaccine formulation (Figure 16h). Thus, despite preserving high multivalency for B cell receptor triggering, nanoparticles lacking MBL-mediated FDC targeting elicit weaker humoral immune responses.

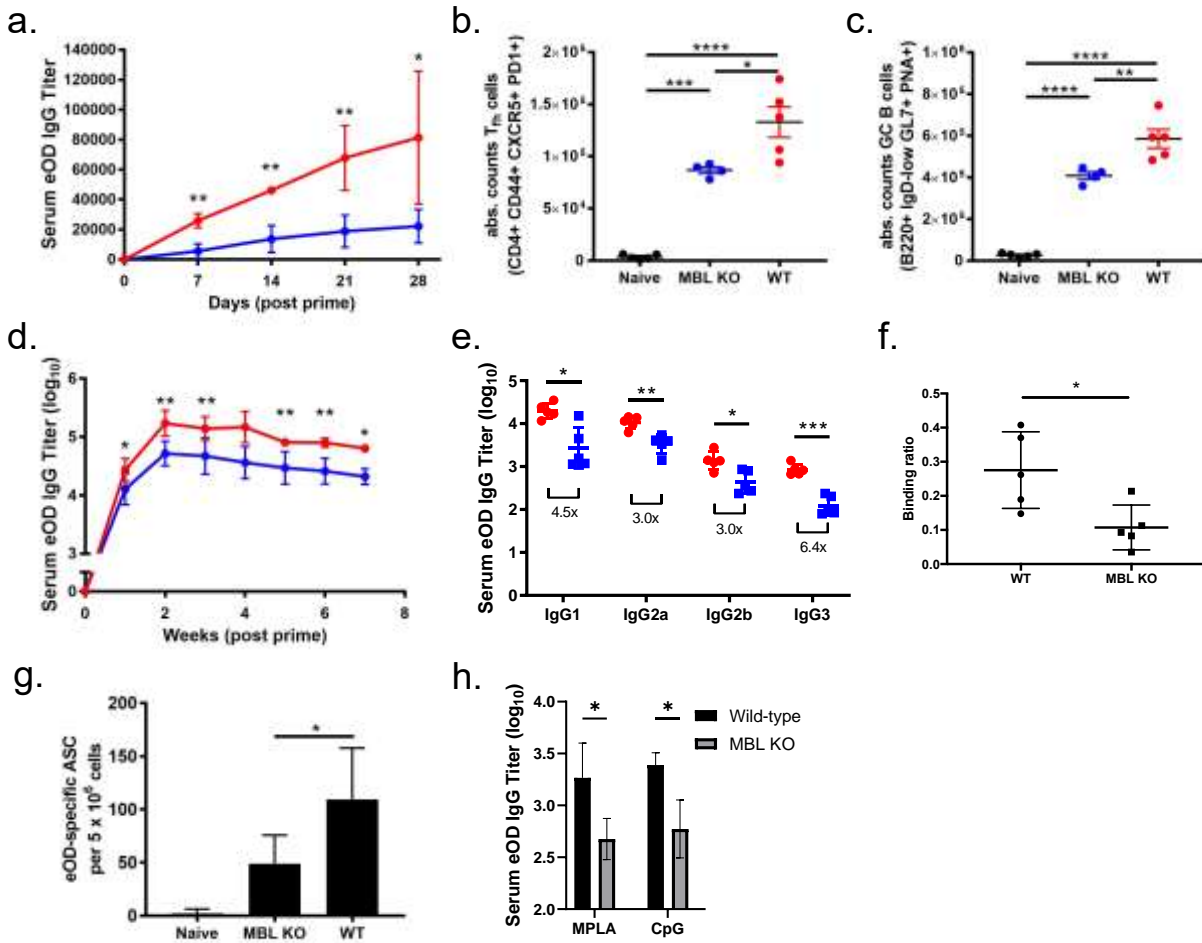


Figure 16. Follicular trafficking of eOD-60mer is associated with multiple increased immune outputs. **a** C57BL/6 mice were immunized with 2 μ g eOD equivalent unmodified (red) or PNGase F-treated (blue) eOD-60mer and adjuvant. Serum eOD-specific IgG titers from individual mice were analyzed over time by ELISA. Shown are mean with 95% CI from one of two independent experiments. **b-g** C57BL/6 (red) or MBL KO (blue) mice were immunized with 2 μ g eOD equivalent eOD-60mer and adjuvant. Absolute numbers of **b** germinal center T_{fh} cells and **c** germinal center B cells were analyzed at day 7. Shown are mean and SD. **d** eOD-specific IgG titers from individual mice were analyzed over time by ELISA. Shown are mean and 95% CI. **e** Isotype specific mid-point titers were analyzed four weeks post immunization. Shown are mean and SD. **f** Sera were assayed for eOD-specific IgG by ELISA using plates coated with a high or low density of eOD. Shown is the ratio of titers for binding on low-density plates to that measured on high-density plates as a measure of relative polyclonal antibody avidity. **g** Mean bone marrow eOD-specific ASCs were quantified by ELISPOT at eight weeks post immunization. Shown are mean and SD. **h** C57BL/6 and MBL KO mice were immunized with 2 μ g eOD equivalent eOD-60mer with either 10 μ g MPLA or 20 μ g CpG adjuvants. Serum eOD-specific IgG titers from individual mice were analyzed two weeks postimmunization by ELISA. * $p < 0.05$; ** $p < 0.01$; *** $p < 0.001$; **** $p < 0.0001$, by either one-way ANOVA followed by Tukey's multiple comparisons test or Mann-Whitney test.

2.9 Discussion

Collectively, these data point to a previous undescribed trafficking mechanism of glycosylated HIV antigen-bearing nanoparticles in which MBL-mediated innate immune recognition leads to rapid complement-dependent transport of particles to FDC networks and subsequent concentration in germinal centers *in vivo*. This targeting was associated with enhanced antibody responses, suggesting that tuning immunogen glycosylation may be a key design criterion for future nanoparticulate vaccines or immunomodulators and providing an explanation for how FDC localization of immunogens can occur in the absence of preexisting immunogen-specific antibodies.

This is especially important because historically, most antigen-bearing nanoparticles have been observed to be largely excluded from lymph node follicles. While many of these particles have still elicited humoral responses in preclinical models greater than that of the corresponding monomeric antigens, it is likely that the potential immunological benefits associated with multimerization will be decreased when less antigen has an opportunity to interact with the B cells that reside in follicles. This is directly suggested by the data presented in this chapter, as a loss of follicular targeting is associated in every case by a decrease in the measured immune outputs. Without follicle trafficking, by the MBL-mediated mechanism identified here or some other mechanism, it is possible that no nanoparticulate antigen will be able to reach its hypothetical maximal immunogenicity.

More generally, the studies described in this chapter point to the importance of determining an antigen's ultimate fate after immunization. While most potential antigens can elicit an immune response from various routes of immunization and various different formulations, this research highlights the importance of tracking the antigen to gain an understanding of how it is processed after the initial delivery of material. Clearly, not all antigens are the same, and it follows that there are numerous factors that could impact how effective they are at generating protective

immunity. The lymph node clearing method utilized herein is a powerful tool for determining that antigen is reaching the critical areas where it will have the greatest opportunity to interact with cells of the immune system responsible for eliciting such responses.

These findings open the door to a wide avenue of additional questions. In these studies, we focused on two nanoparticles with a number of similarities; both eOD-60mer and MD39-8mer have protein cores, bear HIV immunogens, are globular, are approximately the same size, and are natively glycosylated. These similarities make generalizing the results of this chapter to antigen-bearing nanoparticles as a whole somewhat difficult. In Chapter 3, we will explore many of these questions in greater detail.

2.10 Materials and Methods

Immunogen synthesis

Polyhistidine-tagged MD39 (MD39-6xHis) and cysteine-terminal MD39-6xHis were prepared as described previously^{51,60,68}. Briefly, trimer genes were synthesized and cloned into pHLsec by Genscript and then co-transfected with human furin on a pcDNA3.1 plasmid at a 2:1 trimer to furin DNA ratio using 293fectin into FreeStyle 293-F cells (ThermoFisher). Trimer supernatant was harvested five days post transfection by centrifugation and purified by affinity chromatography using HisTrap HP columns (GE Healthcare) followed by size-exclusion chromatography (SEC) using a S200 Increase column (GE Healthcare) in PBS at flow rate of 0.5 ml/min. The molecular weight of the trimer was confirmed by SEC multi-angle light-scattering (SECMALS) using DAWN HELEOS II and Optilab T-rEX instruments (Wyatt Technology). MD39-8mer, a nanoparticulate fusion of MD39 and ferritin from the hyperthermophilic archaeal anaerobe *Pyrococcus furiosus*, was produced and purified in a similar manner as MD39-6xHis with these modifications: 1) the affinity chromatography step was done by overnight 4°C incubation on Galanthus Nivalis Lectin agarose beads (Vector Laboratories #AL-1243), elution with Lectin Elution Buffer (1M Methyl α -D-mannopyranoside) followed by dialysis into PBS; and 2) the affinity

chromatography (SEC) step was done using a Superose 6 or a Superose 6 Increase column (GE Healthcare) in PBS at flow rate of 0.5 ml/min. Particle formation was assessed by SEC-MALS and by staining MD39-8mer with 2% uranyl formate, gridding and imaging by negative stain electron microscopy on a Philips CM100 TEM with a Soft Imaging Systems MegaView III CCD and SIA model 12C CCD cameras. eOD-GT8 monomer, trimer and 60mer were prepared as previously described^{50,51}. Briefly, eOD monomer and trimer were produced and purified in a similar manner as MD39-6xHis except that a Superdex 75 column (GE) was used for size-exclusion chromatography. eOD-GT8 60mer was purified using the same protocol as MD39-8mer. "Bare" ferritin was expressed in E.coli with a 6xHis tag at the N-terminus of each ferritin subunit and purified by Ni⁺⁺ chromatography followed by SEC.

Synthesis of saponin adjuvant

The adjuvant used for all the described studies was an ISCOM-like nanoparticle comprised of self-assembled cholesterol, phospholipid, and Quillaja saponin prepared as previously described¹²³; all synthesis was performed under sterile conditions with sterile reagents. Briefly, 10 mg each of cholesterol (Avanti Polar Lipids 700000) and DPPC (Avanti Polar Lipids 850355) were dissolved separately in 20 % MEGA-10 (Sigma D6277) detergent at a final concentration of 20 mg/ml and 50 mg Quil-A saponin (InvivoGen vac-quil) was dissolved in MQ H₂O at a final concentration of 100 mg/ml. Next, DPPC solution was added to cholesterol followed by addition of Quil-A saponin in rapid succession and the volume was brought up with PBS for a final concentration of 1 mg/ml cholesterol and 2 % MEGA-10. The solution was allowed to equilibrate at 25 °C overnight, followed by 5 days of dialysis against PBS using a 10k MWCO membrane. The adjuvant solution was then filter sterilized using a 0.2 µm Supor syringe filter, concentrated using 50k MWCO centricon filters, and further purified by FPLC using a Sephacryl S-500 HR size exclusion column. Each adjuvant batch was finally characterized by negative stain TEM and DLS to confirm uniform morphology and size and validated for low endotoxin by Limulus

Amebocyte Lystae assay (Lonza QCL-1000). Final adjuvant concentration was determined by cholesterol quantification (Sigma MAK043).

Immunizations

Balb/c, C57BL/6, C3 KO, Cr1/Cr2 KO, μ IgM KO, and MBL KO mice were purchased from Jackson Laboratory (Bar Harbor, ME). Mice were housed under specific pathogen-free conditions. All procedures used in this study were approved by the Committee on Animal Care at the Massachusetts Institute of Technology following local, state, and federal regulations.

Female mice 6-10 weeks of age were immunized with immunogen and adjuvant via subcutaneous tail-base injection with 50 μ l on either side of the tail. Mice immunized with eOD, eOD-3mer, eOD-60mer, or HA-8mer received a total of 2 μ g eOD or HA, while mice immunized with MD39, MD39-8mer, or MD39-liposomes received either 1 or 5 μ g MD39. For immunizations with particle immunogens, total molar equivalence of immunogen was kept constant, approximately 0.1 nmol for eOD and 5 pmol or 25 pmol for MD39, equivalent to 3.7 μ g eOD-60mer and 1.3 or 6.4 μ g MD39-8mer, respectively. All immunizations included 5 μ g saponin adjuvant unless otherwise noted. For a few experiments, monophosphoryl lipid A (MPLA PHAD, Avanti Polar Lipids 699800) or CpG 1826 DNA (5'-tccatgacgttctgacgtt-3', InvivoGen tlr1-1826) were used as alternate adjuvants. For trafficking studies, mice were similarly immunized with AlexaFluor 647-tagged immunogens (ThermoFisher A20186). Immunogens were characterized by UV-vis spectroscopy and contained \sim 1 dye/monomeric eOD and \sim 45 dyes/eOD-60mer (i.e. \sim 0.75 dyes/monomer) while each MD39 trimer contained \sim 5.7-6.1 dyes/trimer and \sim 44-45 dyes/MD39-8mer (i.e. \sim 5.6 dyes/trimer). Trimers on liposomes were similarly pre-labeled prior to liposome conjugation as soluble trimers. For trafficking in knockout animals, equal mixtures of female and male mice were used due to availability. For trafficking of bare nanoparticles, mice were immunized with 2 μ g of Alexa-Fluor 647-tagged nanoparticle. Mice were then injected subcutaneously in the tail base with 4 μ g BV421-labeled anti-CD35 (BD Biosciences 740029) 16-

18 hours prior to LN excision to label follicles *in situ*. Injection of 20 µg PE-labeled anti-CD157 (Biolegend 140204) one day prior to lymph node removal was used as an alternative to label B cell follicles for mice lacking complement receptor 1, while injection of anti-CD157 three days prior to lymph node removal was used to label active germinal centers¹²⁴.

LI-COR immunogen tracking

Balb/c mice were immunized (as described above) with 5 µg IR dye 800CW NHS-Ester (LI-COR Biosciences) labeled MD39 or MD39-8mer and 5 µg saponin adjuvant or with 2 µg IR dye 800CW NHS-Ester labeled eOD or eOD-60mer and 5 µg saponin adjuvant. At specified times, draining lymph nodes were excised and fluorescence was measured using a LI-COR Odyssey CLx Infrared Imaging System. Fluorescence was reported as the total integrated intensity for each set of lymph nodes.

Antibody titer analysis

Blood samples were collected from immunized mice via retro-orbital bleeds and serum was isolated. MaxiSorp plates (ThermoFisher 44-2404-21) were coated with either 2 µg/ml immunogen or 1 µg/ml rabbit anti-polyhistidine antibody (Genscript) followed by 2 µg/ml HIStagged immunogen. Analysis of IgG responses elicited by immunization with deglycosylated immunogens was carried out by coating ELISA plates with the matching deglycosylated antigen. Plates were blocked overnight in a solution containing 1x PBS, 5% skim milk, 10% goat serum, 1% BSA, 1% FBS, and 0.2% Tween-20. In the case of plates coated with anti-polyhistidine antibodies, polyhistidine-tagged immunogen was then added and allowed to incubate for two hours. Plates were washed four times in 1x PBS containing 0.2% Tween-20, and dilutions of serum in blocking buffer were added and incubated for two hours. Plates were washed as before and an HRP-conjugated anti-mouse IgG was added and incubated for one hour. For analyses of antigen-specific IgG isotype titers, HRP-conjugated anti-mouse IgG1, IgG2a, IgG2b, and IgG3 antibodies were used at this step. Plates were then washed and TMB was added. The reaction

was stopped with sulfuric acid once the wells containing the lowest dilutions of TMB began to develop visually and the absorbance of each well was determined. All titers reported are inverse dilutions where $A_{450\text{nm}} - A_{540\text{nm}}$ (reference wavelength) equals 0.2.

Bio-layer interferometry

All bio-layer interferometry measurements were conducted using a ForteBio Octet RED96 instrument in the MIT Biophysical Instrumentation Facility. eOD monomer was biotinylated via NHS-amine chemistry (ThermoFisher 21925). Streptavidin-coated biosensors were incubated in PBS containing 1% BSA, then moved to wells containing the same solution with 3 ug/ml biotinylated monomeric eOD for five minutes. Nonspecifically bound eOD was removed with a three minute baseline step, and eOD-coated biosensors were moved to wells containing dilutions of polyclonal IgG from immunized mice for five to ten minutes. The biosensors were then moved back to the baseline solution and dissociation of IgG from the biosensors was detected.

For dissociation constant analysis of MBL binding to eOD and MD39 formulations, the same protocol was performed in PBS containing 1% BSA and 0.1 M CaCl. Streptavidin-coated biosensors were loaded in solution containing 1 ug/ml biotinylated mouse MBL for several minutes. Excess MBL was washed off and MBL-coated biosensors were moved to wells containing dilutions of antigen formulations until probes began to become saturated. The biosensors were then moved back to the baseline solution and antigen was allowed to dissociate.

Germinal center and T_{fh} analysis

Mice were sacrificed by CO₂ inhalation and both inguinal lymph nodes were harvested at specified days. Lymph nodes were processed into single-cell suspensions using enzymatic digestion with 0.8 mg/ml Collagenase/Dispase and 0.1 mg/ml DNase (Roche Diagnostics) in complete RPMI (with 10% FBS and antibiotics) at 37°C, followed by passage through a 70- μm cell strainer (BD Biosciences). Next, cells were washed with PBS and stained with Live/Dead Aqua (Life Technologies) for 15 minutes at 25°C. Samples were then treated with anti-CD16/32

Fc block (BioLegend 14-0161-85), followed by staining with anti-CD3e-PerCP-Cy5.5 (BD Biosciences 5204845), anti-B220-PE-Cy7 (BioLegend 103222), anti-IgD-APC (eBioscience 17-5993-82), anti-GL7-FITC (BioLegend 144604), and PNA-biotin (VectorLabs ZB1228) + streptavidin-APC-Cy7 (BD Biosciences 554063) in PBS/1% BSA and finally fixed and stored at 4°C until analysis. Alternatively, to simultaneously stain for germinal center B cells and T follicular helper cells, cells were similarly stained with Live/Dead Violet (Life Technologies) followed by Fc block and staining with anti-B220-BV510 (BD Biosciences 563103), anti-IgD-APC (eBioscience 17-5993-82), anti-GL7-FITC (BioLegend 144604), anti-CD38-APC-Cy7 (BioLegend 102727), anti-CD4-PerCP-Cy5.5 (eBioscience 45-0042-82), anti-CD44-AlexaFluor700 (BioLegend 103026), anti-PD1-PE-Cy7 (eBioscience 25-9985-82), and anti-CXCR5-biotin (BD Biosciences 551960) + streptavidin-PE (BioLegend 405204) in PBS/1% BSA and finally fixed and stored at 4°C until analysis. Flow cytometry was carried out on a BD LSR Fortessa.

For studies in which antigen-specific T_{fh} was assessed, analysis was performed as previously described^{125,126}. Briefly, 1×10^6 cells were stimulated with 5 µg/ml of intact antigen (monomeric eOD or trimeric MD39) in addition to 5 µg/ml of an overlapping peptide pool for 18 hours at 37°C. Unstimulated cells were run as a control. Cells were then washed and similarly stained with Live/Dead Aqua and treated with anti-CD16/32 Fc block (BioLegend 14-0161-85), followed by staining with anti-B220-BV510 (BD Biosciences 563103), anti-CD4-PerCP-Cy5.5 (eBioscience 45-0042-82), anti-CD44-AlexaFluor700 (BioLegend 103026), anti-PD1-PE-Cy7 (eBioscience 25-9985-82), anti-OX40-APC (BioLegend 119413), anti-CD25-FITC (BioLegend 101907), anti-PDL1-BV421 (BioLegend 124315), and purified rat anti-CXCR5 (BD Biosciences 551961) + goat anti-rat IgG-biotin (Jackson ImmunoResearch 112-065-167) + streptavidin-PE (BioLegend 405204) in PBS/2% normal mouse serum/2% FBS/1% BSA and finally fixed and stored at 4°C until analysis. Flow cytometry was carried out on a BD LSR Fortessa.

Lymph node processing for whole-tissue imaging

For whole-tissue imaging, lymph nodes were excised from mice and fixed overnight at 4°C in 4% paraformaldehyde. Lymph nodes were then processed as previously described (33) with some modifications to improve protein retention in lymph nodes. Briefly, they were washed twice in PBS and excess fat and connective tissue was removed. Nodes were then gradually moved into solutions containing successively high concentrations of methanol over the course of several hours until they were incubated for half an hour in pure methanol. Nodes were then briefly bleached in hydrogen peroxide for one minute before being returned to methanol for half an hour. They were then gradually moved into solutions containing increasing concentrations of tertiary-butanol before eventually being incubated in pure tertiary-butanol for one hour. All solutions used after bleaching contained an additional 0.4% α -tocopherol (vitamin E). Nodes were then removed from solution and allowed to dry completely before being placed in dichloromethane. After the lymph nodes dropped to the bottom of tubes following swirling (indicating removal of remaining tertiary-butanol), they were stored in dibenzylether with 0.4% α -tocopherol, which was used as an optical clearing solution.

Lymph node processing for immunofluorescence microscopy

Lymph nodes were excised from mice and fixed in 4% paraformaldehyde at 37°C for two hours. Lymph nodes were then washed in PBS (three times, five minutes each) before being embedded in 3% agarose. Nodes were cut into 100 μ m thick slices. The slices were blocked in 10% goat serum for one hour and then stained with anti-B220 and anti-Ki67 overnight at 37°C. The slices were then washed in PBS (three times, one hour each) and mounted on slides.

Confocal microscopy and image processing

Whole lymph nodes were imaged using an Olympus FV1200 Laser Scanning Confocal Microscope. Lasers were set to minimize pixel saturation in the brightest samples. All laser and channel settings were then kept constant across time points for individual studies to allow for direct comparison between different samples. Each lymph node was imaged over 300 μ m.

Lymph node slices were imaged using a Leica SP8 Laser Scanning Confocal Microscope. Laser settings were determined similarly to as described for whole lymph node imaging.

Microscopy images were analyzed using ImageJ. To reduce background signal bleeding into other channels, each channel other than the 405 nm channel was passed through an HSB filter against background fluorescence. Z-stacks were then condensed into average intensity projections ranging over the full 300 μm displaying the average intensity of each color for each pixel.

To quantify immunogen signal and follicle colocalization, first the maximum intensity z-projection on all channels was binarized and used to define a selection comprising the whole lymph node area. Next, for each z-height slice in the imaged sample, a high-pass filter was applied such that the brightest pixels in the background autofluorescence channel were binarized. These bright pixels in the autofluorescence channel were zeroed in the signal channels in an attempt to mitigate the intensity effects of bleedthrough from autofluorescence into the signal channels (ie: a pixel $[x,y,z]$ of bright autofluorescence was zeroed for corresponding $[x,y,z]$ for all pixels across all signal channels). Although this method may reduce true signal (resulting in an underestimated intensity quantitation), it successfully removes a substantial contribution from autofluorescence to the true signal intensity by wholly removing the pixels most prone to bleedthrough from autofluorescence. A sum intensity z-projection on the combined CD35+PNA/CD157 channels was binarized and used to define a selection comprising the follicular area. Finally, a sum intensity z-projection on the immunogen signal channel (following autofluorescence reduction) was binarized using a high pass filter such that bright pixels were applied an intensity value of 1, while dim pixels were applied an intensity value of 0. This binary mask was used to multiply a sum intensity z-projection such that all dim pixels were zeroed while all bright pixels retained their unaltered intensity information. This was done to prevent skewing of immunogen signal from the high number of near-zero background pixels that existed despite autofluorescence signal

reduction. The intensity of only these bright pixels was measured within both the whole lymph node and follicular areas for use in ratiometric antigen signal intensity calculations (i.e. % immunogen within follicles). In addition, only bright pixels were quantified to identify overall immunogen signal distribution within follicles (i.e. % immunogen+ follicular area).

C3 and MBL assays

eOD formulations were coated directly on to MaxiSorp plates in 50 μ l PBS at 3 μ g/ml eOD. Plates were then blocked overnight in PBS containing 1% BSA and 0.1 M CaCl₂. For MBL assays, dilutions of MBL were added and plates were incubated for two hours. For C3 assays, dilutions of normal or MBL KO mouse serum were added and plates were incubated at 37 C for two hours, with a maximal concentration of 30% serum. Plates were then washed four times in PBS containing 0.1% Tween-20 and anti-MBL or anti-C3 antibodies were added, followed by another two-hour incubation. Plates were washed as before and HRP-conjugated secondary antibodies were added. Following an hour-long incubation and additional washes, TMB was added and plates were developed until the lowest dilution wells started to visually show signal. The reaction was then stopped with sulfuric acid and the absorbance at 450 nm was read via plate reader.

eOD-60mer deglycosylation

eOD-60mer was deglycosylated using PNGase F (New England BioLabs P0704S) under non-denaturing conditions following the manufacturer's guidelines. Deglycosylation was confirmed via SDS-PAGE gel using glycoprotein stain (ThermoFisher 24562). eOD-60mer was confirmed to maintain its structure using dynamic light scattering and cryo-transmission electron microscopy. The retention of immunogen conformation on the surface of eOD-60mer was confirmed via ELISA against VRC01 as compared to unmodified eOD-60mer.

Bone marrow ELISPOT

Total IgG and antigen-specific IgG ELISPOTs were carried out using a mouse IgG ELISpot^{BASIC} (ALP) protocol from Mabtech with some modifications. One day prior to cell seeding,

Millipore multiscreen PVDF well-plates were pre-treated for 1 minute with 35% ethanol, followed by overnight coating at 4°C with 10 µg/ml polyclonal anti-mouse IgG (Mabtech) in phosphate buffer. The next day, wells were washed with PBS/0.5% BSA and blocked with complete RPMI (with 10% FBS and antibiotics). Bone marrow from both hind legs (femur and tibia) of immunized balb/c mice was harvested and ACK lysed for 1 minute, followed by washing in PBS/1% BSA. 100,000 cells were plated in 250 µl complete RPMI for 4 hours at 37°C. All samples were plated in duplicate wells. Cells and media were then washed away and spots were detected using either 1 µg/ml biotinylated rat anti-mouse IgG monoclonal antibody (Mabtech) for total B cell responses or 2 µg/ml biotinylated eOD monomer (prepared by reacting eOD with NHS-PEG₂-biotin for 2 hours at 25°C at a eOD:NHS ratio of 1:20) for antigen-specific B cell responses for 2 hours, followed by secondary detection with streptavidin-ALP conjugate (Mabtech) for 1 hour at 25°C. Spots were finally developed using 5-bromo-4-chloro-3-indolyl phosphate/nitroblue tetrazolium chloride substrate solution (BCIP/NBT-plus; Mabtech) for 5 minutes. Plates were scanned using a CTL-ImmunoSpot Plate Reader and data were analyzed using CTL ImmunoSpot Software.

Statistical analysis

Statistical analyses were performed using GraphPad Prism software. All values and error bars are shown as mean ± standard deviation, with the exception of serum titer data that are shown as mean ± 95% confidence interval. Serum titers were analyzed using a Mann-Whitney test. All other data was analyzed using an unpaired *t* test for direct comparisons or an ordinary one-way ANOVA followed by a Tukey's post-test to compare multiple groups, unless otherwise noted.

3. Assessment of generalizability of MBL-mediated nanoparticle trafficking

3.1 Introduction

Numerous preclinical studies have found that nanoparticles of a variety of compositions drain efficiently via the lymphatic system, but upon reaching secondary lymphoid tissues remain primarily localized within the subcapsular sinus and the medulla, and are seemingly excluded from B cell follicles^{101–104,127}. We have previously demonstrated that natural glycosylation of HIV antigens, when displayed on a dense, multivalent nanoparticulate platform, are recognized upon immunization by MBL and selectively accumulate within draining lymph node follicles in an MBL- and complement-dependent manner⁹⁰. Here, we further explore this trafficking mechanism to elucidate its applicability to the development of future nanoparticle vaccines. We continued our investigations of HIV antigen nanoparticles and expanded to include other clinically relevant nanoparticles as well as glycosylated but non-antigen-bearing nanoparticles.

3.2 Generation and investigation of differentially glycosylated eOD-60mer particles

Protein glycosylation is a posttranslational modification that occurs primarily in the endoplasmic reticulum and Golgi apparatus in eukaryotic cells^{128–132}. eOD-60mer is no exception to this, and the glycosylation on the surface of the nanoparticle can be modulated during protein production via the inclusion of small molecule inhibitors in the culture media. One such inhibitor, kifunensine, is able when in media to prevent the modification of initial high-mannose glycosylation into more complex glycan forms, resulting in proteins that are fully glycosylated but exclusively with oligomannose^{133–136}. The previously described studies in this thesis utilizing eOD-60mer all utilized this high-mannose glycoform of eOD-60mer (HM 60mer). When eOD-60mer is expressed in the absence of kifunensine (complex 60mer), only about one quarter of the

glycosylation is predominantly oligomannose and the remainder was either complex or hybrid (Figure 17).

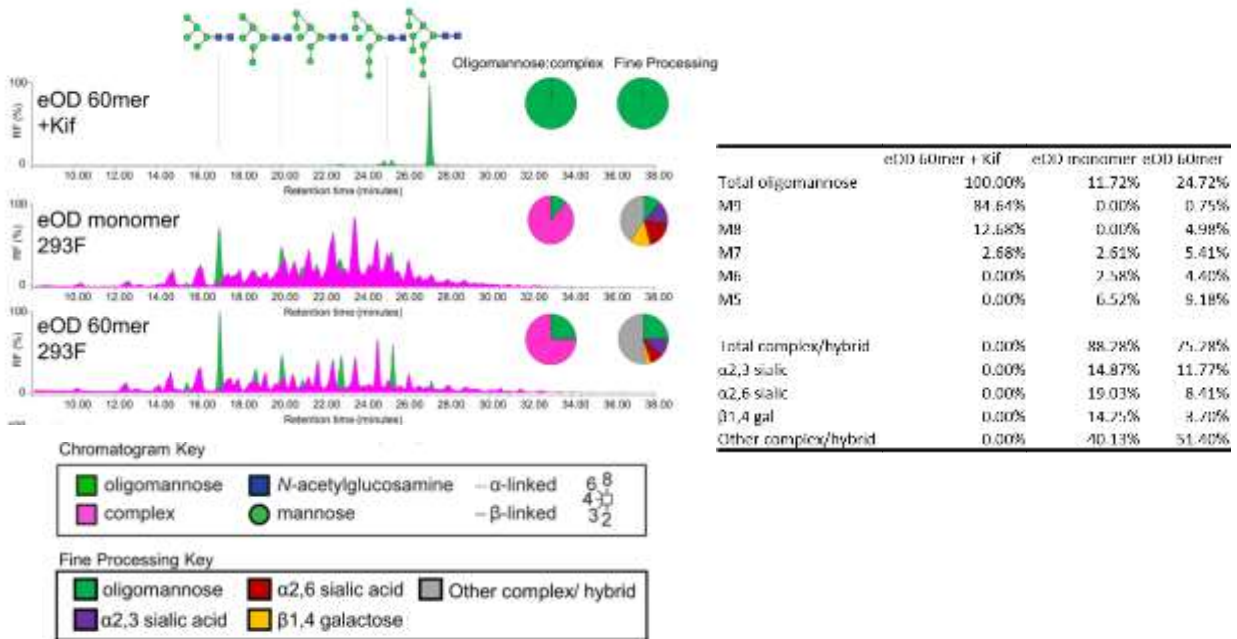


Figure 17. Global glycan analysis of eOD and eOD-60mer using ultra-high performance liquid chromatography (UPLC). UPLC chromatograms of N-glycans from eOD 60mer+kif, eOD monomer, and eOD-60mer. Peaks sensitive to endoglycosidase H (Endo H) digestion are colored green and represent oligomannose-type or hybrid-type glycans. Peaks resistant to Endo H are colored magenta and represent complex-type glycans. The first pie chart depicts the quantification of oligomannose-type glycans in each sample. The second pie chart displays the quantification of the fine processing of complex-type glycans. Complex-type glycans containing α2,3 sialic acid residues are colored purple, α2,6 sialic acid are colored red and those terminating with a β1,4 galactose residue are colored yellow. Other N-linked glycans corresponding to complex-type or hybrid-type glycans are colored grey. Peaks corresponding to the series of oligomannose-type glycans (Man₅₋₉GlcNAc₂) are annotated with symbolic representation of the most abundant isomer.

These two eOD-60mer glycoforms were further modified via endoglycosidase treatment. PNGase F was used to fully deglycosylate each particle, while endoglycosidase H (Endo H) was used to selectively cleave high-mannose residues while preserving hybrid and complex glycans^{137–139}. The six total glycoforms were then evaluated for murine MBL binding by biolayer interferometry. Both HM 60mer bearing only high-mannose glycans and complex 60mer bearing predominantly complex glycans bound to immobilized MBL in a concentration-dependent manner, but binding was greater for HM 60mer. Notably, treatment of the nanoparticles with Endo H ablated binding for both high-mannose- and complex glycan-bearing particles, indicating that MBL recognition of eOD-60mer is dependent on oligomannose on the nanoparticle (Figure 18a). As anticipated, treatment with PNGase F abrogated all binding of MBL to both 60mer particles.

To assess the biological impact of these distinct MBL binding patterns, we imaged the localization of each of the eOD-60mer glycoforms in draining lymph nodes following immunization. Strikingly, while both untreated HM 60mer and complex 60mer concentrated in follicles within three days of injection, Endo H- and PNGase F-treated particles exhibited greatly reduced follicular accumulation (Figure 18b,c). Thus, follicular trafficking of eOD-60mer is intrinsically linked to MBL recognition of not simply any glycans on the particle surface, but specifically recognition of oligomannose residues. In line with this, there was no difference in antigen-specific IgG titers from mice immunized with either HM 60mer or complex 60mer (Figure 18d). Together, these data suggest that while oligomannose is required for MBL recognition, a maximal density of oligomannose may not be required.

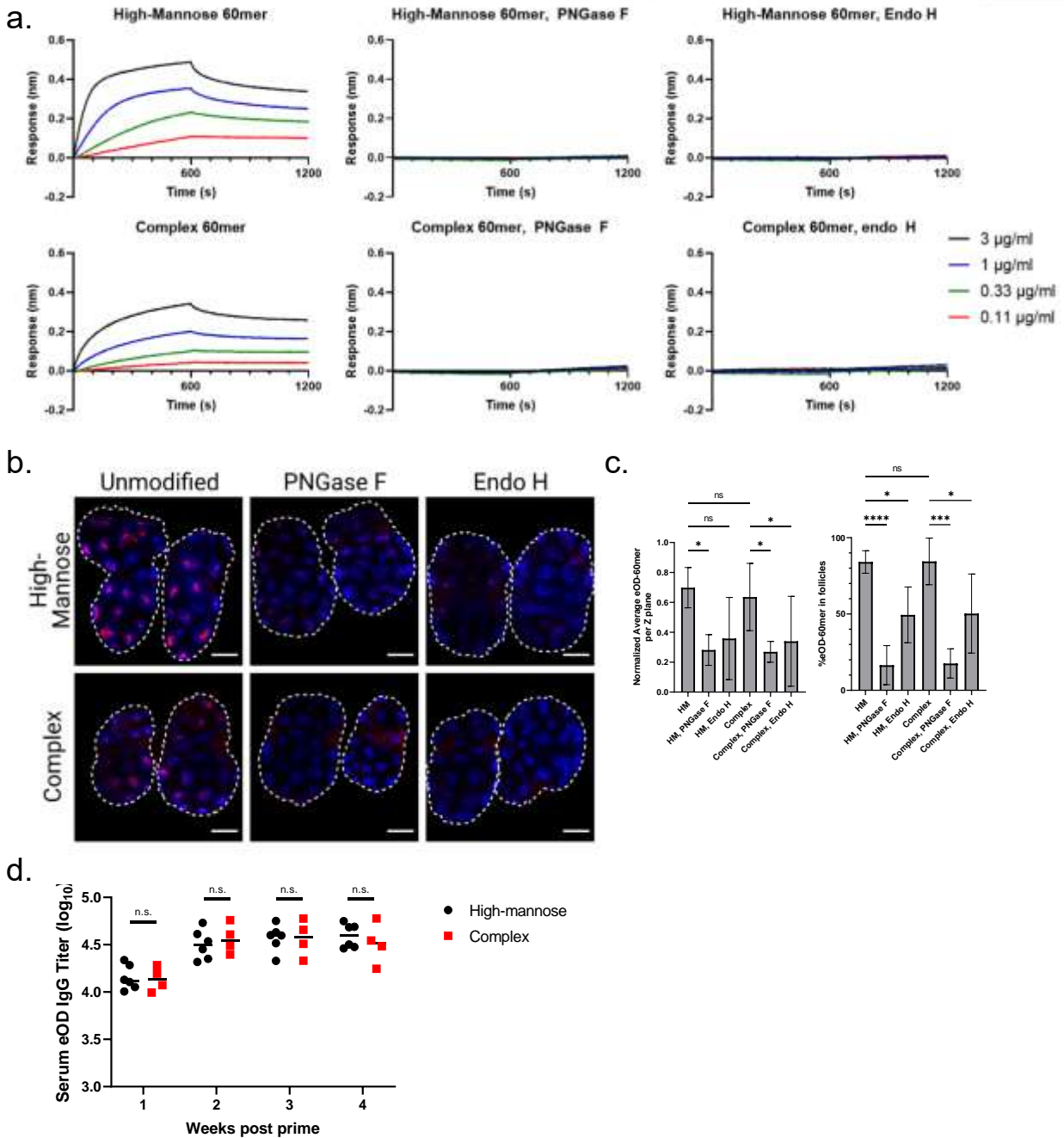


Figure 18. High-mannose glycans are required for MBL-driven eOD-60mer accumulation in lymph node follicles. **a** BLI analysis of eOD-GT8 60mer glycan variants binding to immobilized recombinant murine MBL2 as a function of eOD particle concentration. **b, c** C57Bl/6 mice ($n=5/\text{group}$) were immunized with $2\ \mu\text{g}$ eOD equivalent eOD-GT8 60mer glycan variants and saponin adjuvant. Shown are **b** average intensity Z projections of cleared draining lymph nodes harvested on day 7 (Blue, CD35; red, eOD-GT8 60mer; scale bars denote $500\ \mu\text{m}$), and **c** analyses of normalized total eOD-GT8 60mer signal per Z plane of cleared lymph nodes and percent eOD-60mer signal found within follicles. **d** C57BL/6 mice were immunized with with $2\ \mu\text{g}$ eOD equivalent high-mannose eOD-60mer or complex eOD-60mer and adjuvant. Serum anti-eOD IgG titers were analyzed over time by ELISA. Error bars indicate SEM; *, $p<0.05$; $p^{***}<0.001$; $p^{****}<0.0001$, ns=not significant by one-way ANOVA followed by Tukey post hoc test.

3.3 MD39-bearing liposomes traffic to lymph node follicles

Thus far we had evaluated the trafficking of a variety of self-assembling nanoparticle structures, but we had not investigated other common nanoparticle compositions. As a first step to see if trafficking can occur in significantly different particles, we synthesized liposomes with 100 nm diameters and conjugated MD39 trimer to the surface via the inclusion of a phospholipid with a maleimide head group into the bilayer⁷⁹. Despite the larger particle size and different structure, these particles trafficked to lymph node follicles in a manner similar to what had been observed for the previously evaluated protein nanoparticles (Figure 19). This indicates that the trafficking mechanism is not unique to self-assembled protein particles and opens the door for investigating the trafficking of a variety of different nanoparticles.

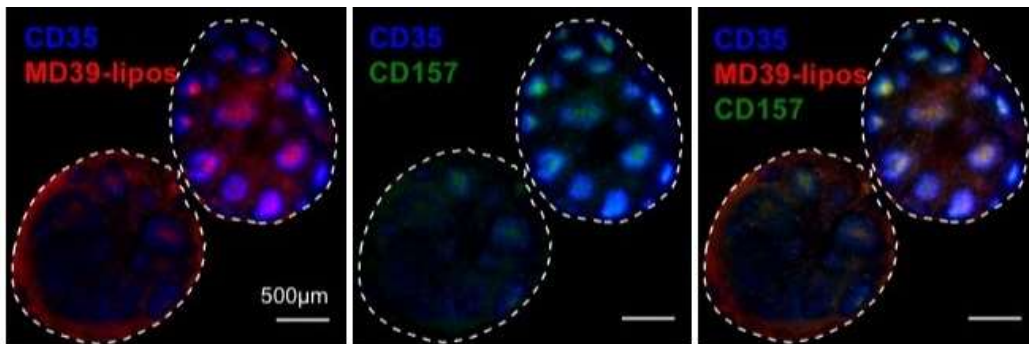


Figure 19. Trafficking of MD39-displaying liposomes to lymph node follicles. BALB/c mice were immunized with 5 µg fluorescent MD39 on 100 nm diameter liposomes and adjuvant. Follicular dendritic cells and germinal centers were labeled *in situ* with anti-CD35 or anti-CD157, respectively. Draining lymph nodes were recovered after seven days, cleared, and imaged by confocal microscopy.

3.4 Development and analysis of mannosylated, non-antigen-bearing nanoparticles

At this time, we had determined that multiple classes of nanoparticles were able to be trafficked by via the MBL pathway, but had only evaluated nanoparticles bearing HIV immunogens. To evaluate if these proteins were required for trafficking, we sought to investigate the trafficking of non-antigen-bearing particles coated in synthetic trimannose moieties. We first investigate dye-loaded polystyrene beads of 40 nm, 100 nm, and 200 nm diameters. These were conjugated with excess trimannose and purified by dialysis (Figure 20a). Each size nanoparticle was found to not bind to MBL *in vitro* prior to trimannose conjugation but exhibited a large degree of binding post modification (Figure 20b). These nanoparticles were then injected subcutaneously in mice and their lymph node localization was assessed by immunohistochemistry. Of all tested particles, only the mannosylated 40 nm particles showed follicular localization (Figure 20c). These data indicated that antigen is not required for MBL and complement recognition of nanoparticles, and that polystyrene beads were another class of particles that could be trafficked in the manner previously uncovered. Importantly, the apparent size constraints on trafficking observed in this study mirror results in the literature that lymphatic drainage of nanoparticles is most efficient when the diameter is below 100 nm^{140–145}.

In addition to the polystyrene beads, we also evaluated mannosylated ferritin nanoparticles. These used the same ferritin core as MD39-8mer but lacked any additional antigen displayed on the surface. These were glycosylated using a similar method to the polystyrene beads (Figure 21a). Two distinct glycoforms were produced, one bearing approximately 25 trimannose groups per particle and one bearing 96 per particle. Each of these, in addition to an unglycosylated control, were injected in mice and the lymphatic trafficking was analyzed. Both the unglycosylated and low glycan density particles did not exhibit detectable accumulation in follicles, while the high glycan density particles did localize (Figure 21b). These data indicate that there is

a minimal degree of glycosylation required for MBL recognition, in agreement with past literature on the highly avid nature of MBL binding events^{116,118,146}.

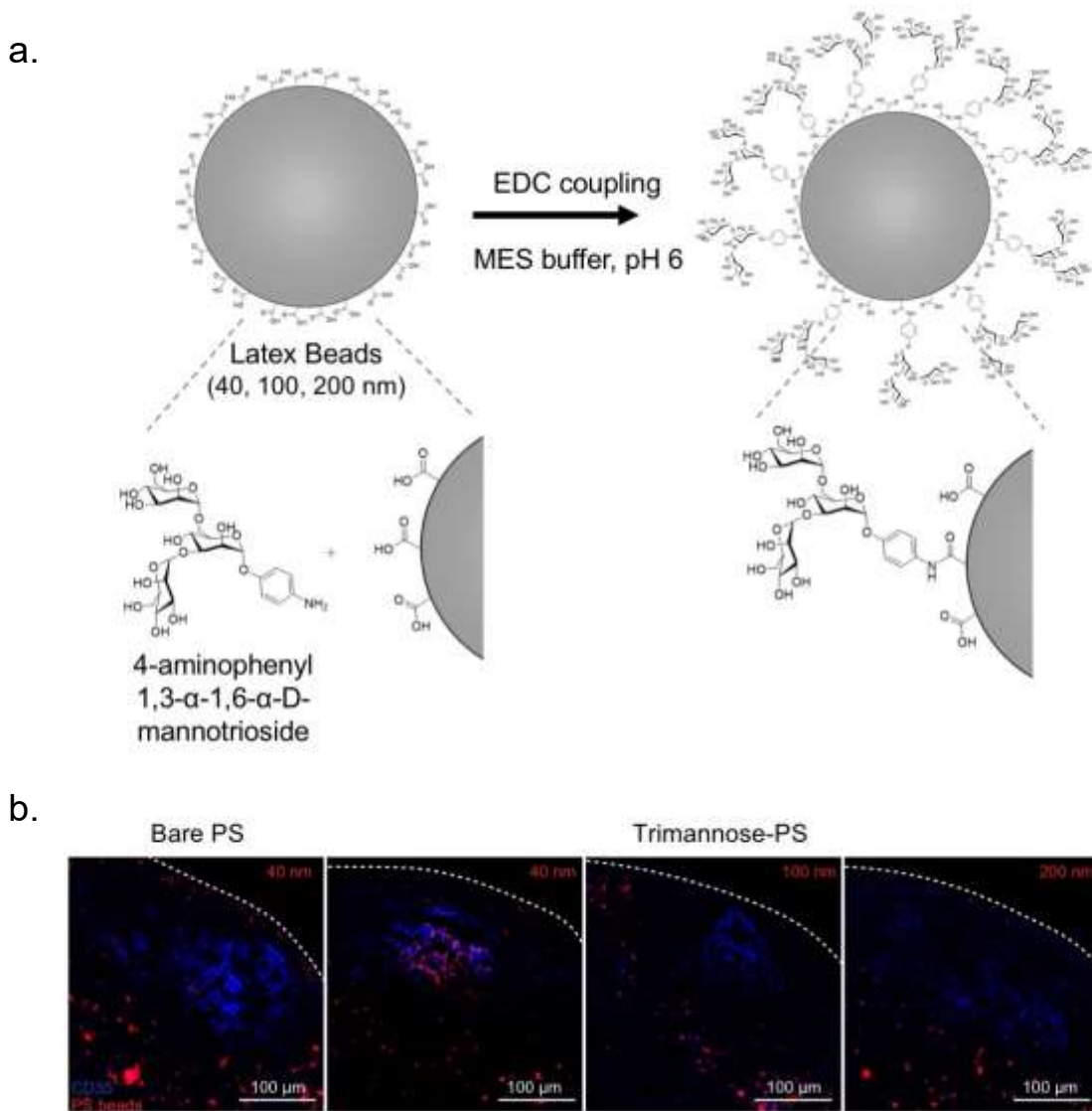


Figure 20. Trimannose functionalization of small polystyrene (PS) nanoparticles promotes follicular dendritic cell localization in lymph nodes. **a** Chemistry of trimannose coupling to polystyrene nanoparticles. **b** C57BL/6 mice were immunized with 10 μ g PS nanoparticles of 40 nm, 100 nm, or 200 nm diameters conjugated with trimannose or not with adjuvant. Lymph nodes were excised seven days later, fixed, sectioned, and imaged by confocal microscopy.

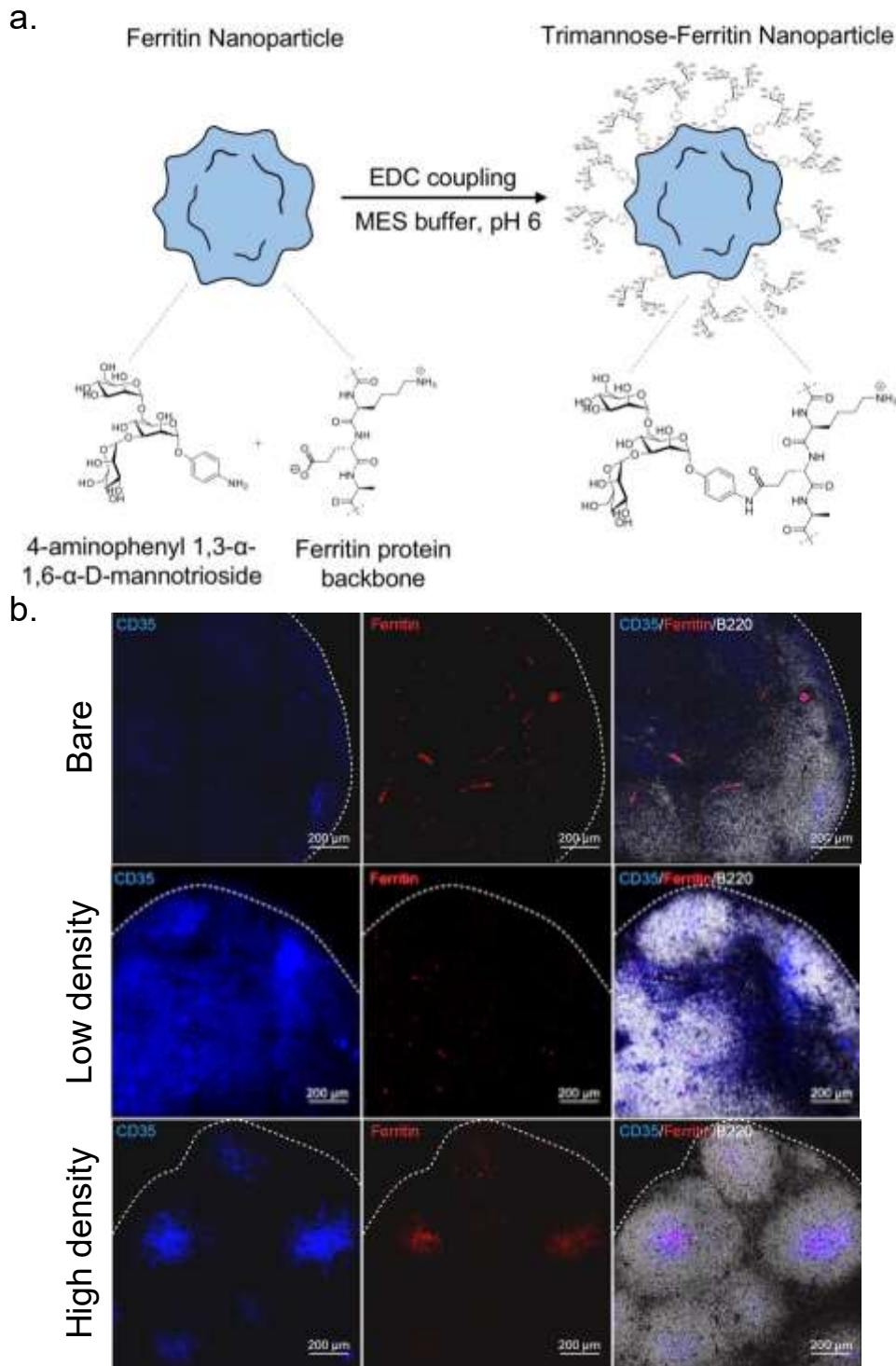


Figure 21. Trimannose functionalization of ferritin nanoparticles promotes follicular dendritic cell localization in lymph nodes. a Chemistry of trimannose coupling to ferritin nanoparticles. b C57BL/6 mice were immunized with 5 μ g of fluorescent bare ferritin nanoparticles lacking glycans, 5 μ g ferritin nanoparticles with a low density of trimannose moieties (~25 trimannose groups per particle), or 5 μ g ferritin nanoparticles with a high density of trimannose moieties (~96 trimannose groups per particles) and adjuvant. Lymph nodes were excised three days later, sectioned, and imaged by confocal microscopy.

3.5 *In vitro* MBL binding to serially mannosylated nanoparticles

In an attempt to assess the minimal required density of mannosylation for MBL recognition, polystyrene beads were coated as before with either synthetic mannose or galactose residues. As anticipated from evidence in the literature, MBL was unable to bind to galactose-coated particles but recognized mannose-coated particles readily as before^{118,147}. Utilizing MBL's lack of recognition for galactose, a panel was created consisting of nanoparticles reacted with different molar ratios of mannose to galactose, in effect altering the surface area of MBL-recognizable glycan. These particles were analyzed by bilayer interferometry, and it was found that while particles coated in only mannose were the strongest binders, particles bearing between 50% and 75% mannose had similar degrees of MBL binding. However, binding fell off rapidly when the mannose proportion of reacted glycans was reduced beyond 50%, with very little binding detected at 25% (Figure 22). While this is a reductionist system that is unlikely to closely model *in vivo* behavior, it does provide some helpful guidance for the general degree of glycosylation required for MBL recognition.

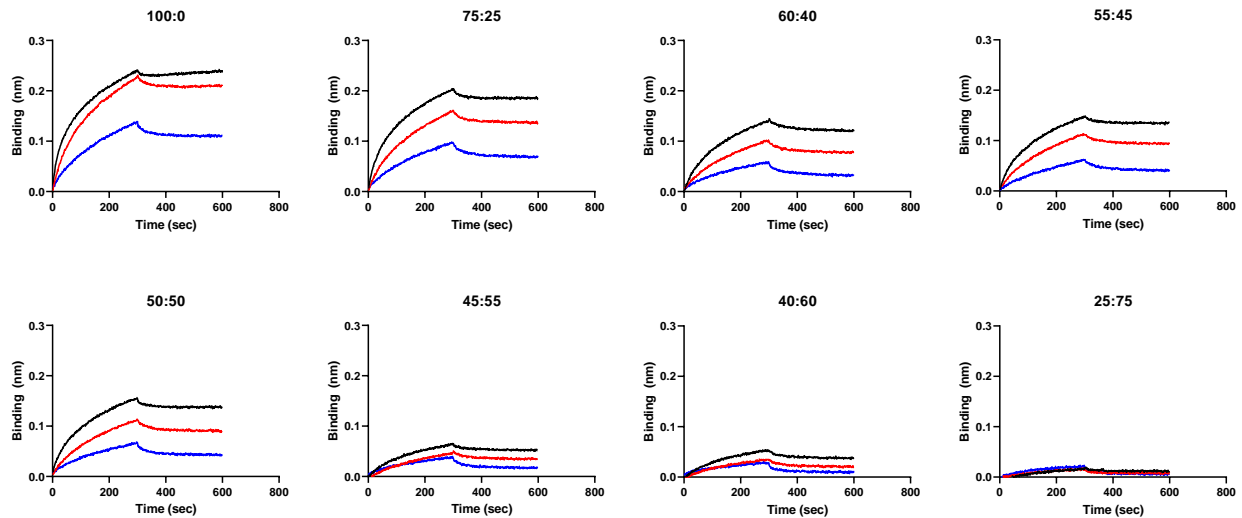


Figure 22. MBL binding to serially mannosylated polystyrene (PS) nanoparticles. 20 nm diameter PS nanoparticles were fully coated in buffer containing varying molar ratios of mannose to galactose. Shown are biolayer interferometry binding and unbinding curves of these particles to immobilized mouse MBL.

3.6 Trafficking and immunogenicity of HA-8mer nanoparticles

We next sought to understand the degree to which other clinically-relevant nanoparticle antigen formulations are affected by MBL-mediated trafficking. First, we started by investigating the trafficking behavior of a self-assembling ferritin nanoparticle bearing eight copies of the influenza hemagglutinin (HA) trimer (HA-8mer)^{95,148,149}. These particles were selected for being structurally similar to the HIV antigen nanoparticles evaluated previously yet bearing unrelated antigens on their surface.

First, we conducted trafficking studies in wild-type and MBL KO mice using dye-labeled HA-8mer delivered subcutaneously as with previous nanoparticle formulations. In wild-type mice, HA-8mer accumulated within draining lymph node follicles, while in MBL KO mice the nanoparticles were diffusely distributed throughout the lymph node seven days post immunization (Figure 23a-b). Similar to our findings with eOD-60mer, antibody titers against HA-8mer were substantially reduced, by ~10-fold, in MBL KO vs. wild-type mice (Figure 23c). An analysis of

germinal centers in these mice revealed that wild-type mice had significantly higher levels of total germinal center B cells as well as antigen-specific germinal center B cells (Figure 23d). However, there was no significant difference between the mean fluorescent intensities of the HA-8mer stain within the antigen-specific germinal center B cell populations between groups (Figure 23e).

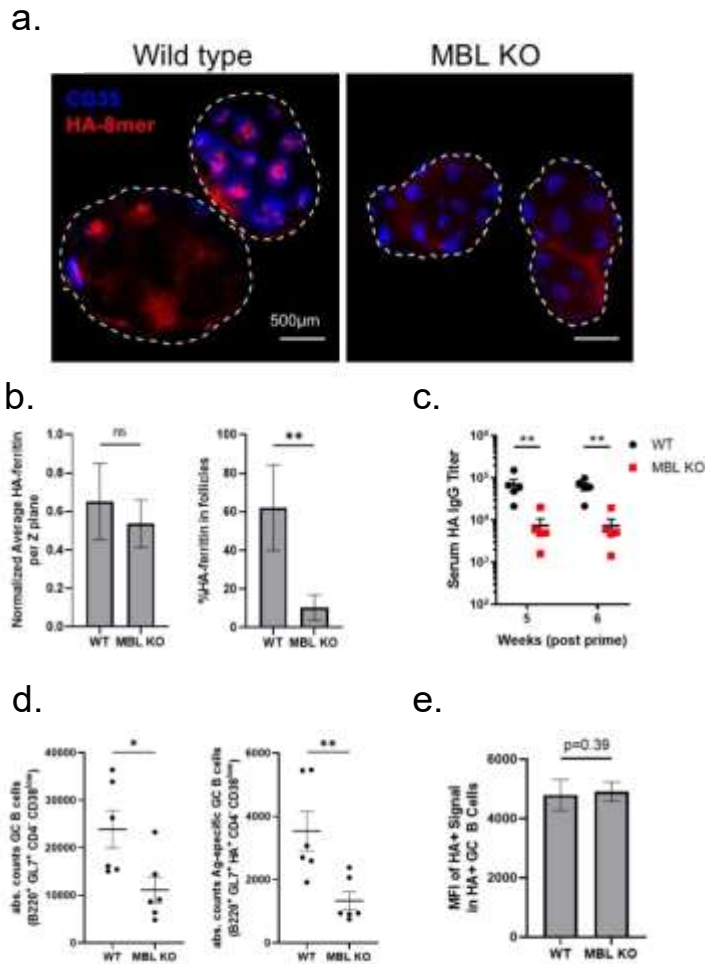


Figure 23. HA-8mer follicular accumulation and immunogenicity are dependent on MBL. **a,b** C57BL/6 (wild type) and MBL KO mice were immunized with 2 µg fluorescent HA-8mer and adjuvant. Draining lymph nodes were recovered after seven days, cleared, and **a** imaged by confocal microscopy. **b** Quantification was performed by determining total HA-8mer signal per Z plane of cleared tissue and percent HA-8mer signal found within follicles. **c-e** C57BL/6 or MBL KO mice were immunized with 5 µg HA-8mer and adjuvant. **c** Serum hemagglutinin-specific IgG titers were analyzed over time by ELISA. **d** Absolute counts of total germinal center B cells and absolute counts of antigen-specific germinal center B cells were determined twelve days after immunization. **e** The average MFI of antigen specificity stain among antigen-specific GC B cells twelve days post immunization. Shown are means and SEM. *p<0.05; **p<0.01; ns=not significant by Mann-Whitney test.

3.7 Trafficking and immunogenicity of HPV16 L1 and HBsAg AD nanoparticles

Next, we examined the capacity of two self-assembling nanoparticle antigens highly similar to those currently used for human vaccinations, human papillomavirus 16 L1 virus-like particles (HPV16 L1)^{150–154} and hepatitis B virus surface antigen AD virus-like particles (HBsAg)^{94,155–157}, to engage with MBL trafficking. Dynamic light scattering confirmed the formation of particles of the anticipated sizes (Figure 24a). By BLI analysis, HPV16 L1 exhibited concentration-dependent binding to immobilized murine MBL, which was greatly reduced following PNGase F treatment (Figure 24b). In contrast, MBL showed no binding toward HBsAg even at high particle concentrations, indicating a lack of high-mannose glycans on the particle surface (Figure 24c).

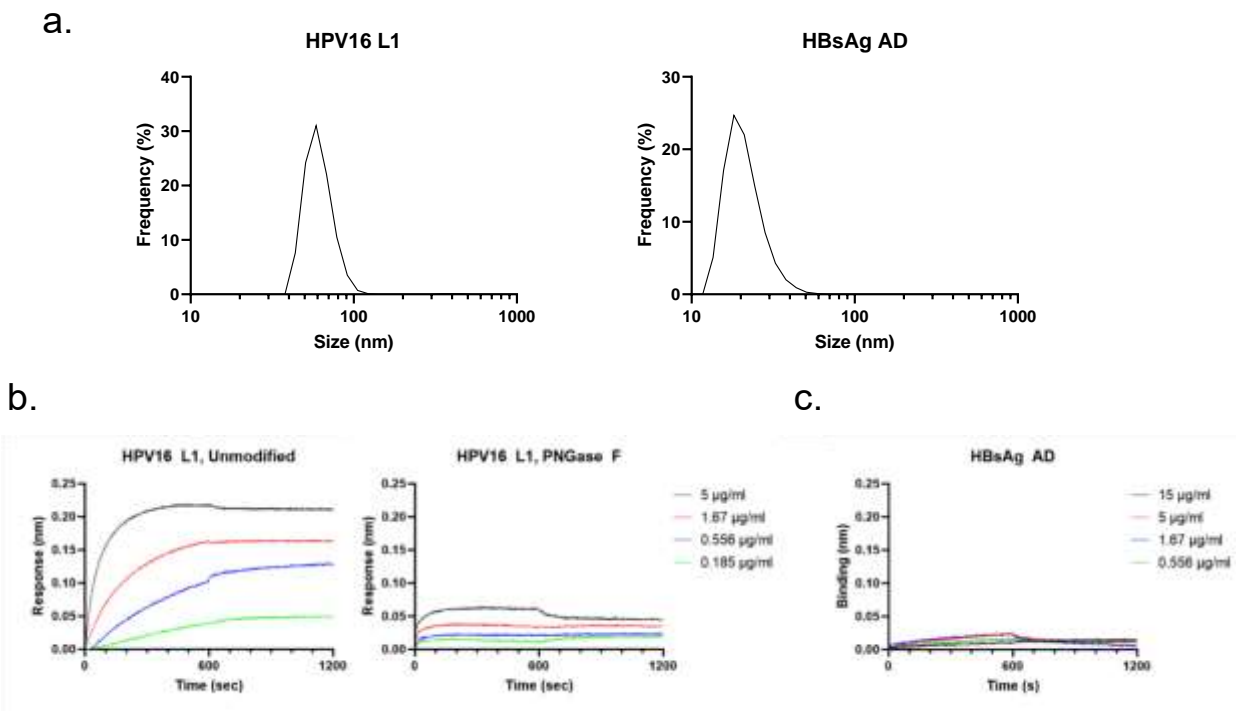


Figure 24. Characterization of HPV16 L1 and HBsAg nanoparticles. **a** Hydrodynamic radii of HPV16 L1 and HBsAg particles as determined by dynamic light scattering. **b,c** Bi-layer interferometry binding and unbinding curves to immobilized mouse MBL of **b** unmodified and PNGase F-treated HPV16 L1 and **c** HBsAg.

Imaging of fluorescently-labeled HPV16 L1 in lymph nodes seven days post immunization revealed follicular accumulation of HPV particles in wild-type but not MBL KO animals (Figure 25a). In a manner distinct from other antigen-bearing nanoparticles evaluated thus far, immunization with HPV16 L1 elicited serum antibody titers that were not statistically different between wild-type and MBL KO mice (Figure 25b). However, total and antigen-specific germinal center B cell populations were reduced by ~50% in MBL KO animals compared to wild-type mice (Figure 25c). Interestingly, fluorescently-tagged HBsAg particles exhibited essentially identical follicular accumulation in both wild-type and MBL KO animals at seven days post immunization (Figure 25d). This prompted us to test whether these particles might be trafficked via complement activation through the alternative pathway, or perhaps trigger complement through natural IgM^{110,158}; HBsAg follicular accumulation remained present in secretory IgM-deficient animals but was lost entirely in C3 KO mice (Figure 25d), suggesting a role for the alternative pathway of complement activation for these nanoparticles. Wild-type and MBL KO mice immunized with HBsAg particles exhibited similar serum antibody responses, while C3 KO mice had reduced IgG titers (Figure 25e). Immunizations with HBsAg also led to substantially greater levels of total and antigen-specific germinal center B cells in wild-type vs. C3 KO animals (Figure 25f).

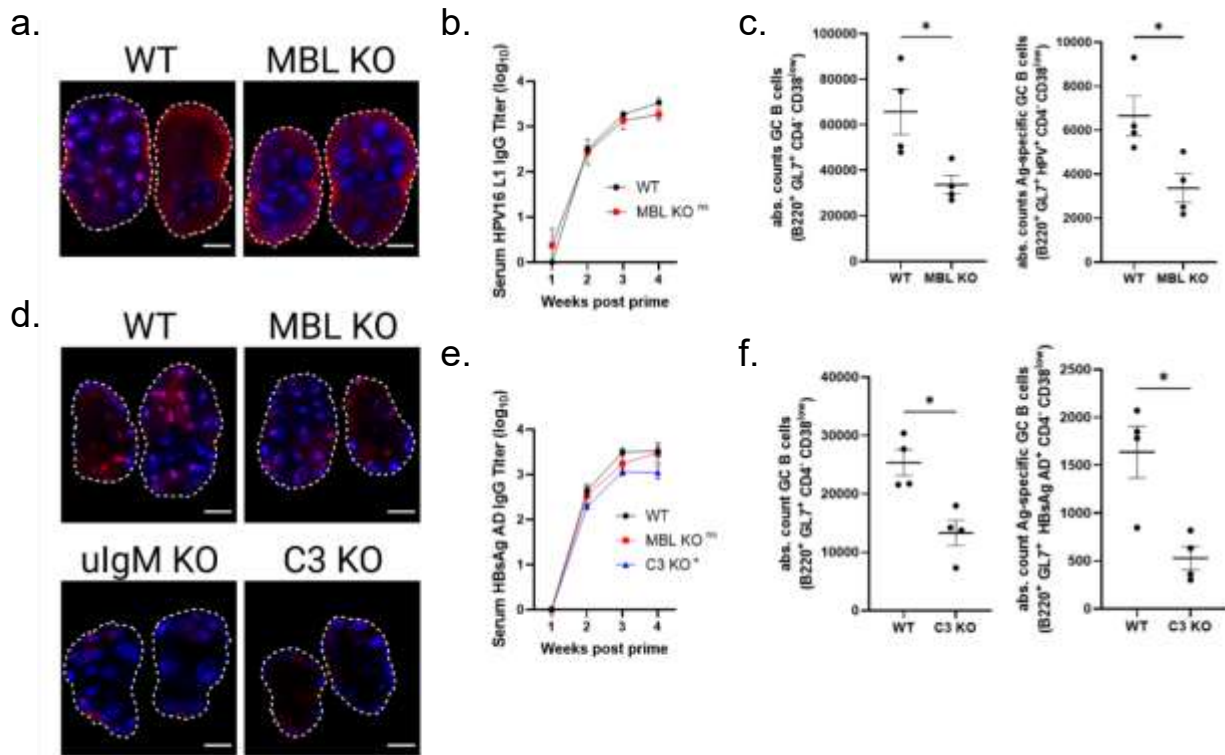


Figure 25. HPV16 L1 and HBsAg nanoparticles exhibit complement-dependent follicular accumulation and immunogenicity. **a** C57Bl/6 mice or MBL KO mice ($n=5/\text{group}$) were immunized with $0.1 \mu\text{g}$ fluorescent HPV16 L1 and saponin adjuvant. 7 days later, lymph nodes were harvested, cleared, and imaged by confocal microscopy. Shown are average intensity Z projections of the tissues; shown is staining for CD35 (blue) and antigen (red), scale bars denote $500 \mu\text{m}$. **b** Serum HPV16 L1-specific IgG titers over time in mice ($n=5/\text{group}$) immunized with $0.1 \mu\text{g}$ HPV16 L1 and saponin adjuvant. Error bars indicate SEM, $p=0.92$ compared to WT one-way ANOVA. **c** Absolute counts of germinal center B cells ($\text{B220}^+\text{GL7}^+\text{CD4}^-\text{CD38}^{\text{low}}$) and antigen-specific germinal center B cells ($\text{B220}^+\text{GL7}^+\text{HPV16 L1}^+\text{CD4}^-\text{CD38}^{\text{low}}$) from WT and MBL KO mice ($n=4/\text{group}$) at day 12 following immunization with $0.1 \mu\text{g}$ HPV16 L1 and saponin adjuvant. Error bars indicate SEM, $p^*<0.05$ by Mann-Whitney test. **d** C57Bl/6 mice or MBL KO mice ($n=5/\text{group}$) were immunized with $5 \mu\text{g}$ fluorescent HBsAg AD and saponin adjuvant. 7 days later, lymph nodes were harvested, cleared, and imaged by confocal microscopy. Shown are average intensity Z projections of the tissues; shown is staining for CD35 (blue) and antigen (red), scale bars denote $500 \mu\text{m}$. **e** Serum HBsAg AD-specific IgG titers over time in mice immunized with $5 \mu\text{g}$ HBsAg and saponin adjuvant. Error bars indicate SEM; *, $p<0.05$ compared to WT by one-way ANOVA followed by Tukey post hoc test. **f** Absolute counts of germinal center B cells and antigen-specific germinal center B cells from WT and MBL KO mice 12 days after immunization with $5 \mu\text{g}$ HBsAg and saponin adjuvant. Error bars indicate SEM, $p^*<0.05$ by Mann-Whitney test.

3.8 Discussion

Here we show that MBL- and complement-mediated recognition of nanoparticles can lead to significantly enhanced accumulation within draining lymph node follicles and that this accumulation is associated with enhanced humoral responses against a variety of clinically important antigens. That both the altered trafficking and immune responses seen in the presence of MBL recognition are observed in multiple, unrelated antigens of multiple designs could provide a generalizable path for enhancing the immunogenicity of many different antigens.

As hypothesized, MBL recognition of eOD-60mer was dependent on the presence of high-mannose glycans on the particle surface. This highlights the glycan specificity by which MBL recognizes surfaces and provides insight into the glycosylation that could be engineering onto a particle to enable MBL-mediated trafficking. However, eOD-60mer coated in primarily complex glycans and treated with endoglycosidase H still exhibited a small degree of follicular localization despite this same eOD-60mer treatment having no MBL recognition *in vitro*. This could be explained by slight differences in glycan recognition between recombinant and native MBL, or by the engagement of other lectins or glycan receptors *in vivo* such as sialoadhesin and intelectins^{159,160}. While the presence of other glycan-specific proteins may have some impact on trafficking, the large reduction in follicular accumulation when only complex glycans were present on eOD-60mer demonstrates the critical nature of high mannose glycans for reliable antigen deposition in follicles.

That non-antigen bearing particles of multiple compositions are able to be trafficked to lymph node follicles when coated with mannose is a very important finding, since it speaks to the generalizability of this mechanism. Since liposomes can traffic through this method, MBL-mediated trafficking could be used to enhance the immunogenicity of membrane-bound antigens, potentially sidestepping some of the work required to make versions of this antigens that are stable *in vivo*. Based on the findings described in this chapter, it seems as though nanoparticles

of arbitrary compositions can be trafficked via MBL with comparable efficacy, meaning that there are far fewer limits on design choices for nanoparticulate antigens in order to take advantage of this mechanism.

Of the three non-HIV immunogen-bearing nanoparticles investigated for MBL recognition and immunogenicity, HA-8mer most closely recapitulated the results observed with eOD-60mer. Follicular accumulation, IgG responses, and germinal center responses were all uniformly enhanced in wild-type mice as compared to MBL KO mice, indicating that not only is MBL-mediated trafficking possible in non-HIV antigen-bearing nanoparticles but that the associated immunological benefits can be present as well. HPV16 L1 was similar, though there was no observable difference in the antibody titers elicited in wild-type and MBL KO mice. It is possible that the reduced impact of MBL on this particle is related to the relatively small portion of HPV26 L1 that is typically glycosylated; most particles are formed within the nucleus where glycans cannot be added, while only a smaller portion are assembled within the cytoplasm and will be glycosylated with high mannose glycans¹⁶¹. HBsAg particles behaved differently than other particles evaluated, going unrecognized by MBL but still trafficking to lymph node follicles in a complement-dependent manner. Given the retention of trafficking in μ gM KO mice and the lack of trafficking in C3 KO mice, it seems as though these particles are especially efficient activators of complement via the alternative pathway, a phenomenon that to our knowledge has not been previously described in HBsAg nanoparticles. Even considering this, the trafficking pattern of these particles highlights the critical role of complement on follicular accumulation on immunogenicity that has been exhibited in all evaluated nanoparticles.

The studies outlined in this chapter cumulatively indicate that MBL-mediated follicular accumulation of nanoparticulate antigen is not specific to a specific class of nanoparticle or type of antigen displayed on those nanoparticles. Instead, it appears that a diverse array of nanoparticle antigens are all capable of being recognized by MBL or by complement directly, and

that this recognition improves both follicular targeting and downstream immune outputs. Additionally, initial experiments undertaken as part of this chapter begin to elucidate the glycosylation requirements needed to engineer this trafficking into model nanoparticles, paving the way for future studies to apply these findings to new nanoparticle antigens for potential clinical development.

3.9 Materials and Methods

Immunogen synthesis

eOD monomer and eOD-60mer were synthesized as before^{50,51}. For eOD monomer synthesis, plasmids were transiently transfected into Expi293 cells (ThermoFisher Scientific). After 5 days, cell culture supernatants were collected and protein was purified in an ÄKTA pure chromatography system using HiTrap HP Ni sepharose affinity column, followed by size exclusion chromatography using Superdex 75 Increase 10/300 GL column (GE Healthcare Life Sciences). Endotoxin levels in purified protein was measured using Endosafe Nexgen-PTS system (Charles River) and assured to be < 5EU/mg protein. eOD-60mer was produced via the same method, except that unless otherwise indicated kifunensine was included in the cell media and the size exclusion chromatography was performed used a Superose 6 column (GE Healthcare)

Synthesis of saponin adjuvant

The adjuvant used for all the described studies was an ISCOM-like nanoparticle comprised of self-assembled cholesterol, phospholipid, and Quillaja saponin prepared as previously described¹²³; all synthesis was performed under sterile conditions with sterile reagents. Briefly, 10 mg each of cholesterol (Avanti Polar Lipids 700000) and DPPC (Avanti Polar Lipids 850355) were dissolved separately in 20% MEGA-10 (Sigma D6277) detergent at a final concentration of 20 mg/ml and 50 mg Quil-A saponin (Invivogen vac-quil) was dissolved in MQ water at a final concentration of 100 mg/ml. Next, DPPC solution was added to cholesterol followed by addition of Quil-A saponin in rapid succession and the volume was brought up with

PBS to a final concentration of 1 mg/ml cholesterol and 2% MEGA-10. The solution was allowed to equilibrate at 25 °C overnight, followed by 5 days of dialysis against PBS using a 10k MWCO membrane. The adjuvant solution was then filter sterilized using a 0.2 µm Supor syringe filter, concentrated using 50k MWCO centricon filters, and further purified by FPLC using a Sephacryl S-500 HR size exclusion column. Each adjuvant batch was finally characterized by negative stain TEM and DLS to confirm uniform morphology and size and validated for low endotoxin by Limulus Amebocyte Lysate assay (Lonza QCL-1000). Final adjuvant concentration was determined by cholesterol quantification (Sigma MAK043).

Immunizations

C57BL/6, MBL KO, C3 KO, Cr1/2 KO, B6129SF2/J, and µIgM KO mice were purchased from Jackson Laboratory (Bay Harbor, ME). Mice were housed under specific pathogen-free conditions. All procedures used in this study were approved by the Committee on Animal Care at the Massachusetts Institute of Technology following local, state, and federal regulations.

Female mice age 6-10 weeks of age were immunized with immunogen and adjuvant via subcutaneous tail-base injection with 50 µl on either side of the tail. Mice immunized with eOD or eOD-60mer received a total of 2 µg eOD, mice immunized with HA-8mer and HBsAg AD received 5 µg total protein, and mice immunized with HPV16 L1 received a 0.1 µg total protein. All immunizations included 5 µg saponin adjuvant. For trafficking studies, mice were similarly immunized with AlexaFluor 647-tagged immunogens (ThermoFisher A21086). Immunogens were characterized by UV-vis spectroscopy and contained approximately 1 dye per monomeric eOD, 40 dyes per eOD-60mer particle, 45 dyes per HA-8mer particle, and 50 dyes per HPV16 L1 and HBsAg AD particle. Mice were then injected subcutaneously in the tail base with 4 µg BV421-labeled anti-CD35 (BD Biosciences 740029) 18-24 hours prior to lymph node excision to label follicles *in situ*.

Whole lymph node imaging

Mice were sacrificed by carbon dioxide inhalation and both inguinal lymph nodes were harvested at the specified days. Lymph nodes were immediately placed into PBS containing 4% paraformaldehyde overnight and were then washed twice in PBS.

Imaging was performed using an IVIS spectrum optical imaging system. All lymph nodes were imaged at the same time using automatically determined imaging settings based on the fluorescence of the nodes. Background subtraction was performed based on an empty portion of the image. The MFI of each pair of lymph nodes was determined using an identically sized gate, and the MFI of a pair of lymph nodes from an unimmunized mouse was subtracted from the MFIs of experimental mice to correct for lymph node autofluorescence.

Lymph node processing and imaging for immunofluorescence microscopy

Lymph nodes were excised from mice and immediately placed in OCT. Nodes were then flash frozen using liquid nitrogen to prevent antigen leakage. Frozen lymph node blocks were sliced into 100 μm thick sections using a cryomicrotome. For each node, six slices were obtained and mounted onto slides. Slides were stored at $-80\text{ }^{\circ}\text{C}$.

Lymph nodes were imaged using a Leica SP8 Laser Scanning Confocal Microscope. Lasers were set to minimize pixel saturation in the brightest samples in each experiment. All laser and channel settings were then kept constant across each individual studies to allow for direct comparison between different samples.

Germinal center analysis

Mice were sacrificed by carbon dioxide inhalation and both inguinal lymph nodes were harvested at the specified days. Lymph nodes were processed into single-cell suspensions by mechanical digestion followed by passage through a 70 μm cell strainer (BD Biosciences) twice. Next, cells were washed with PBS and stained with Live/Dead Aqua (Life Technologies) for 15 minutes at room temperature. Samples were then treated with anti-CD16/32 Fc block (BioLegend 14-0161-85), followed by staining with anti-B220-PE-Cy7 (BioLegend 103222), anti-CD4-BV711

(BioLegend 100550), anti-GL7-PerCP/Cy5.5 (BioLegend 144610), anti-CD38-AF488 (BioLegend 102714), and antigen-bearing nanoparticles separately with Pacific Blue and AF647. Excess staining reagents were washed off and cells were analyzed via a BD FACSCelesta flow cytometer.

Antibody titer analysis

Blood samples were collected from immunized mice via retro-orbital bleeds and serum was isolated. MaxiSorp plates (ThermoFisher 44-2404-21) were coated with 2 µg/ml immunogen and blocked overnight in PBS containing 1% BSA. Plates were washed four times in PBS containing 0.2% Tween-20, and dilutions of serum in blocking buffer were added and incubated for two hours. Plates were washed as before and an HRP-conjugated anti-mouse IgG was added and incubated for one hour. Plates were washed and TMB was added. The reaction was stopped with sulfuric acid once the wells containing the lowest dilutions of TMB began to develop visually or after 20 minutes and the absorbance of each well was determined. All titers reported are inverse dilutions were $A_{450\text{nm}} - A_{540\text{nm}}$ (reference wavelength) equals 0.5.

Antigen deglycosylation

Nanoparticle immunogens were deglycosylated using PNGase F (New England BioLabs P0704S) or endoglycosidase H (New England BioLabs P0702S) under non-denaturing conditions following the manufacturer's guidelines. Deglycosylation was confirmed via SDS-PAGE gel using glycoprotein stain (ThermoFisher 24562). Retention of particle structure was confirmed via dynamic light scattering.

Bio-layer interferometry

All bio-layer interferometry measurements were conducted using a ForteBio Octet RED96 instrument in the MIT Biophysical Instrumentation Facility. Streptavidin-coated sensors were incubated in PBS containing 1% BSA and 0.1 M CaCl and were then loaded into wells of the same solution containing 1 µg/ml biotinylated murine MBL2 for one minute. Excess MBL was

washed off and MBL-coated biosensors were moved to wells containing dilutions of antigen formulations until probes began to become saturated. The biosensors were then moved back to the baseline solution and antigen was allowed to dissociate.

Lymph node processing and imaging for whole-tissue confocal microscopy

Lymph nodes were excised from mice and fixed overnight at 4 °C in 4% paraformaldehyde. Lymph nodes were then processed as previously described⁹⁰. Briefly, nodes were washed twice in PBS and excess fat and connective tissue were removed. Nodes were then gradually moved into solutions containing successively high concentrations of methanol over the course of several hours until they were incubated for half an hour in pure methanol. Nodes were then briefly bleached in hydrogen peroxide solution for one minute before being returned to methanol for half an hour. They were then gradually moved into solutions containing increasing concentrations of tertiary-butanol before being incubated in pure tertiary-butanol for one hour. All solutions used after bleaching contained an additional 0.4% α -tocopherol. Nodes were then removed from solution and allowed to dry completely before being placed in dichloromethane. After lymph nodes dropped to the bottom of tubes following swirling, indicating the removal of remaining tertiary-butanol, they were stored in dibenzyl ether, which was used as an optical clearing solution.

Lymph nodes were imaged using an Olympus FV1200 Laser Scanning Confocal Microscope. Lasers were set to minimize pixel saturation in the brightest samples in each experiment. All laser and channel settings were then kept constant across each individual studies to allow for direct comparison between different samples. Each lymph node was imaged over 360 μm . For studies comparing the total number of antigen-positive follicles, channel settings were increased to allow for imaging through the entire height of the lymph node regardless of signal saturation.

Microscopy images were analyzed using ImageJ as previously described⁹⁰. To reduce background signal bleed, the antigen channel was passed through an HSB filter against background fluorescence. Z-stacks were then condensed into average intensity projections ranging over the full 360 μm displaying the average intensity of each color for each pixel.

To quantify immunogen signal and follicle colocalization, the maximum intensity z-projection on all channels was binarized and used to define a selection comprising the whole lymph node area. Next, for each z slice a high-pass filter was applied such that the brightest pixels in the background autofluorescence channel were binarized. These bright pixels in the autofluorescence channel were zeroed in the signal channels to mitigate the intensity effects of bleed-through from autofluorescence into the signal channels. A sum intensity z-projection on the CD35 channel was binarized and used to define a selection comprising the follicular area. A sum intensity z-projection on the immunogen channel was then binarized using a high pass filter such that bright pixels were applied an intensity value of 1, while dim pixels were applied an intensity value of 0. This binary mask was used to multiply a sum intensity z-projection such that all dim pixels were zeroed while all bright pixels retained their unaltered intensity information. The intensity of these bright pixels was measured within both the whole lymph node and follicular areas for use in ratiometric antigen signal intensity calculations.

Statistics

Statistical analyses were performed using GraphPad Prism software. All values and errors bars are shown as mean \pm standard error. Data was analyzed using Mann-Whitney tests or ordinary one-way ANOVA followed by a Tukey's post-test to compare multiple groups as noted.

4. DNA origami for probing nanoparticle vaccine design parameters

4.1 Introduction

Most of the work in this thesis is focused on the use of nanoparticle immunogens formed by protein self-assembly, which have the advantage of being well characterized and well tolerated *in vivo*. However, varying the properties of protein particles can be difficult in many key ways. For example, particle size is typically fixed for each particle system, meaning that any comparisons between nanoparticles of different sizes and shapes also necessitates comparing particles with greatly varying amino acid sequences and structures. The ability to select individual nanoparticle parameters to vary is limited, hindering attempts to determine which specific parameters are of greatest importance to the design of nanoparticulate vaccines. To systematically interrogate the relative importance factors such as nanoparticle shape and size and antigen density and surface location, a modular nanoparticle platform is needed.

One technology uniquely positioned to be used to probe this parameter space is DNA origami. DNA origami (or DNA nanotechnology) is based on self-assembly of double-stranded DNA into arbitrary, complex, three-dimensional structures through complementary strand base pairing.^{162,163} In one particularly successful version of this technology, a long single-stranded DNA, referred to as the scaffold strand, is folded into a specific three-dimensional conformation using hundreds of short DNA oligonucleotides, referred to as staple strands. Because the scaffold and staple strands can be designed and customized on a base pair by base pair basis, there is enormous potential to create structures varied in size, shape, and location and type of functionalization sites^{164–168}. In this chapter, we utilize this technology to investigate the role of particle shape, particle functionalization, and antigen density on a nanoparticulate antigen's ability to activate B cells. This work was done in collaboration with the MIT Lab for Nucleic Acid Nanotechnology, primarily working with Eike-Christian Wamhoff, Grant Knappe, and Anna

Romanov, who designed and synthesized the DNA origami structures described in subsequent subchapters.

4.2 *In vitro* validation of eOD-conjugated DNA nanoparticles

A pentagonal bipyramid DNA particle with edge lengths of 84 base pairs (PB84) was synthesized as previously described¹⁶⁹ (Figure 26a). The HIV Env germline targeting antigen eOD was attached to the particles by first covalently attaching a peptide nucleic acid (PNA) complementary to single-stranded DNA overhangs on the PB84 scaffold to the eOD (forming eOD-PNA) and then incubating the eOD-PNA with the PB84 to allow for hybridization (Figure 26b,c). eOD-functionalized particles were purified by centrifugation, resulting in DNA origami particles decorated with 40 copies of eOD (PB84-40x).

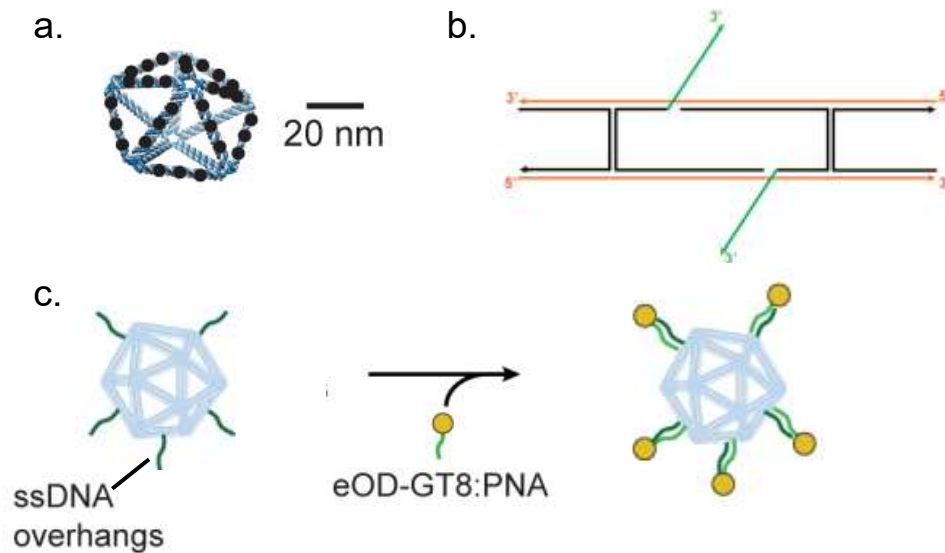


Figure 26. Design and hybridization of DNA nanostructures. **a** PB84 DNA nanostructure (blue) with hybridization sites (black dots). **b** Secondary structure of an edge of a DNA nanostructure. Shown are the scaffold strands (red), staple strands (black), and DNA overhangs for hybridization (green). **c** Overview of the antigen conjugation protocol to attach eOD to DNA nanostructures using PNA single strands complementary to single stranded DNA overhangs on the nanostructures.

To evaluate the capacity of the DNA particles to activate B cells, Ramos B cells expressing germline reverted VRC01 B cell receptors (the cognate receptor that binds to the eOD antigen)^{170,171} were loaded intracellularly with a calcium sensor dye and incubated with eOD monomer, eOD-60mer protein nanoparticles, or DNA nanostructures. Increases in fluorescence indicate release of calcium from the endoplasmic reticulum of the cells following antigen-B cell receptor binding¹⁷². A range for antigen concentrations for this assay was determined by titrating eOD-60mer across several orders of magnitude, which confirmed that B cell calcium flux signal was antigen concentration dependent as anticipated (Figure 27a,b). Our studies found that PB84-40x was able to robustly initiate calcium flux in B cells *in vitro* to a degree approaching the stimulus provided by an equivalent molar concentration of eOD presented on eOD-60mer, but eOD monomer or PB84 DNA particles lacking eOD (PB84-0x) failed to elicit any response (Figure 27c,d). Importantly, the lack of a response from eOD monomer indicates the importance of multivalency for eliciting strong B cell receptor engagement.

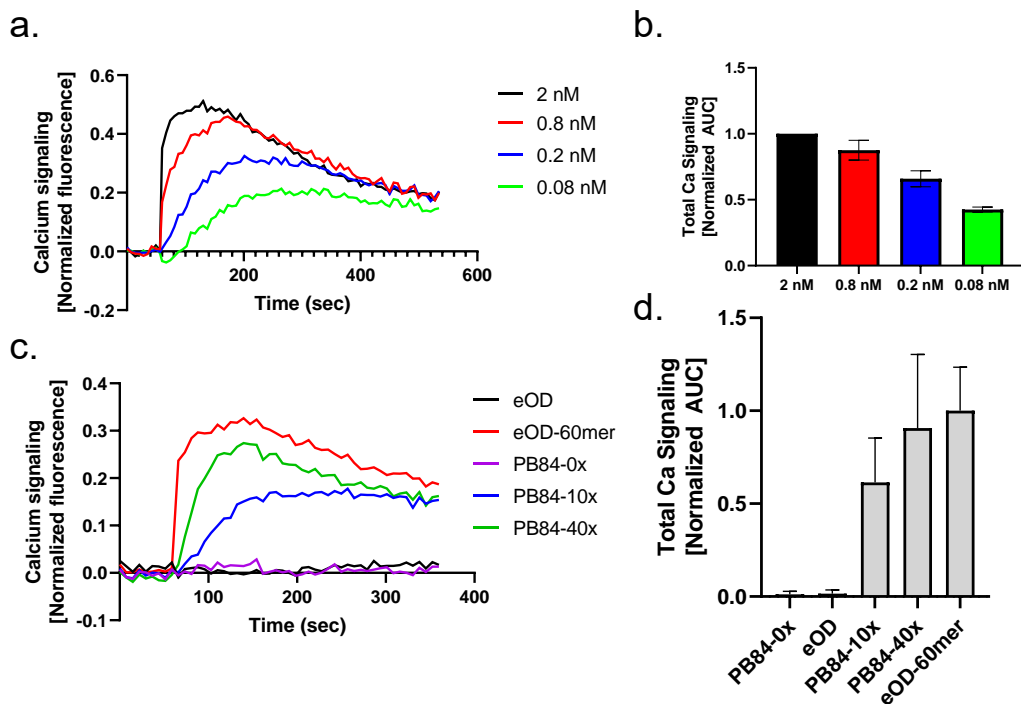


Figure 27. Calcium signaling is antigen concentration and density dependent. **a,b** Germline VRC01-expressing Ramos B cells were loaded with Fluo-4 calcium sensitive dye, and eOD-60mer at varying concentrations was washed over the cells. Subsequent calcium flux was detected as increase in fluorescence from the cells and is shown as **a** representative normalized fluorescence changes over time and **b** average area-under-the-curve (AUC) of three independent repeats normalized to the maximum response among all samples in a repeat. Shown are averages and SEM. **c,d** Germline VRC01 Ramos B cells were stained with Fluo-4 calcium sensitive dye and eOD-displaying nanoparticles were washed over the cells at a concentration of 1 nM eOD. Subsequent calcium flux was detected as increase in fluorescence from the cells and is shown as **c** representative normalized fluorescence changes over time and **d** average area-under-the-curve (AUC) of three independent repeats normalized to the maximum response among all samples in a repeat. Shown are averages and SEM.

4.3 Activation of B cells by varied DNA nanostructures

To test whether the robust calcium flux observed with PB84-40x was specific to this particular DNA particle structure, an icosahedral DNA particle with edge lengths of 52 base pairs (I52) was synthesized and conjugated with 30 copies of eOD (I52-30x) utilizing the same PNA-based hybridization technique (Figure 28). When compared in a calcium flux assay against eOD-60mer and PB84-40x, I52-30x was found to activate B cells to a similar degree as both other nanoparticle formulations (Figure 29a,b). However, at lower antigen concentrations eOD-60mer

induced significantly more signaling than either DNA particle, and I52-30x induced significantly more than PB84-40x (Figure 29c,d). These results suggest that at high antigen concentrations, small differences in particles geometry and antigen spacing are unlikely to have a major impact on B cell responses, but that such changes become increasingly impactful as antigen concentrations are reduced.

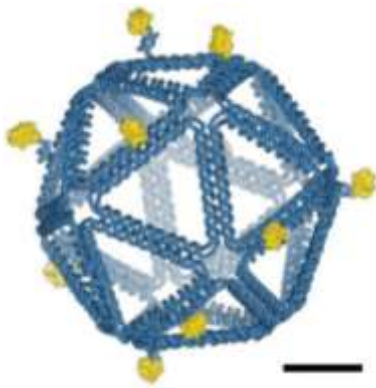


Figure 28. I52 DNA nanostructure schematic. Cartoon rendering of an icosahedral DNA nanoparticle displaying ten copies of eOD-PNA (yellow). Scale bar, 10nm.

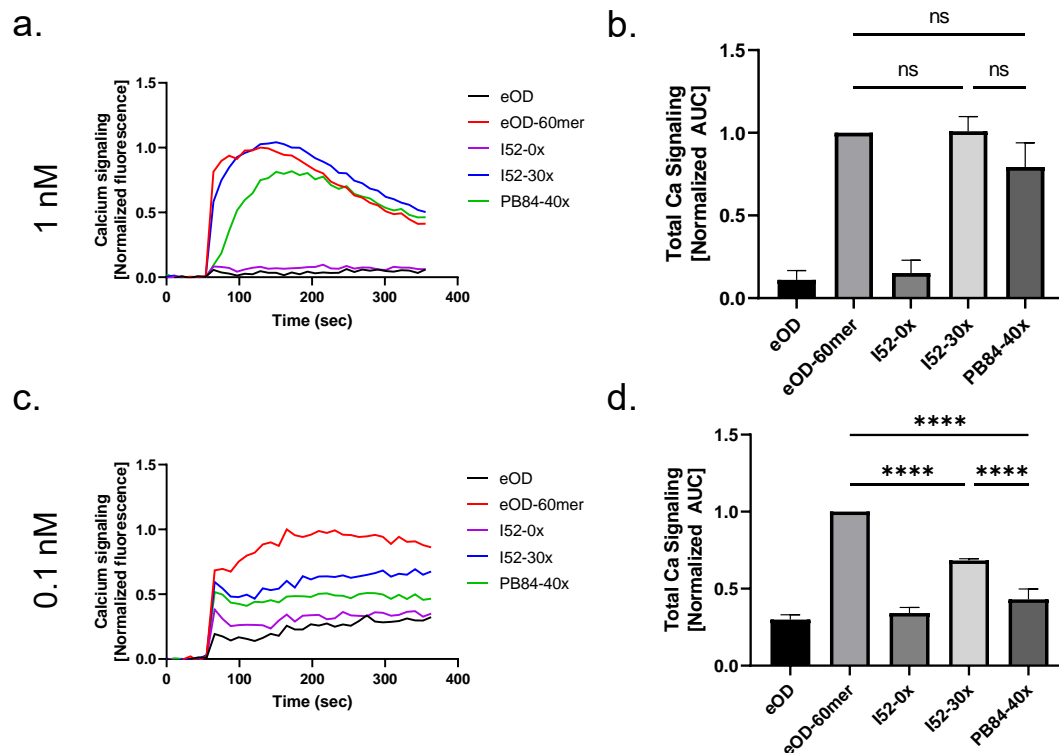


Figure 29. Multiple DNA particle geometries can induce calcium signaling. **a,b** Germline VRC01-expressing Ramos B cells were loaded with Fluo-4 calcium sensitive dye, and eOD-displaying nanoparticles were washed over the cells at a molar eOD equivalent concentration of 1 nM. Subsequent calcium flux was detected as increase in fluorescence from the cells and is shown as **a** representative normalized fluorescence changes over time and **b** average area-under-the-curve (AUC) of three independent repeats normalized to the maximum response among all samples in a repeat. Shown are averages and SEM. **c,d** Germline VRC01 Ramos B cells were stained with Fluo-4 calcium sensitive dye and eOD-displaying nanoparticles at were washed over the cells at a molar eOD equivalent of 0.1 nM. Subsequent calcium flux was detected as increase in fluorescence from the cells and is shown as **c** representative normalized fluorescence changes over time and **d** average area-under-the-curve (AUC) of three independent repeats normalized to the maximum response among all samples in a repeat. Shown are averages and SEM. **** $p < 0.0001$; ns=not significant by one-way ANOVA followed by Tukey's multiple comparisons test.

4.4 Antigen density dependence of *in vitro* antigen-specific B cell activation

For initial experiments into the effect of antigen density and spacing on B cell activation, another DNA nanostructure, six DNA helices bundled into a rigid rod (6HB), was synthesized. This structure has the advantage of being able to place two eOD proteins on the particle at varied lengths across the rod, allowing for a minimalist approach to investigating the effect of antigen spacing. Our studies found that, despite the prevalent dogma in the field that minimizing antigen spacing will increase B cell activation, calcium flux actually increased as eOD spacing was increased from 14 to 80 nm (Figure 30a,b). This finding has potentially important implications for the design of future nanoparticle vaccines.

While antigen spacing is an important factor, we also found that antigen copy number on each particle has an important impact on B cell activation. Both PB84 and I52 were produced with a smaller than maximum copy number of eOD on their surface, and when compared in a calcium flux assay against PB84-40x or I52-30x they elicited weaker responses (Figure 30c-f). These data in combination with the 6HB data suggest there likely exists a point of antigen density in which further antigen addition would add antigens within a less effective distance of one another.

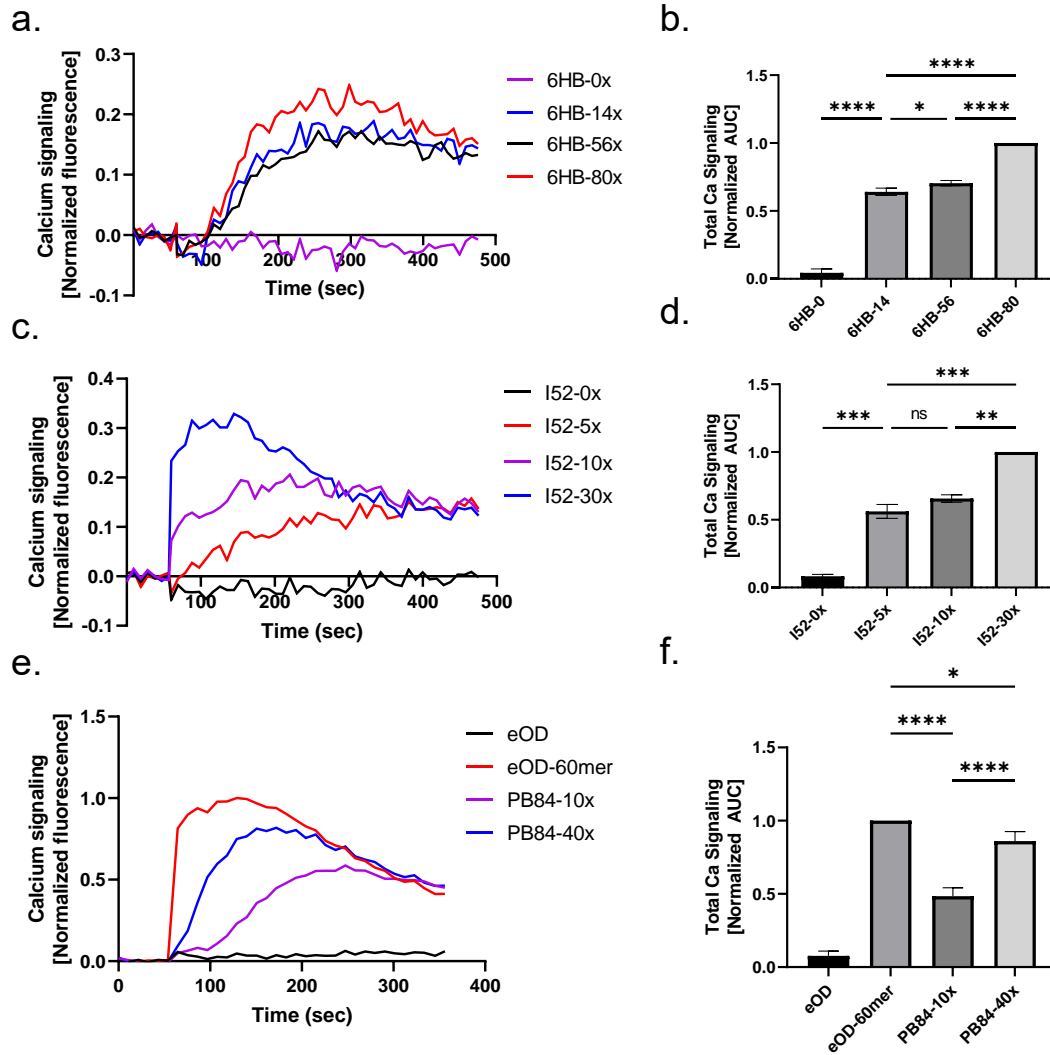


Figure 30. Antigen spacing and density significantly alter calcium signaling. **a,b** Germline VRC01-expressing Ramos B cells were loaded with Fluo-4 calcium sensitive dye, and eOD-displaying 6HB rods were washed over the cells at a molar eOD equivalent concentration of 5 nM. Subsequent calcium flux was detected as increase in fluorescence from the cells and is shown as **a** representative normalized fluorescence changes over time and **b** average area-under-the-curve (AUC) of three independent repeats normalized to the maximum response among all samples in a repeat. Shown are averages and SEM. **c,d** Germline VRC01-expressing Ramos B cells were loaded with Fluo-4 calcium sensitive dye, and eOD-displaying I52 nanoparticles were washed over the cells at a molar eOD equivalent concentration of 5 nM. Subsequent calcium flux was detected as increase in fluorescence from the cells and is shown as **c** representative normalized fluorescence changes over time and **d** average area-under-the-curve (AUC) of three independent repeats normalized to the maximum response among all samples in a repeat. Shown are averages and SEM. **e,f** Germline VRC01-expressing Ramos B cells were loaded with Fluo-4 calcium sensitive dye, and eOD-displaying PB84 nanoparticles were washed over the cells at a molar eOD equivalent concentration of 1 nM. Subsequent calcium flux was detected as increase in fluorescence from the cells and is shown as **e** representative normalized fluorescence changes over time and **f** average area-under-the-curve (AUC) of three independent repeats normalized to the maximum response among all samples in a repeat. Shown are averages and SEM. * $p < 0.05$; ** $p < 0.01$; *** $p < 0.001$; **** $p < 0.0001$; ns=not significant by one-way ANOVA followed by Tukey's multiple comparisons test.

4.5 Effect of stabilization and antigen attachment method on B cell activation

DNA origami use *in vivo* has historically been limited by rapid degradation of DNA particles by pH and ion concentration changes and by the numerous DNases present in serum, particularly DNase I¹⁶⁴. Multiple stabilization strategies have been developed to protect DNA structures from these environmental hazards, including envelopment in lipid bilayers or viral capsid proteins or coating with various dendrons and cationic polymers^{173–179}. However, many of these strategies result in significant changes to the outer surface of the structure and could bury antigens displayed on the particle.

We sought to evaluate the degree to which B cell activation was altered by DNA particle stabilization using two different techniques: coating DNA particles with an oligolysine-PEG copolymer that binds via electrostatic interactions, or coating particles with DAPI, a small molecule that can bind to adenine-thymine-rich regions of the DNA structure. These methodologies were chosen for their predicted minimal impact on the accessibility of eOD to B cell receptors. I52-30x nanoparticles stabilized in these ways were found to activate B cells roughly equivalently to unstabilized I52-30x and eOD-60mer at 5 nM (Figure 31a,b), but at 1 nM eOD concentration the stabilized particles induced lesser calcium flux signals than eOD-60mer (Figure 31c,d). These results suggest a slight hindrance of B cell recognition of displayed eOD when particles are stabilized, though the ultimate effect of this hindrance *in vivo* remains unclear.

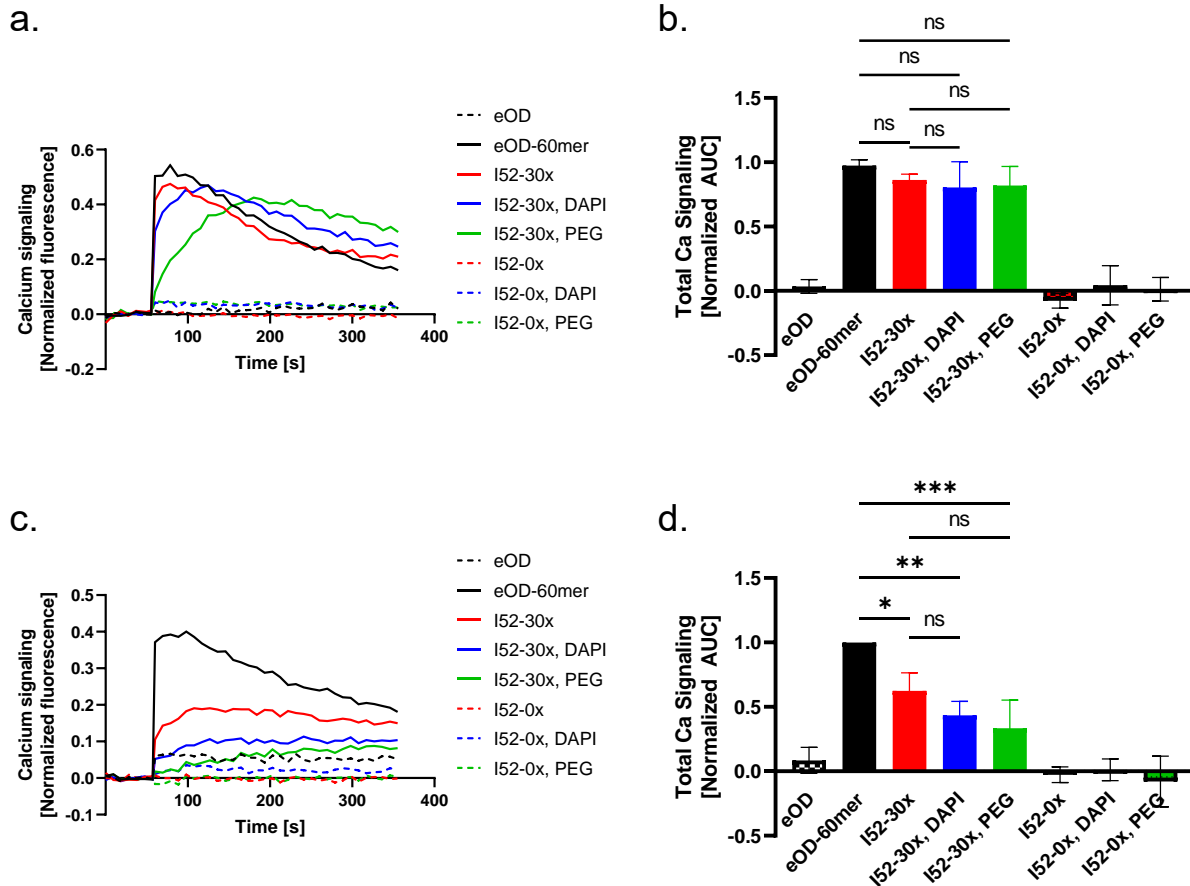


Figure 31. DNA nanoparticle stabilization can alter calcium signaling at low antigen concentrations. **a,b** Germline VRC01-expressing Ramos B cells were loaded with Fluo-4 calcium sensitive dye, and eOD-displaying nanoparticles with or without additional nanoparticle stabilization were washed over the cells at a molar eOD equivalent concentration of 5 nM. Subsequent calcium flux was detected as increase in fluorescence from the cells and is shown as **a** representative normalized fluorescence changes over time and **b** average area-under-the-curve (AUC) of three independent repeats normalized to the maximum response among all samples in a repeat. Shown are averages and SEM. **c,d** Germline VRC01-expressing Ramos B cells were loaded with Fluo-4 calcium sensitive dye, and eOD-displaying nanoparticles with or without additional nanoparticle stabilization were washed over the cells at a molar eOD equivalent concentration of 1 nM. Subsequent calcium flux was detected as increase in fluorescence from the cells and is shown as **c** representative normalized fluorescence changes over time and **d** average area-under-the-curve (AUC) of three independent repeats normalized to the maximum response among all samples in a repeat. * $p < 0.05$; ** $p < 0.01$; *** $p < 0.001$; ns=not significant by one-way ANOVA followed by Tukey's multiple comparisons test.

We also investigated different methods for attaching eOD to DNA particles. We hypothesized that the hybridization method could be susceptible to dehybridization *in vivo* in the presence of serum and so developed an alternative method to coat eOD using azide-DBCO conjugation chemistry¹⁸⁰ (Figure 32a). However, the hybridization method has the potential benefit of including a flexible linker between the DNA scaffold and the antigen, potentially allowing for more degrees of conformational flexibility and improved access to binding sites for B cell receptors than the covalent scheme would permit. I52-30x made via hybridization or covalent conjugation were compared in a calcium flux assay and found to activate B cells equivalently (Figure 32b,c), demonstrating that *in vitro* both methods of attaching eOD to particles are effective. Future *in vivo* studies are required to compare the efficacy of these strategies in live animals, where differences in antigen flexibility and the long-term stability of antigen-nanoparticle binding may be more relevant.

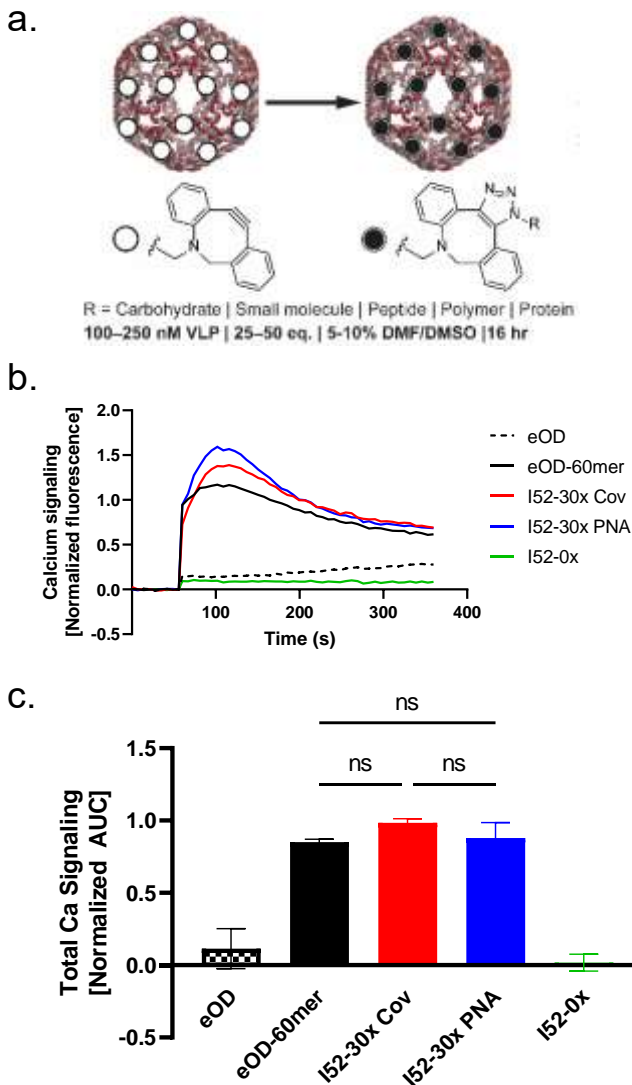


Figure 32. B cell calcium flux is indifferent to mode of antigen attachment to DNA nanoparticles. **a** Schematic of covalent conjugation strategy. Staple strands of the DNA nanostructure contain overhangs displaying DBCO (sites shown in white), which can then be reacted with an azide-functionalized eOD to covalently bind eOD to the functionalization sites of the DNA particle. **b,c** Germline VRC01-expressing Ramos B cells were loaded with Fluo-4 calcium sensitive dye, and eOD-displaying nanoparticles, including DNA nanoparticles with eOD attached via direct covalent conjugation (Cov) and DNA nanoparticles with eOD attached via PNA hybridization (PNA), were washed over the cells at a molar eOD equivalent concentration of 5 nM. Subsequent calcium flux was detected as increase in fluorescence from the cells and is shown as **b** representative normalized fluorescence changes over time and **c** average area-under-the-curve (AUC) of three independent repeats normalized to the maximum response among all samples in a repeat. Shown are averages and SEM. ns=not significant by one-way ANOVA followed by Tukey's multiple comparisons test.

4.6 Preliminary *in vivo* studies of eOD-conjugated DNA nanoparticles

Given the efficacy exhibited by eOD-displaying DNA nanostructures *in vitro*, we sought to determine if they could elicit humoral immune responses *in vivo* as well. We selected nanostructures decorated with eOD via the hybridization method as the first to test, as this is a commonly used technique in the field and was the strategy most extensively studied through calcium flux assays.

We first conducted a study to determine if immunization with DNA particles could generate eOD-specific antibodies. An eOD dose of 100 ng was chosen such that monomer eOD would fail to seroconvert most mice immunized with it, in the hopes that this would allow for clear determination of how DNA particles compared to both eOD monomer and eOD-60mer. Following subcutaneous immunization, mice immunized with eOD-60mer elicited strong responses as had previously been observed, but all DNA nanostructures failed to generate detectable antibody levels against either eOD or the DNA scaffold regardless of the type of DNA stabilization used (Figure 33a). Germinal center and T_{fh} responses in mice immunized with eOD-bearing DNA nanostructures were also lower than those of mice immunized with eOD-60mer and trended lower than those of mice immunized with monomer eOD (Figure 33b,c). Notably, however, the germinal center responses against all three eOD-bearing nanoparticle formulations were above non-eOD-bearing controls, indicating some small degree of immune activation and suggesting that these nanoparticles were capable of eliciting at least a weak immune response.

There were several possible explanations for why the DNA particles failed to elicit an antibody response. They could have been broken down rapidly *in vivo* by DNases, the eOD could have dehybridized and effectively become monomeric, and/or the particles could have become entrapped in the highly charged cellular matrix at the site of injection. As a next step, we immunized mice intraperitoneally; this mode of injection allows injected materials to rapidly flush into the spleen, and thereby circumvents potential interference from the extracellular matrix. Following a prime and boost through the intraperitoneal route, several mice from the DNA nanoparticle groups did seroconvert, indicating that these particles do have the potential to generate antigen-specific antibody responses (Figure 32d). However, the only formulation to successfully seroconvert all mice and elicit detectable antibody responses significantly above that elicited by eOD monomer was eOD-60mer, suggesting that despite stabilization and altered route of administration the DNA nanostructures were still not able to generate enhanced immune responses as might be expected from particle delivery of antigen. Thus, while these eOD-DNA

nanoparticles displayed significant efficacy in *in vitro* studies, more work is needed to successfully translate them for use in *in vivo* studies.

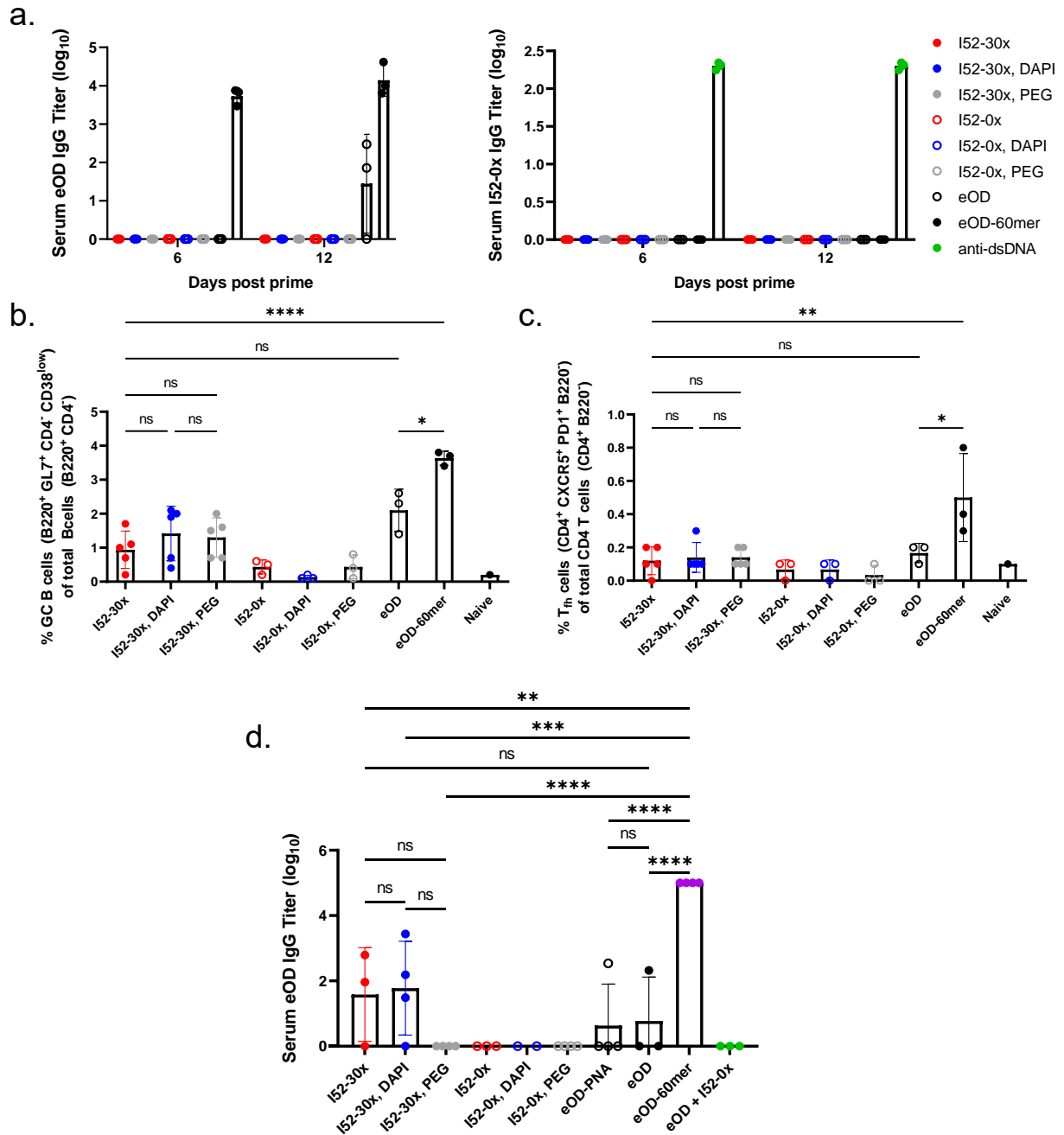


Figure 33. eOD-displaying DNA nanoparticles elicit weak immune responses following subcutaneous and intraperitoneal immunization. a-c C57BL/6 mice were immunized subcutaneously with eOD-displaying DNA nanoparticles and other eOD formulations, each containing 100 ng eOD with adjuvant. a Serum was collected at 6 and 12 days post immunization and analyzed for anti-eOD and anti-DNA scaffold antibodies. An anti-doubled stranded DNA assay control (anti-dsDNA) was used to validate the assay to detect anti-DNA scaffold antibodies. 12 days post immunization draining lymph nodes were removed and analyzed for b germinal center B cell and c follicular helper T cell responses. d C57BL/6 mice were immunized intraperitoneally with eOD-displaying DNA nanoparticles and other eOD formulations, each containing 100 ng eOD with adjuvant and were boosted with identical formulations 14 weeks later. Serum was collected 6 weeks post boost and analyzed for anti-eOD antibodies. * $p < 0.05$; ** $p < 0.01$; *** $p < 0.001$; **** $p < 0.0001$; ns=not significant by one-way ANOVA followed by Tukey's multiple comparisons test.

4.7 *In vitro* validation of peptide-conjugated DNA nanoparticles

We were also interested to evaluate the capacity of the DNA particles to serve as a platform for other types of antigens, such as peptides. We chose to utilize peptides recognized by 3-83 IgM-BCR-transgenic mice, which produce only a single B cell receptor with defined specificity for a series of peptides^{181–184}. The use of this system also allowed for decorating DNA particles with different peptides to determine how the affinity of the BCR for each peptide alters its activation. For these studies, we chose to investigate two of the peptides in this series: p31, with a K_D for binding to the 3-83 B cell receptor of 15.3 nM, and p5, with a K_D for binding to the 3-83 B cell receptor of 1 μ M. In addition to DNA particles bearing these peptides, control particles in the form of peptide-displaying liposomes were synthesized⁷⁹.

To obtain the cells needed for a calcium flux assay, a 3-83 transgenic mouse was euthanized and its spleen was excised. Single cells were isolated via mechanical disruption and run through a B cell isolation kit to enrich the population for B cells. These cells were then stained as the cultured eOD-specific cells had been and used for the assay. While overall signaling was significantly lower than what had been observed using cultured cells, clear signals were detectable for all the particles tested with differences in calcium flux kinetics between DNA particles displaying p5 and those displaying the higher affinity p31 (Figure 33). This result demonstrates not only that DNA particles can successfully display different types of antigens for B cell recognition, but also that primary B cells can be successfully used in plate-based calcium flux assays, potentially opening the door to a wider variety of study designs.

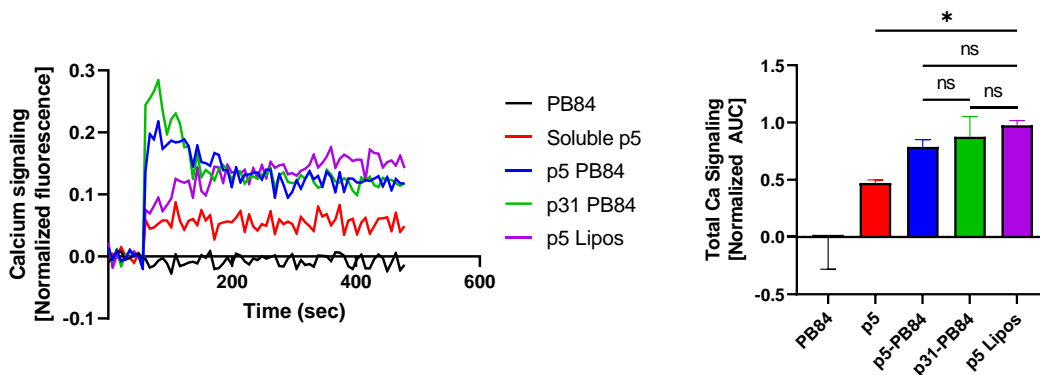


Figure 34. Primary B cell activation can be detected *in vitro* in presence of antigen-bearing nanoparticles. Primary 3-83 B cells were isolated from spleens and loaded with Fluo-4 calcium sensitive dye. p5- and p31-displaying nanoparticles were washed over the cells at a molar peptide equivalent concentration of 1 nM. Subsequent calcium flux was detected as increase in fluorescence from the cells and is shown as representative normalized fluorescence changes over time and average area-under-the-curve (AUC) of three independent repeats normalized to the maximum response among all samples in a repeat. Shown are averages and SEM. * $p < 0.05$; ns=not significant by one-way ANOVA followed by Tukey's multiple comparisons test.

4.8 Discussion

DNA origami is an extremely versatile tool that has the potential to be a powerful platform for evaluating how different design parameters effect nanoparticle immunogenicity. During the studies outlined in this chapter, we were able to begin elucidating the relative importance of a variety of factors, including nanoparticle geometry, antigen density, antigen spacing, and antigen conformational flexibility. These studies pave the way for additional work in this area and demonstrate the potential of a large, iteratively-produced DNA nanostructure library for the thorough understanding of how to best design nanoparticle antigens for maximal B cell activation.

These initial experiments have already produced some results that were perhaps unintuitive based on the predominant thinking in the field, primarily in the effect of antigen copy number on B cell activation. Our results suggest that beyond a certain threshold, increasing antigen copy number and antigen density on a nanoparticle surface does not result in increased B cell activation as determined by calcium flux. It is possible that this is because, at a certain

point, B cell receptors are already crosslinking as much as possible based on the size of the B cell receptors themselves, and therefore fitting more antigen in on the surface of a particle will not allow for further B cell receptor engagement. Since a maximal density does not seem to be required, this may allow for optimized nanoparticle designs that display both antigen at the necessary density and a separate homing ligand, such as a multibranched high mannose glycan, on the remaining free particle surface. This could allow for both efficient B cell activation and MBL recognition for particles to reach areas rich in B cells, potentially optimizing any humoral response against the antigen. This is merely one hypothetical example, and further research in this area is needed for more precise design criteria to be developed.

On an experimental design level, these studies highlight one of the first applications of calcium flux assays in a microwell plate format. These experiments are typically conducted on a flow cytometer, looking at the change in fluorescence of the population one cell at a time over the period of initial flux. The microwell format allows for significantly more rapid throughput and collects bulk fluorescence reads rather than individual cell reads, though some temporal resolution is sacrificed. For many applications, however, the microplate protocol developed for these experiments will be more practical and allow for more samples to be analyzed.

As made clear from our initial attempts at *in vivo* immunizations, additional optimization is required before these DNA nanostructures could be used effectively for studies in live animals. Whether this is because the particles are degraded rapidly upon injection, become trapped within the extracellular matrix, dehybridize in presence of serum, or some other mechanism remains to be seen. However, given the potential for these nanoparticles to answer fundamental and important questions in the field of nanoparticle vaccine design, more work is warranted to further improve this system for *in vivo* use.

4.9 Materials and Methods

Chemicals and kits

Magnesium chloride, TRIS acetate EDTA (TAE) buffer, TRIS-base, sodium chloride, Phosphate Buffer Saline, ethidium Bromide solution (10 mg/mL), Pluronic F-127 (#540025-50ML) and Amicon ultra 0.5 centrifugal filter (#UFC5003) were provided by Sigma-Aldrich. Nuclease free water was purchased from Integrated DNA Technologies, Inc. (IDT). The DNTPs mix (#N0447S), the DNA ladder (Quick-Load[®] Purple 2-Log DNA ladder 0.1-10 kb, #N0550S) were provided by New England Biolabs (NEB), The polymerase enzyme (Accustart Taq DNA polymerase HiFi, #95085-05K) was provided by Quanta Biosciences. Low melt agarose was purchased from IBI Scientific (#IB70058) and the agarose from Seakem, Inc. G-capsule for electroelution (#786-001) was purchased from G-Biosciences and Freeze 'N Squeeze DNA gel extraction columns by Bio-rad, Inc. (#732-6165). The Zymoclean Gel DNA recovery kit (#D4008) was purchased from Zymo Research, Inc. The SybrSafe DNA staining reagent was provided by Thermo Fisher Scientific, Inc. PEG3500 (#A4010-1/MAL-PEG3500-MAL) and PEG2000 (#A4010-1/MAL-PEG2000-MAL) bismaleimide were purchased from JenKem Technology.

Oligonucleotides and DNA templates

All oligonucleotides used for asymmetric PCR (aPCR) amplification of the template and for folding the various scaffolded DNA origami nanoparticles (NPs) were purchased from IDT. The circular plasmid DNA scaffold M13mp18 used for amplification of the short scaffolds with aPCR was acquired from NEB (#N4040S).

Antigens and cell lines

The eOD antigen with a 6xHis tag and N-terminal cysteine was prepared as previously described⁶⁷. Plasmids were transiently transfected into Expi293 cells (ThermoFisher Scientific, not authenticated). After 5 days, cell culture supernatants were collected and protein was purified in an ÄKTA pure chromatography system using HiTrap HP Ni sepharose affinity column, followed

by size exclusion chromatography using Superdex 75 Increase 10/300 GL column (GE Healthcare Life Sciences). Endotoxin levels in purified protein was measured using Endosafe Nexgen-PTS system (Charles River) and assured to be < 5EU/mg protein. PNA conjugated peptide antigens p31 (HDWRSGFGGFQHLCC-O-Linker-cagtccagt-K(AF-647)) and p5 (SGSVTYLPTPEWALQSGS-O-Linker-cagtccagt-K(AF-647)) were purchased from PNA Bio. Ramos B cells stably expressing VRC01 germline IgM B cell receptor were provided by Dr. Daniel Lingwood (Ragon Institute of MGH, MIT and Harvard)^{170,171}. As described previously, VRC01 germline cells were generated by stable lentiviral transduction of surface IgM-negative Ramos B cells and IgM-BCR-expressing cells were sorted by flow cytometry. Antigen-specific receptor expression levels after transduction were characterized previously and found to be ~12,000 per cell⁴⁴. Functional expression of germline VRC01 was confirmed by flow cytometry analysis of labeled eOD probes binding to the VRC01 Ramos cells. Both Expi293 and germline VRC01-expressing Ramos B cells tested negative for mycoplasma.

ssDNA scaffold synthesis

The ssDNA scaffolds used to fold the DNA six helix bundle (6-HB) and the DNA icosahedron NPs were produced using the previously described procedure asymmetric PCR^{185,186}. Briefly, two specific primers sets were used to amplify the ssDNA fragments using Quanta Accustart HiFi DNA polymerase. The aPCR mix was prepared at a final volume of 50 μ L with the specific polymerase buffer complemented with 2 mM magnesium chloride, 200 μ M dNTPs, 1 μ M forward primer, 20 nM reverse primer, 25 ng M13mp18 template, and 1 unit of Quanta Accustart HiFi polymerase. The amplification protocol used was: 94°C for 1 min for initial denaturation followed by 35 cycles of 94°C held for 20 sec; 56°C held for 30 sec; 68°C held for 1 min per kb for amplification. Following amplification, the aPCR mix was run on a 1% low-melt agarose gel prestained with Ethidium Bromide (EtBr). The resulting ssDNA product was then extracted using the Zymoclean gel DNA recovery kit. The custom circular DNA scaffold pHPB84

used for the pentagonal bipyramid DNA-NP was prepared as previously published¹⁶⁹. Purified ssDNA concentration was measured using a NanoDrop 2000 (Thermo Scientific).

DNA-NP folding

DNA-NPs (icosahedron, pentagonal bipyramid, and 6-HB) with or without overhangs were self-assembled using a one-pot reaction and annealing as described previously^{185,187}. Briefly, 20-40 nM of scaffold was mixed with an excess of the staple strand mix (molar ratio of 10x) in buffer TAE-MgCl₂ (40 mM Tris, 20 mM acetic acid, 2 mM EDTA, 16 mM MgCl₂, pH 8.0) in a final reaction volume of 50 uL and annealed with the following program: 95°C for 5 min, 80–75°C at 1°C per 5 min, 75–30°C at 1°C per 15 min, and 30–25°C at 1°C per 10 min. In the case of the pentagonal bipyramid, the reverse-complement oligonucleotide to the overhang sequence was added to the reaction mixture at 2-fold excess over the total concentration of the overhang sequence. The folded NPs are stored at 4°C in the folding buffer with the excess of staples strands prior to perform conjugation with antigens.

DNA-NP purification

Before using the DNA-NPs for conjugation with antigens and for the B cell activation assay, the DNA origami objects folded with an excess of staples strands were purified using an Amicon ultra 0.5 centrifugal filter with three washes of folding buffer and an extra wash of 1X PBS for further modification with antigens. In the case of the pentagonal bipyramid, DNA-NPs with overhangs were purified into TAE-MgCl₂ buffer prior to functionalization with antigen and concentrated to at least 5-fold over the target concentration for the functionalization reaction. Centrifugation steps were performed at 1000g for 30-40 minutes and the final concentration of NPs was determined using a NanoDrop 2000. Purified NPs were subsequently modified with antigens or stored in 1X PBS (or TAE-MgCl₂ buffer) at 4°C.

PNA strand synthesis

PNA strands were synthesized in-house using solid phase peptide synthesis. Lysine residues were attached at either end of the PNA sequence to improve solubility. Fmoc-PNA

monomers (PNA-Bio, Inc.) were coupled to a low loading Tentagel-S-RAM resin using 4 eq. PNA, 3.95 eq. PyBOP, and 6 eq. diisopropylethylamine (DIEA) in 2:1 DMF:DCM at room temperature for at least three hours. Lysine and glycine residues were reacted in the same way. Following each coupling, the peptide was deprotected in 20% piperidine in DMF. N-maleoyl- β -alanine (Sigma) was coupled to the N-terminus under the same coupling conditions. The peptide was then cleaved from the resin in 95% trifluoroacetic acid (TFA), 2.5% H₂O, and 2.5% triisopropylsilane. The peptide was dissolved in aqueous solution with 0.1% TFA, filtered, and purified by HPLC using a C-18 Gemini column (Phenomenex) with a mobile phase of acetonitrile containing 0.1% TFA. Purity of the PNA products was analyzed with MALDI-TOF mass spectrometry on a Bruker Daltonics microflex. The sequence of the synthesized PNA strand is: (Maleimide)-GGK-cagtccagt-K-(CONH₂), and the complementary ssDNA is: 5'-Oligo-TT-ACTGGACTG-3' (melting temperature predicted: 56.7°C). The sequence has been designed to have a melting temperature above 55°C (predicted with the PNA tool: https://www.pnabio.com/support/PNA_Tool.htm, from PNA Bio, Inc.) and orthogonal to the sequence of M13mp18 and validated using NCBI BLAST online tool.

Antigen-PNA conjugation

PNA strands were conjugated to eOD by reacting the terminal maleimide onto an N-terminal cysteine of eOD. Prior to the reaction, eOD was incubated with a 10-fold molar excess of tris(2-carboxyethyl)phosphine (TCEP) in PBS at room temperature for 15 minutes, after which TCEP was removed using a centrifugal filter. Immediately after removal of TCEP, a 2-fold molar excess of maleimide-PNA was reacted with cysteine-eOD overnight at 4°C in PBS. Unreacted PNA was then removed using an Amicon centrifugal filter (10 kDa MWCO).

Antigen attachment to DNA-NPs

Purified DNA-NPs were mixed with PNA-antigen conjugates at a molar ratio of 5X antigen per overhang on the DNA-NPs in 1X PBS buffer. The concentration of DNA-NPs used was in the

range of 50 to 100 nM. An annealing temperature ramp was used for ssPNA-ssDNA hybridization starting at 37°C and decreasing to 4°C at 1°C per 20 min and kept for at least 4 hours at 4°C prior use for B cell activation assay. Prior to use in the B cell activation assay, modified DNA-NPs were purified using a centrifugal filter, as described in the DNA-NP purification section above, to remove excess free PNA-antigens. Peptide antigens were added from DMF stock solutions and maximal target concentrations of DMF in the functionalization reaction were kept below 5% (v/v). For purification of the functionalized pentagonal bipyramid, centrifugal filters were coated with Pluronic F-127.

Transmission electron microscopy

DNA-NPs were visualized by transmission electron microscopy (TEM) using grids prepared as described previously with minor modifications⁴⁸. Briefly, carbon supported grids with copper mesh (CF200H-CU; Electron Microscopy Sciences) were glow discharged and soaked in 100 µM MgCl₂ and blotted prior to depositing DNA-NPs. 20 µl of a 10 nM DNA-NP solution was applied to a clean parafilm surface and the grid was floated for 2 minutes. While soaking, 2% uranyl formate (UF; Electron Microscopy Sciences) was neutralized with 25 mM NaOH final concentration, vortexed for 1 minute, and filtered via syringe through a 0.1 µm filter (EMD Millipore) dropwise onto the clean parafilm surface. The grid was then removed and quickly dried by edge blotting with Whatman 44 ashless paper. The grid was then immediately transferred to the 2% UF solution and incubated for 30 seconds. Again, the grid was dried by blotting along the edge with Whatman paper, and left to dry in air for an additional 30 minutes prior to imaging. Imaging was done on a FEI Tecnai G2 Spirit TWIN set to 120kV equipped with a Gatan camera. Images were acquired at 6,500x for wide-field views and 52,000x for near-field views. Images were collected using 3-second exposures. All raw images were cropped in Adobe Photoshop with subsequent autocontrast applied.

Agarose gel electrophoresis

DNA-NPs folded and conjugated with eOD-GT8-PNA were analyzed using agarose gel electrophoresis with 2% agarose gel pre-stained with EtBr. Samples non-purified in folding buffer or purified in PBS buffer were loaded at a concentration of 20 to 50 nM of DNA origami, ran for 2-3 hours at 70 V at 4C and visualized with a transilluminator. Images were subsequently merged using ImageJ software¹⁸⁸.

Tryptophan assay for quantification of DNA-NP coverage with antigen

A tryptophan fluorescence standard curve (0 to 2 μ M) was used to determine the percentage of antigen coverage on DNA-NPs. Tryptophan fluorescence was read on a fluorescence plate reader at 440 nm using an excitation wavelength of 370 nm.

B cell calcium flux assay

Ramos B Cells at a concentration of 10 million cells/mL were incubated with 10 μ M Fluo-4 AM (ThermoFisher, Inc.) for 30 minutes at 37C. After washing once, flux assays were performed on a Tecan plate reader at 37C on a 96 well microplate with 160 μ L of Fluo-4 labeled Ramos cells at 2 million cells/mL. A baseline fluorescence was then recorded for 1 minute, and 40 μ L of NPs were added to the cells for a final concentration of 5 nM of antigen, unless otherwise stated. A fixed concentration of antigens was used rather than the concentration of DNA-NPs to simplify the comparison between experiments with various DNA-NPs and to assess the role of antigen concentration instead of the role of the DNA-NPs. For studies utilizing the p31 and p5 peptide antigens, primary B cells were isolated from 3-83 mouse spleens and stained via the same procedure. Primary B cells were isolated from splenocytes by negative selection using a StemCell EasySep B Cell Isolation Kit.

B cell calcium flux data statistical analysis

Raw calcium traces were normalized to a common baseline by subtracting the PBS timetrace at every timepoint, then dividing the timetrace at every point by the average of the timepoints before antigen addition. The timepoints after antigen addition were then summed for

each sample in each repeat to give the calcium release above baseline (I_{tot}). The maximum I_{tot} across all samples within each repeat was determined ($\max(I_{tot})$), and total calcium signaling (normalized AUC) for each sample within each repeat is then given by $I_{tot} / \max(I_{tot})$. Repeats were then averaged together. Student's t-test was performed on the normalized AUCs entering into this average, where in most cases $n=3$ replicates.

Animals

Female 3-83 mice (H-2K^K-specific BCR) 6-10 weeks of age were used for primary B cell experiments. Mice were handled under local, state, and federal guidelines following an Institutional Animal Care and Use Committee (IACUC)-approved protocol at MIT.

p5 liposome synthesis

A lipid film was formed consisting of 1,2-dioleoyl-sn-glycero-3-phosphocholine (DOPC), 1,2-dimyristoyl-sn-glycero-3-phosphocholine (DMPC), 1,2-dioleoyl-sn-glycero-3-phospho-(1'-rac-glycerol) (DOPG), 1,2-distearoyl-sn-glycero-3-phosphoethanolamine-N-[maleimide(polyethylene glycol)-2000] (DSPE-mal), and synthetic monophosphoryl lipid A (MPLA) was formed in a DOPC : DMPC : DOPG : DSPE-mal : MPLA molar ratio of 37.8 : 37.8 : 18.9 : 5 : 0.5. The film was rehydrated in PBS with vortexing for one hour at 37 °C and was then taken through six freeze-thaw cycles using liquid nitrogen and room temperature water. Unilamellar liposomes were then formed via membrane extrusion using a 100 nm membrane.

Prior to the reaction, p5 was incubated with a 10-fold molar excess of tris(2-carboxyethyl)phosphine (TCEP) in PBS at room temperature for 15 minutes. A 2-fold molar excess of p5 compared to the DPSE-mal content of the liposomes was reacted with the liposomes for 2 hours in PBS at room temperature. Unconjugated p5 was removed by dialysis in PBS using 20 kDa MWCO dialysis cassettes. Bound p5 was assessed by tryptophan fluorescence.

5. Conclusion and future work

In this thesis, we have contributed data and understanding to two related but distinct areas. The first was the identification and investigation of a novel MBL- and complement-dependent trafficking mechanism that alters the lymph node accumulation of mannose-6-phosphate (M6P)-targeted nanoparticles, and the implications that this mechanism has on the design of future nanoparticle vaccines. The second was the development of DNA origami as a platform for probing key parameters of basic antigen-bearing nanoparticle design so that future particles can be built from the ground up in a rational manner for enhanced immunogenicity.

The findings described in this thesis and the related work of others in the field leave open numerous avenues for impactful future research. Some of these are direct continuations of the research that has been presented here, namely expanding on the types of nanoparticles and antigens tested for MBL recognition and more fully determining the extent to which mannose-6-phosphate (M6P) can positively impact the immunogenicity of nanoparticle antigens. Though a significant amount of that work has been accomplished and presented here, there are many more antigens that could have potential to be clinically useful as vaccine candidates if their immunogenicity could be increased than we could evaluate alone, so more work remains to further define how widely applicable mannose-6-phosphate (M6P) could be as a technique in these settings.

Taking a step back, the core of much of the work presented here focused on how interactions with the complement system and innate immunity as a whole can lead to beneficial changes to immune response generation. In particular, we've demonstrated how interactions with factors of innate immunity can beneficially influence antigen trafficking. While this area has been explored somewhat for other nanoparticle-based interventions, most nanoparticle trafficking research has focused on coating particles with monoclonal antibodies or large biomolecules that can be recognized by receptors found in the desired compartment for nanoparticle accumulation¹⁸⁹⁻¹⁹³. These strategies are not without merits, but the possibility of significantly

effecting trafficking without the need for large biomolecules on the surface of a nanoparticle opens much more design space for these particles, potentially allowing for specifically targeted nanoparticles that would otherwise have been difficult to create. Utilizing existing pathways of innate and active immunity could provide a path forward to a wide array of targeted nanoparticles for intervention in a variety of clinical settings.

One caveat to this approach that is important to consider is that these strategies may be more sensitive to differences in the biology of different individuals, particularly if efforts are made to translate them to clinical products. As a pertinent example, MBL levels can vary widely across individuals, and MBL deficiencies are not uncommon^{194–197}. These facts could mean that between different patients, different degrees of trafficking are observed when immunized with mannosylated nanoparticles. However, this is not something that is currently well understood, and more research in this area is warranted to better determine how natural variations in the expression of factors of innate immunity could impact the efficacy of nanoparticle vaccines designed to interact with them.

In summary, we have developed several techniques for improving and investigating the efficacy of nanoparticle vaccines, with broad applicability across the fields of both vaccinology and nanomedicine.

Appendix

eOD-GT8 amino acid sequence

CHHHHHGGDTITLPCRPAAPPHCSSNITGLILTRQGGYSNDNTVIFRPSGGDWRDIAR
CQIAGTVVSTQLFLNGSLAEEEVVIRSEDWRDNAKSICVQLNTSVEINCTGAGHCNISRA
KWNNTLKQIASKLREQYGNKTIIFKPSSGGDPEFVNHSFNCGGEFFYCDSTQLFNSTW
FNSTGS

Amino acid sequence for eOD-GT8-PADRE used in studies described in Chapters 2. The N-terminal cysteine is shown in blue, the histidine tag is shown in green, and the eOD antigen is shown in black.

eOD-60mer amino acid sequence

MQIYEGKLTAEGLRFGIVASRANHALVDRLVEGAIDAIVRHGGREEDITLVRVCGSWEIP
VAAGELARKEDIDAVIAIGVLCRGATPSFDYIASEVSKGLADLSLELRKPITFGVITADTLE
QAIEAAGTCHGNKGWEAALCAIEMANLFKSLRGGSGGSGGSGGSGGGDTITLPCRPA
PPPHCSSNITGLILTRQGGYSNDNTVIFRPSGGDWRDIARCQIAGTVVSTQLFLNGSLA
EEEVVIRSEDWRDNAKSICVQLNTSVEINCTGAGHCNISRAKWNNTLKQIASKLREQYG
NKTIIIFKPSSGGDPEFVNHSFNCGGEFFYCDSTQLFNSTWFNST

Amino acid sequence for eOD-60mer used in studied throughout this thesis. The lumazine synthase core including spacer is shown in red and the eOD antigen is shown in black.

eOD-GT8-PADRE amino acid sequence

CHHHHHGGDTITLPCRPPPPHCSSNITGLILTRQGGYSNDNTVIFRPSGGDWRDIAR
CQIAGTVVSTQLFLNGSLAEEVVIRSEDWRDNAKSICVQLNTSVEINCTGAGHCNISRA
KWNNTLKQIASKLREQYGNKTIIFKPSSGGDPEFVNHSFNCGGEFFYCDSTQLFNSTW
FNSTGS**AKFVAAWTLKAAA**

Amino acid sequence for eOD-GT8-PADRE used in studies described in Chapters 3 and 4. The N-terminal cysteine is shown in blue, the histidine tag is shown in green, the eOD antigen is shown in black, and the PADRE epitope is shown in red.

p5 amino acid sequence

SGSVTYLPTPEWALQSGSC

Amino acid sequence for the p5 peptide, with an additional C-terminal cysteine added for conjugation chemistry.

p31 amino acid sequence

SGSHDWRSFGGGFQHLCCSGS

Amino acid sequence of the p31 peptide.

Lymph node solvent-based clearing protocol

Materials: tocopherol (toco); 24-well plates with lids; 20 ml glass scintillation vials; aluminum foil; power towels; forceps

Solvents: PBS; 4% paraformaldehyde (PFA); methanol (MeOH); tertiary butanol (t-but); dichloromethane (DCM); dibenzyl ether (DBE); dimethyl sulfoxide (DMSO); hydrogen peroxide (H₂O₂)

Solutions to prepare in bulk:

- 50% PBS + 50% MeOH
- 20% PBS + 80% MeOH
- “Bleach”: MeOH:DMSO:H₂O₂ in a 4:1:1 ratio (prepare immediately before use)
- 49.8% MeOH + 49.8% t-but + 0.4% toco
- 19.8% MeOH + 79.8% t-but + 0.4% toco
- 99.6% t-but + 0.4% toco
- 99.6% DCM + 0.4% toco

Notes:

- At every step, cover lymph nodes in foil to prevent fluorescent signal loss.
 - From step 4 on, all steps should be completed in a chemical fume hood.
1. One day prior to extracting lymph nodes, inject 4 ug BV421 anti-CD35 subcutaneously at tail base to allow for follicle visualization.
 2. Extract lymph nodes, being careful to avoid puncturing or tearing them while also removing as much connective tissue as possible, and fix in 1 ml 4% PFA overnight at 4° C in a 24-well plate. Nodes from the same animal may be kept in the same wells.
 3. Remove PFA and wash lymph nodes twice in 1 ml PBS at room temperature for 30 minutes each. During these washes, gently remove any remaining connective tissue.

4. Remove PBS and soak lymph nodes in 1 ml 50% PBS + 50% MeOH for 30 minutes.
5. Remove 50% PBS + 50% MeOH and soak lymph nodes in 1 ml 20% PBS + 80% MeOH for 30 minutes.
6. Remove 20% PBS + 80% MeOH and soak lymph nodes in 1 ml MeOH. Prepare 3 ml bleach solution in two scintillation vials (6 ml total).
7. One well at a time, transfer lymph nodes to a vial of bleach solution, soak for one minute, and return to MeOH for 30 minutes.
 - a. Be consistent with soak time in bleach across all lymph nodes. Nodes should be noticeably whiter after bleaching.
 - b. Can stagger samples by 30 seconds to use both bleach vials.
 - c. Begin warming 99.6% t-but + 0.4% toco in 37° C water bath.
8. Remove MeOH and soak lymph nodes in 1 ml 49.8% MeOH + 49.8% t-but + 0.4% toco for 30 minutes.
9. Remove 49.8% MeOH + 49.8% t-but + 0.4% toco and soak lymph nodes in 1 ml 19.8% MeOH + 79.8% t-but + 0.4% toco for 30 minutes.
10. Remove 19.8% MeOH + 79.8% t-but + 0.4% toco and soak lymph nodes in 1 ml 99.6% t-but + 0.4% toco at 37° C for one hour.
11. Tape down a paper towel inside a chemical fume hood and mark off zones for each well. Transfer lymph nodes into the appropriate zone of the paper towel and wait for them to dry.
 - a. The lymph nodes at this stage tend to “jump”: use forceps cautiously to place them on paper towel.
 - b. Leaving the fume hood open during this stage, as closing it will result in nodes being sucked into the back of the hood.

12. Transfer lymph nodes to glass scintillation vials containing 5 ml 99.6% DCM + 0.4% toco. Periodically swirl the vials. Once the lymph nodes sink to the bottom of the vials after swirling, immediately transfer them to scintillation vials containing 99.6% DBE + 0.4% toco.
 - a. It typically takes about 3-6 minutes of soaking before lymph nodes will sink after swirling.
13. Allow lymph nodes to clear in DBE solution for at least one day before imaging on a confocal microscope.

Biolayer interferometry protocol

Materials: two 96-well black plates; PBS + 1% BSA (+ 0.05 mg/ml calcium if using MBL in assay); biotinylation kit; streptavidin-coated octet biosensors (provided by BIF at MIT)

Notes:

- For accurate reads, typically at least four dilutions of each sample are required. There are also two needed controls for each sample, so this protocol assumes six dilutions to fill out one column of a 96-well plate.
- The concentration range to use is dependent on the binding being analyzed and may require optimization. For eOD-60mer binding to immobilized MBL, a maximum concentration of 5-10 ug/ml eOD is typically a good starting point. For IgG purified from serum of immunized mice binding to the immunogen, 1-5 uM is a good starting point.

Plate set up

1. Biotinylate protein (typically MBL for MBL-binding assays or antigen for antigen-specific IgG analysis) according to kit instructions and purify unbound biotin by centrifugation.
 - a. Aim for 1-2 biotin/protein, as too much can interfere with binding to analyte.
2. Prepare biosensor plate
 - a. Add 200 ul of PBS/BSA buffer to every well of a column, then repeat in other columns until one column is filled for each sample.
3. Prepare sample plate
 - a. Fill column one with 200 ul buffer
 - b. Fill column two with 200 ul buffer containing 3-5 ug/ml biotinylated protein
 - i. In well G2, add 200 ul buffer only (no biotinylated protein)
 - ii. The exact concentration is not very important as the length of the loading step can be adjusted during the assay.

c. Sample dilution columns

- i. For each sample, add 300 ul sample in PBS/BSA to the first well of the column.
- ii. Add 200 ul PBS/BSA to wells B-F and H in each sample column.
- iii. Transfer 100 ul of each well A to the corresponding well B, mix, and repeat this process through row F, discarding the excess 100 ul.
- iv. Add 200 ul sample in PBS/BSA at a concentration between that of rows A or B in well G.

Octet assay

1. Place biosensor 96-well plate in biosensor tray and add biosensors to each buffer-containing well.
 - a. Be careful not to scrape biosensors on the wall of the wells while inserting them. Do not use biosensors that have scraped the sides.
 - b. Ensure that biosensors have been in buffer for at least five minutes before beginning assay.
2. Place sample plate in octet in position on heating pad.
3. Set up kinetics experiment protocol in octet software
 - a. Steps:
 - i. Move column of biosensors to sample plate column 1 for 120 seconds
 - ii. Move biosensors to column 2
 1. The exact time of this step depends on the protein concentration and degree of biotinylation. The step should be ended once the increase in signal begins to become nonlinear.
 - iii. Move biosensors to column 1 for 180 seconds.
 - iv. Move biosensors to sample column.

1. The length of time required will vary based on the binding kinetics and should be allowed to run until saturation is observed in the maximal concentration. Allowing 300-600 seconds for this step is usually sufficient.
 - v. Move biosensors to column 1 for 300-600 seconds or until significant dissociation (at least a 10% reduction in binding) is observed.
 - vi. Repeat this protocol for each sample to be analyzed.
- b. Note: because very little protein actually dissociates into column 1 after each run, column 1 can be continued to be used as a wash and dissociation buffer throughout the experiment.
- c. Set the temperature to 30° C.
4. When analyzing data, subtract control curves in rows G and H from other samples.
 - a. Good fits will visually match the data curves well, have $R^2 > 0.95$ and $\chi^2 < 3$.
 - b. MBL binding will not normally have good fits because the models assume a 1:1 or 1:2 binding interaction.
 - c. Fits of purified IgG binding will give apparent values that are aggregates for the sample as a whole.

Calcium flux assay protocol

Materials: 96-well black plate; serum-free RPMI; Fluo4-AM cell permeant (ThermoFisher F14201)*; ionomycin; antigen-specific B cells (Ramos VRC01 B cells for eOD)

Note: due to variation between assay runs, samples should always be run in triplicate.

1. Centrifuge cells at 1600 RPM for 5 minutes, aspirate supernatant, resuspend in 1 ml RPMI, and count. Adjust cell concentration to 20 million/ml.
2. Prepare Fluo4 by resuspending a new tube in 45.8 ul DMSO to create a 1 mM stock.
 - a. Leftover resuspended Fluo4 can be stored at -20° C.
3. Add 20 ul Fluo4 to 730 ul RPMI, then add 750 ul of cells. Parafilm and incubate for 30 minutes at 37° C.
 - a. The number of cells to be stained can be adjusted to accommodate the number of samples to be tested. Adjust the Fluo4 and total volumes accordingly.
 - b. After staining, the cells will be sensitive to temperature. Keep them at room temperature at the coldest and run assays as soon as possible.
4. During staining, prepare sample dilutions.
 - a. For each run of the assay, 40 ul of sample at 5x the desired assay concentration are required.
 - b. Typical assay concentrations are in the range of 0.5-10 nM.
5. Wash cells twice in RPMI.
6. Add 160 ul cells at 2 million/ml to each well of black 96-well plate to be used for assay.
 - a. Include wells for RPMI only negative control and ionomycin assay control.
 - b. Place replicates in different rows, with no more than 8 or 9 total samples per row (more will reduce temporal resolution).
7. Insert plate into plate reader preset to 37° C and wait for five minutes for plate to warm up.

- a. During warming, set up plate reader for continuous fluorescence read at 480 excitation and 520 emission with light shaking.
8. Run fluorescence baseline of first row for one minute. Quickly add samples using a multichannel pipette, avoiding bubbles. Immediately run on plate reader again for at least five minutes.
9. Repeat step 8 for all other rows.

*This version of Fluo-4 is not compatible with serum, as confirmed by studies using media containing 2% mouse serum. If using serum-containing media, use Fluo-4 Direct (ThermoFisher F10471) and follow the manufacturer's instructions for running the assay with non-adherent cells, adding ~300,000 cells per well.

References

1. Nabel, G. J. Designing Tomorrow's Vaccines. *New Engl J Medicine* **368**, 551–560 (2013).
2. Robbins, F. C. Poliomyelitis Eradication: a Continuing Story. *Faseb J* **8**, 665–666 (1994).
3. Wolfson, L. J. *et al.* Has the 2005 measles mortality reduction goal been achieved? A natural history modelling study. *Lancet* **369**, 191–200 (2007).
4. Barquet, N. & Domingo, P. Smallpox: The Triumph over the Most Terrible of the Ministers of Death. *Ann Intern Med* **127**, 635 (1997).
5. Roush, S. W., Murphy, T. V. & Group, and the V.-P. D. T. W. Historical Comparisons of Morbidity and Mortality for Vaccine-Preventable Diseases in the United States. *Jama* **298**, 2155–2163 (2007).
6. Allen, C. D. C., Okada, T. & Cyster, J. G. Germinal-Center Organization and Cellular Dynamics. *Immunity* **27**, 190–202 (2007).
7. Victora, G. D. & Nussenzweig, M. C. Germinal Centers. *Immunology* **30**, 429–457 (2012).
8. Zhang, Y., Garcia-Ibanez, L. & Toellner, K. Regulation of germinal center B-cell differentiation. *Immunol Rev* **270**, 8–19 (2016).
9. Huang, C. B Cells in Immunity and Tolerance. *Adv Exp Med Biol* **1254**, 47–53 (2020).
10. Pollard, A. J. & Bijker, E. M. A guide to vaccinology: from basic principles to new developments. *Nat Rev Immunol* **21**, 83–100 (2021).
11. Baden, L. R. *et al.* Efficacy and Safety of the mRNA-1273 SARS-CoV-2 Vaccine. *New Engl J Med* **384**, 403–416 (2020).
12. Haque, A., Akçeşme, F. B. & Pant, A. B. A systematic review of Zika virus: hurdles toward vaccine development and the way forward. *Antivir Ther* **23**, 285–293 (2017).
13. Rezza, G. & Weaver, S. C. Chikungunya as a paradigm for emerging viral diseases: Evaluating disease impact and hurdles to vaccine development. *Plos Neglect Trop D* **13**, e0006919 (2019).
14. Garvy, B. A. Overcoming Hurdles to Development of a Vaccine against *Pneumocystis jirovecii*. *Infect Immun* **85**, e00035-17 (2017).
15. Oyston, P. & Robinson, K. The current challenges for vaccine development. *J Med Microbiol* **61**, 889–894 (2012).
16. Valkenburg, S. A. *et al.* The Hurdles From Bench to Bedside in the Realization and Implementation of a Universal Influenza Vaccine. *Front Immunol* **9**, 1479 (2018).

17. Eisinger, R. W. & Fauci, A. S. Ending the HIV/AIDS Pandemic - Volume 24, Number 3—March 2018 - Emerging Infectious Diseases journal - CDC. *Emerg Infect Dis* **24**, 413–416 (2018).
18. Simon, V., Ho, D. D. & Karim, Q. A. HIV/AIDS epidemiology, pathogenesis, prevention, and treatment. *Lancet* **368**, 489–504 (2006).
19. Fauci, A. S. An HIV Vaccine is Essential for Ending the HIV/AIDS Pandemic. *Jama* **318**, 1535 (2017).
20. Sadanand, S., Suscovich, T. J. & Alter, G. Broadly Neutralizing Antibodies Against HIV: New Insights to Inform Vaccine Design. *Annu Rev Med* **67**, 1–16 (2015).
21. Burton, D. R. & Hangartner, L. Broadly Neutralizing Antibodies to HIV and Their Role in Vaccine Design. *Annu Rev Immunol* **34**, 635–659 (2016).
22. Bbosa, N., Kaleebu, P. & Ssemwanga, D. HIV subtype diversity worldwide. *Curr Opin HIV Aids* **14**, 153–160 (2019).
23. Burton, D. R., Poignard, P., Stanfield, R. L. & Wilson, I. A. Broadly Neutralizing Antibodies Present New Prospects to Counter Highly Antigenically Diverse Viruses. *Science* **337**, 183–186 (2012).
24. Corti, D. & Lanzavecchia, A. Broadly Neutralizing Antiviral Antibodies. *Immunology* **31**, 705–742 (2013).
25. Pitisuttithum, P. *et al.* Randomized, Double-Blind, Placebo-Controlled Efficacy Trial of a Bivalent Recombinant Glycoprotein 120 HIV-1 Vaccine among Injection Drug Users in Bangkok, Thailand. *J Infect Dis* **194**, 1661–1671 (2006).
26. Flynn, N. M. *et al.* Placebo-Controlled Phase 3 Trial of a Recombinant Glycoprotein 120 Vaccine to Prevent HIV-1 Infection. *J Infect Dis* **191**, 654–665 (2005).
27. Myszka, D. G. *et al.* Energetics of the HIV gp120-CD4 binding reaction. *Proc National Acad Sci* **97**, 9026–9031 (2000).
28. Chen, L. *et al.* Structural Basis of Immune Evasion at the Site of CD4 Attachment on HIV-1 gp120. *Science* **326**, 1123–1127 (2009).
29. Kwong, P. D. *et al.* HIV-1 evades antibody-mediated neutralization through conformational masking of receptor-binding sites. *Nature* **420**, 678–682 (2002).
30. Hammonds, J. *et al.* Gp120 stability on HIV-1 virions and Gag-Env pseudovirions is enhanced by an uncleaved Gag core. *Virology* **314**, 636–649 (2003).
31. Liao, H.-X. *et al.* Co-evolution of a broadly neutralizing HIV-1 antibody and founder virus. *Nature* **496**, 469–476 (2013).
32. Horiya, S., MacPherson, I. S. & Krauss, I. J. Recent strategies targeting HIV glycans in vaccine design. *Nat Chem Biol* **10**, 990–999 (2014).

33. Icenogle, J. *et al.* Neutralization of poliovirus by a monoclonal antibody: Kinetics and stoichiometry. *Virology* **127**, 412–425 (1983).
34. Schofield, D. J., Stephenson, J. R. & Dimmock, N. J. Variations in the neutralizing and haemagglutination-inhibiting activities of five influenza A virus-specific IgGs and their antibody fragments. *J Gen Virol* **78**, 2431–2439 (1997).
35. Galimidi, R. P. *et al.* Intra-Spike Crosslinking Overcomes Antibody Evasion by HIV-1. *Cell* **160**, 433–446 (2015).
36. Trovato, M., Sartorius, R., D’Apice, L., Manco, R. & Berardinis, P. D. Viral Emerging Diseases: Challenges in Developing Vaccination Strategies. *Front Immunol* **11**, 2130 (2020).
37. Chiu, C. Seasonal influenza vaccines and hurdles to mutual protection. *Clin Microbiol Infec* **22**, S113–S119 (2016).
38. Hu, J. K. *et al.* Murine Antibody Responses to Cleaved Soluble HIV-1 Envelope Trimers Are Highly Restricted in Specificity. *J Virol* **89**, 10383–10398 (2015).
39. Klinman, D. M., Higgins, K. W. & Conover, J. Sequential immunizations with rgp120s from independent isolates of human immunodeficiency virus type 1 induce the preferential expansion of broadly crossreactive B cells. *J Exp Medicine* **173**, 881–887 (1991).
40. Mörner, A. *et al.* Human Immunodeficiency Virus Type 1 Env Trimer Immunization of Macaques and Impact of Priming with Viral Vector or Stabilized Core Protein ∇ \dagger . *J Virol* **83**, 540–551 (2008).
41. Guenaga, J. *et al.* Heterologous Epitope-Scaffold Prime:Boosting Immuno-Focuses B Cell Responses to the HIV-1 gp41 2F5 Neutralization Determinant. *Plos One* **6**, e16074 (2011).
42. Escolano, A., Dosenovic, P. & Nussenzweig, M. C. Progress toward active or passive HIV-1 vaccination. *J Exp Medicine* **214**, 3–16 (2017).
43. Scheid, J. F. *et al.* Broad diversity of neutralizing antibodies isolated from memory B cells in HIV-infected individuals. *Nature* **458**, 636–640 (2009).
44. Dimitrov, D. S. Therapeutic antibodies, vaccines and antibodyomes. *Mabs* **2**, 347–356 (2010).
45. Pancera, M. *et al.* Crystal Structure of PG16 and Chimeric Dissection with Somatic Related PG9: Structure-Function Analysis of Two Quaternary-Specific Antibodies That Effectively Neutralize HIV-1 ∇ \dagger . *J Virol* **84**, 8098–8110 (2010).
46. Zhou, T. *et al.* Structural Basis for Broad and Potent Neutralization of HIV-1 by Antibody VRC01. *Science* **329**, 811–817 (2010).
47. Haynes, B. F., Kelsoe, G., Harrison, S. C. & Kepler, T. B. B-cell-lineage immunogen design in vaccine development with HIV-1 as a case study. *Nat Biotechnol* **30**, 423–433 (2012).
48. Mouquet, H. *et al.* Complex-type N-glycan recognition by potent broadly neutralizing HIV antibodies. *Proc National Acad Sci* **109**, E3268–E3277 (2012).

49. Xiao, X. *et al.* Germline-like predecessors of broadly neutralizing antibodies lack measurable binding to HIV-1 envelope glycoproteins: Implications for evasion of immune responses and design of vaccine immunogens. *Biochem Biophys Res Commun* **390**, 404–409 (2009).
50. Jardine, J. *et al.* Rational HIV Immunogen Design to Target Specific Germline B Cell Receptors. *Science* **340**, 711–716 (2013).
51. Jardine, J. G. *et al.* Priming a broadly neutralizing antibody response to HIV-1 using a germline-targeting immunogen. *Science* **349**, 156–161 (2015).
52. McGuire, A. T. *et al.* Engineering HIV envelope protein to activate germline B cell receptors of broadly neutralizing anti-CD4 binding site antibodies Restoring germline anti-HIV antibody binding. *J Exp Medicine* **210**, 655–663 (2013).
53. Dosenovic, P. *et al.* Immunization for HIV-1 Broadly Neutralizing Antibodies in Human Ig Knockin Mice. *Cell* **161**, 1505–1515 (2015).
54. McGuire, A. T. *et al.* Antigen modification regulates competition of broad and narrow neutralizing HIV antibodies. *Science* **346**, 1380–1383 (2014).
55. Sanders, R. W. *et al.* Stabilization of the Soluble, Cleaved, Trimeric Form of the Envelope Glycoprotein Complex of Human Immunodeficiency Virus Type 1. *J Virol* **76**, 8875–8889 (2002).
56. Harris, A. *et al.* Trimeric HIV-1 glycoprotein gp140 immunogens and native HIV-1 envelope glycoproteins display the same closed and open quaternary molecular architectures. *Proc National Acad Sci* **108**, 11440–11445 (2011).
57. Beddows, S. *et al.* Evaluating the Immunogenicity of a Disulfide-Stabilized, Cleaved, Trimeric Form of the Envelope Glycoprotein Complex of Human Immunodeficiency Virus Type 1. *J Virol* **79**, 8812–8827 (2005).
58. Sanders, R. W. *et al.* A Next-Generation Cleaved, Soluble HIV-1 Env Trimer, BG505 SOSIP.664 gp140, Expresses Multiple Epitopes for Broadly Neutralizing but Not Non-Neutralizing Antibodies. *PLoS Pathog* **9**, e1003618 (2013).
59. Kulp, D. W. *et al.* Structure-based design of native-like HIV-1 envelope trimers to silence non-neutralizing epitopes and eliminate CD4 binding. *Nat Commun* **8**, 1655 (2017).
60. Steichen, J. M. *et al.* HIV Vaccine Design to Target Germline Precursors of Glycan-Dependent Broadly Neutralizing Antibodies. *Immunity* **45**, 483–496 (2016).
61. Lin, W.-H. W., Kouyos, R. D., Adams, R. J., Grenfell, B. T. & Griffin, D. E. Prolonged persistence of measles virus RNA is characteristic of primary infection dynamics. *Proc National Acad Sci* **109**, 14989–14994 (2012).
62. Simon, I. D., Publicover, J. & Rose, J. K. Replication and Propagation of Attenuated Vesicular Stomatitis Virus Vectors In Vivo: Vector Spread Correlates with Induction of Immune Responses and Persistence of Genomic RNA. *J Virol* **81**, 2078–2082 (2006).

63. Luker, K. E., Hutchens, M., Schultz, T., Pekosz, A. & Luker, G. D. Bioluminescence imaging of vaccinia virus: Effects of interferon on viral replication and spread. *Virology* **341**, 284–300 (2005).
64. Kuraoka, M. *et al.* Complex Antigens Drive Permissive Clonal Selection in Germinal Centers. *Immunity* **44**, 542–552 (2016).
65. Cirelli, K. M. *et al.* Slow Delivery Immunization Enhances HIV Neutralizing Antibody and Germinal Center Responses via Modulation of Immunodominance. *Cell* **180**, 206 (2020).
66. Tam, H. H. *et al.* Sustained antigen availability during germinal center initiation enhances antibody responses to vaccination. *Proc National Acad Sci* **113**, E6639–E6648 (2016).
67. Jardine, J. G. *et al.* HIV-1 broadly neutralizing antibody precursor B cells revealed by germline-targeting immunogen. *Science* **351**, 1458–1463 (2016).
68. Sok, D. *et al.* Priming HIV-1 broadly neutralizing antibody precursors in human Ig loci transgenic mice. *Science* **353**, 1557–1560 (2016).
69. Sliepen, K. *et al.* Presenting native-like HIV-1 envelope trimers on ferritin nanoparticles improves their immunogenicity. *Retrovirology* **12**, 82 (2015).
70. He, L. *et al.* Presenting native-like trimeric HIV-1 antigens with self-assembling nanoparticles. *Nat Commun* **7**, 12041 (2016).
71. Moyer, T. J., Zmolek, A. C. & Irvine, D. J. Beyond antigens and adjuvants: formulating future vaccines. *J Clin Invest* **126**, 799–808 (2016).
72. Cyster, J. G. B cell follicles and antigen encounters of the third kind. *Nat Immunol* **11**, 989–996 (2010).
73. Tyler, M., Tumban, E., Peabody, D. S. & Chackerian, B. The use of hybrid virus-like particles to enhance the immunogenicity of a broadly protective HPV vaccine. *Biotechnol Bioeng* **111**, 2398–2406 (2014).
74. Francica, J. R. *et al.* Star nanoparticles delivering HIV-1 peptide minimal immunogens elicit near-native envelope antibody responses in nonhuman primates. *Plos Biol* **17**, e3000328 (2019).
75. Bai, L. *et al.* Natural killer T (NKT)–B-cell interactions promote prolonged antibody responses and long-term memory to pneumococcal capsular polysaccharides. *Proc National Acad Sci* **110**, 16097–16102 (2013).
76. Vetro, M. *et al.* Preparation and immunogenicity of gold glyco-nanoparticles as antipneumococcal vaccine model. *Nanomedicine-uk* **12**, 13–23 (2017).
77. Karch, C. P. *et al.* Design and characterization of a self-assembling protein nanoparticle displaying HIV-1 Env V1V2 loop in a native-like trimeric conformation as vaccine antigen. *Nanomed Nanotechnol Biology Medicine* **16**, 206–216 (2018).

78. Brouwer, P. J. M. *et al.* Enhancing and shaping the immunogenicity of native-like HIV-1 envelope trimers with a two-component protein nanoparticle. *Nat Commun* **10**, 4272 (2019).
79. Tokatlian, T. *et al.* Enhancing Humoral Responses Against HIV Envelope Trimers via Nanoparticle Delivery with Stabilized Synthetic Liposomes. *Sci Rep-uk* **8**, 16527 (2018).
80. Frauenfeld, J. *et al.* A saposin-lipoprotein nanoparticle system for membrane proteins. *Nat Methods* **13**, 345–351 (2016).
81. Gerritzen, M. J. H., Martens, D. E., Wijffels, R. H., Pol, L. van der & Stork, M. Bioengineering bacterial outer membrane vesicles as vaccine platform. *Biotechnol Adv* **35**, 565–574 (2017).
82. Marcandalli, J. *et al.* Induction of Potent Neutralizing Antibody Responses by a Designed Protein Nanoparticle Vaccine for Respiratory Syncytial Virus. *Cell* **176**, 1420-1431.e17 (2019).
83. Ingale, J. *et al.* High-Density Array of Well-Ordered HIV-1 Spikes on Synthetic Liposomal Nanoparticles Efficiently Activate B Cells. *Cell Reports* **15**, 1986–1999 (2016).
84. Thompson, E. A. *et al.* TLR-adjuvanted nanoparticle vaccines differentially influence the quality and longevity of responses to malaria antigen Pfs25. *Jci Insight* **3**, e120692 (2018).
85. Havenar-Daughton, C. *et al.* Rapid Germinal Center and Antibody Responses in Non-human Primates after a Single Nanoparticle Vaccine Immunization. *Cell Reports* **29**, 1756-1766.e8 (2019).
86. Kanekiyo, M. *et al.* Mosaic nanoparticle display of diverse influenza virus hemagglutinins elicits broad B cell responses. *Nat Immunol* **20**, 362–372 (2019).
87. Dubrovskaya, V. *et al.* Vaccination with Glycan-Modified HIV NFL Envelope Trimer-Liposomes Elicits Broadly Neutralizing Antibodies to Multiple Sites of Vulnerability. *Immunity* **51**, 915-929.e7 (2019).
88. Shukla, G. S., Sun, Y.-J., Pero, S. C., Sholler, G. S. & Krag, D. N. Immunization with tumor neoantigens displayed on T7 phage nanoparticles elicits plasma antibody and vaccine-draining lymph node B cell responses. *J Immunol Methods* **460**, 51–62 (2018).
89. Sliepen, K. *et al.* Structure and immunogenicity of a stabilized HIV-1 envelope trimer based on a group-M consensus sequence. *Nat Commun* **10**, 2355 (2019).
90. Tokatlian, T. *et al.* Innate immune recognition of glycans targets HIV nanoparticle immunogens to germinal centers. *Science* **363**, eaat9120 (2018).
91. Chang, T. Z., Stadmiller, S. S., Staskevicius, E. & Champion, J. A. Effects of ovalbumin protein nanoparticle vaccine size and coating on dendritic cell processing. *Biomater Sci-uk* **5**, 223–233 (2016).
92. Bachmann, M. F. & Jennings, G. T. Vaccine delivery: a matter of size, geometry, kinetics and molecular patterns. *Nat Rev Immunol* **10**, 787–796 (2010).
93. Naud, P. S. *et al.* Sustained efficacy, immunogenicity, and safety of the HPV-16/18 AS04-adjuvanted vaccine. *Hum Vacc Immunother* **10**, 2147–2162 (2014).

94. Jackson, Y., Chappuis, F., Mezger, N., Kanappa, K. & Loutan, L. High immunogenicity of delayed third dose of hepatitis B vaccine in travellers. *Vaccine* **25**, 3482–3484 (2007).
95. Kanekiyo, M. *et al.* Self-assembling influenza nanoparticle vaccines elicit broadly neutralizing H1N1 antibodies. *Nature* **499**, 102–106 (2013).
96. Kanekiyo, M. *et al.* Rational Design of an Epstein-Barr Virus Vaccine Targeting the Receptor-Binding Site. *Cell* **162**, 1090–1100 (2015).
97. Abbott, R. K. *et al.* Precursor Frequency and Affinity Determine B Cell Competitive Fitness in Germinal Centers, Tested with Germline-Targeting HIV Vaccine Immunogens. *Immunity* **48**, 133-146.e6 (2018).
98. Bale, S. *et al.* Covalent Linkage of HIV-1 Trimers to Synthetic Liposomes Elicits Improved B Cell and Antibody Responses. *J Virol* **91**, e00443-17 (2017).
99. Martinez-Murillo, P. *et al.* Particulate Array of Well-Ordered HIV Clade C Env Trimers Elicits Neutralizing Antibodies that Display a Unique V2 Cap Approach. *Immunity* **46**, 804-817.e7 (2017).
100. Park, C., Arthos, J., Cicala, C. & Kehrl, J. H. The HIV-1 envelope protein gp120 is captured and displayed for B cell recognition by SIGN-R1+ lymph node macrophages. *Elife* **4**, e06467 (2015).
101. Manolova, V. *et al.* Nanoparticles target distinct dendritic cell populations according to their size. *Eur J Immunol* **38**, 1404–1413 (2008).
102. Moon, J. J. *et al.* Enhancing humoral responses to a malaria antigen with nanoparticle vaccines that expand Tfh cells and promote germinal center induction. *Proc National Acad Sci* **109**, 1080–1085 (2012).
103. Reddy, S. T., Rehor, A., Schmoekel, H. G., Hubbell, J. A. & Swartz, M. A. In vivo targeting of dendritic cells in lymph nodes with poly(propylene sulfide) nanoparticles. *J Control Release* **112**, 26–34 (2006).
104. Shukla, S. *et al.* Plant viral nanoparticles-based HER2 vaccine: Immune response influenced by differential transport, localization and cellular interactions of particulate carriers. *Biomaterials* **121**, 15–27 (2017).
105. Phan, T. G., Grigorova, I., Okada, T. & Cyster, J. G. Subcapsular encounter and complement-dependent transport of immune complexes by lymph node B cells. *Nat Immunol* **8**, 992–1000 (2007).
106. Phan, T. G., Green, J. A., Gray, E. E., Xu, Y. & Cyster, J. G. Immune complex relay by subcapsular sinus macrophages and noncognate B cells drives antibody affinity maturation. *Nat Immunol* **10**, 786–793 (2009).
107. Carrasco, Y. R. & Batista, F. D. B Cells Acquire Particulate Antigen in a Macrophage-Rich Area at the Boundary between the Follicle and the Subcapsular Sinus of the Lymph Node. *Immunity* **27**, 160–171 (2007).
108. Holers, V. M. Complement and Its Receptors: New Insights into Human Disease. *Immunology* **32**, 433–459 (2014).

109. Mackay, I. R., Rosen, F. S. & Walport, M. J. Complement. *New Engl J Medicine* **344**, 1058–1066 (2001).
110. Ehrenstein, M. R. & Notley, C. A. The importance of natural IgM: scavenger, protector and regulator. *Nat Rev Immunol* **10**, 778–786 (2010).
111. Garred, P. *et al.* A journey through the lectin pathway of complement—MBL and beyond. *Immunol Rev* **274**, 74–97 (2016).
112. Turner, M. W. The role of mannose-binding lectin in health and disease. *Mol Immunol* **40**, 423–429 (2003).
113. Ip, W. K. E., Takahashi, K., Ezekowitz, R. A. & Stuart, L. M. Mannose-binding lectin and innate immunity. *Immunol Rev* **230**, 9–21 (2009).
114. Howard, M., Farrar, C. A. & Sacks, S. H. Structural and functional diversity of collectins and ficolins and their relationship to disease. *Semin Immunopathol* **40**, 75–85 (2018).
115. Takahashi, K. Lessons learned from murine models of mannose-binding lectin deficiency. *Biochem Soc T* **36**, 1487–1490 (2008).
116. Sheriff, S., Chang, C. Y. & Ezekowitz, R. A. B. Human mannose-binding protein carbohydrate recognition domain trimerizes through a triple α -helical coiled-coil. *Nat Struct Biol* **1**, 789–794 (1994).
117. Turner, M. W. Mannose-binding lectin: the pluripotent molecule of the innate immune system. *Immunol Today* **17**, 532–540 (1996).
118. Childs, R. A., Feizi, T., Yuen, C. T., Drickamer, K. & Quesenberry, M. S. Differential recognition of core and terminal portions of oligosaccharide ligands by carbohydrate-recognition domains of two mannose-binding proteins. *J Biological Chem* **265**, 20770–7 (1990).
119. Ringe, R. P. *et al.* Neutralizing Antibody Induction by HIV-1 Envelope Glycoprotein SOSIP Trimers on Iron Oxide Nanoparticles May Be Impaired by Mannose Binding Lectin. *J Virol* **94**, (2019).
120. Tarentino, A. L., Trimble, R. B. & Plummer, T. H. Chapter 5 Enzymatic Approaches for Studying the Structure, Synthesis, and Processing of Glycoproteins. *Methods Cell Biol* **32**, 111–139 (1989).
121. Tarentino, A. L. & Plummer, T. H. [4] Enzymatic deglycosylation of asparagine-linked glycans: Purification, properties, and specificity of oligosaccharide-cleaving enzymes from *Flavobacterium meningosepticum*. *Methods Enzymol* **230**, 44–57 (1994).
122. Keating, C. L. *et al.* Spontaneous Glycan Reattachment Following N-Glycanase Treatment of Influenza and HIV Vaccine Antigens. *J Proteome Res* **19**, 733–743 (2020).
123. Lövgren-Bengtsson, K. & Morein, B. *Methods in Molecular Medicine, Vaccine Adjuvants: Preparation Methods and Research Protocols*. vol. 42 (Humana Press, 2000).
124. Suan, D. *et al.* T Follicular Helper Cells Have Distinct Modes of Migration and Molecular Signatures in Naïve and Memory Immune Responses. *Immunity* **42**, 704–718 (2015).

125. Havenar-Daughton, C. *et al.* Cytokine-Independent Detection of Antigen-Specific Germinal Center T Follicular Helper Cells in Immunized Nonhuman Primates Using a Live Cell Activation-Induced Marker Technique. *J Immunol* **197**, 994–1002 (2016).
126. Dan, J. M. *et al.* A Cytokine-Independent Approach To Identify Antigen-Specific Human Germinal Center T Follicular Helper Cells and Rare Antigen-Specific CD4⁺ T Cells in Blood. *J Immunol* **197**, 983–993 (2016).
127. Wang, N., Qiu, C., Chen, M., Liu, T. & Wang, T. Covering Aluminum Oxide Nanoparticles with Biocompatible Materials to Efficiently Deliver Subunit Vaccines. *Nato Adv Sci Inst Se* **7**, 52 (2019).
128. Aebi, M. N-linked protein glycosylation in the ER. *Biochimica Et Biophysica Acta Bba - Mol Cell Res* **1833**, 2430–2437 (2013).
129. Schjoldager, K. T., Narimatsu, Y., Joshi, H. J. & Clausen, H. Global view of human protein glycosylation pathways and functions. *Nat Rev Mol Cell Bio* **21**, 729–749 (2020).
130. Bhat, A. H., Maity, S., Giri, K. & Ambatipudi, K. Protein glycosylation: Sweet or bitter for bacterial pathogens? *Crit Rev Microbiol* **45**, 82–102 (2019).
131. Schwarz, F. & Aebi, M. Mechanisms and principles of N-linked protein glycosylation. *Curr Opin Struc Biol* **21**, 576–582 (2011).
132. Spiro, R. G. Protein glycosylation: nature, distribution, enzymatic formation, and disease implications of glycopeptide bonds. *Glycobiology* **12**, 43R-56R (2002).
133. IWAMI, M. *et al.* A NEW IMMUNOMODULATOR, FR-900494: TAXONOMY, FERMENTATION, ISOLATION, AND PHYSICO-CHEMICAL AND BIOLOGICAL CHARACTERISTICS. *J Antibiotics* **40**, 612–622 (1987).
134. Kayakiri, H. *et al.* Structure of kifunensine, a new immunomodulator isolated from an actinomycete. *J Org Chem* **54**, 4015–4016 (1989).
135. Elbein, A. D., Tropea, J. E., Mitchell, M. & Kaushal, G. P. Kifunensine, a potent inhibitor of the glycoprotein processing mannosidase I. *J Biol Chem* **265**, 15599–15605 (1990).
136. Elbein, A. D., Kerbacher, J. K., Schwartz, C. J. & Sprague, E. A. Kifunensine inhibits glycoprotein processing and the function of the modified LDL receptor in endothelial cells. *Arch Biochem Biophys* **288**, 177–184 (1991).
137. Tarentino, A. L., Plummer, T. H. & Maley, F. The Release of Intact Oligosaccharides from Specific Glycoproteins by Endo- β -N-acetylglucosaminidase H. *J Biol Chem* **249**, 818–824 (1974).
138. Tai, T. *et al.* Structural studies of two ovalbumin glycopeptides in relation to the endo-beta-N-acetylglucosaminidase specificity. *J Biol Chem* **250**, 8569–8575 (1975).
139. Pierce, R. J., Spik, G. & Montreuil, J. Demonstration and cytosolic location of an endo-N-acetyl- β -D-glucosaminidase activity towards an asialo-N-acetyl-lactosaminic-type substrate in rat liver. *Biochem J* **185**, 261–264 (1980).

140. Kaminskas, L. M. *et al.* PEGylation of polylysine dendrimers improves absorption and lymphatic targeting following SC administration in rats. *J Control Release* **140**, 108–116 (2009).
141. Ryan, G. M. *et al.* PEGylated polylysine dendrimers increase lymphatic exposure to doxorubicin when compared to PEGylated liposomal and solution formulations of doxorubicin. *J Control Release* **172**, 128–136 (2013).
142. Rohner, N. A. & Thomas, S. N. Flexible Macromolecule versus Rigid Particle Retention in the Injected Skin and Accumulation in Draining Lymph Nodes Are Differentially Influenced by Hydrodynamic Size. *Acs Biomater Sci Eng* **3**, 153–159 (2016).
143. Reddy, S. T., Berk, D. A., Jain, R. K. & Swartz, M. A. A sensitive in vivo model for quantifying interstitial convective transport of injected macromolecules and nanoparticles. *J Appl Physiol* **101**, 1162–1169 (2006).
144. Howard, G. P. *et al.* Critical size limit of biodegradable nanoparticles for enhanced lymph node trafficking and paracortex penetration. *Nano Res* **12**, 837–844 (2019).
145. Blanco, E., Shen, H. & Ferrari, M. Principles of nanoparticle design for overcoming biological barriers to drug delivery. *Nat Biotechnol* **33**, 941–951 (2015).
146. Haurum, J. S. *et al.* Studies on the carbohydrate-binding characteristics of human pulmonary surfactant-associated protein A and comparison with two other collectins: mannan-binding protein and conglutinin. *Biochem J* **293**, 873–878 (1993).
147. Zhang, W. *et al.* Expression and characterization of recombinant chicken mannose binding lectin. *Immunobiology* **222**, 518–528 (2017).
148. Yassine, H. M. *et al.* Hemagglutinin-stem nanoparticles generate heterosubtypic influenza protection. *Nat Med* **21**, 1065–1070 (2015).
149. Sangesland, M. *et al.* Germline-Encoded Affinity for Cognate Antigen Enables Vaccine Amplification of a Human Broadly Neutralizing Response against Influenza Virus. *Immunity* **51**, 735-749.e8 (2019).
150. CASTLE, P. E. & MAZA, M. Prophylactic HPV vaccination: past, present, and future. *Epidemiol Infect* **144**, 449–468 (2016).
151. Schiller, J. & Lowy, D. Explanations for the high potency of HPV prophylactic vaccines. *Vaccine* **36**, 4768–4773 (2018).
152. Wang, J. W. & Roden, R. Virus-like particles for the prevention of human papillomavirus-associated malignancies. *Expert Rev Vaccines* **12**, 129–141 (2014).
153. Paavonen, J. *et al.* Efficacy of a prophylactic adjuvanted bivalent L1 virus-like-particle vaccine against infection with human papillomavirus types 16 and 18 in young women: an interim analysis of a phase III double-blind, randomised controlled trial. *Lancet* **369**, 2161–2170 (2007).

154. Yokomine, M. *et al.* Enhancement of humoral and cell mediated immune response to HPV16 L1-derived peptides subsequent to vaccination with prophylactic bivalent HPV L1 virus-like particle vaccine in healthy females. *Exp Ther Med* **13**, 1500–1505 (2017).
155. Damme, P. V. *et al.* Persistence of HBsAg-specific antibodies and immune memory two to three decades after hepatitis B vaccination in adults. *J Viral Hepatitis* **26**, 1066–1075 (2019).
156. Ho, J. K.-T., Jeevan-Raj, B. & Netter, H.-J. Hepatitis B Virus (HBV) Subviral Particles as Protective Vaccines and Vaccine Platforms. *Viruses* **12**, 126 (2020).
157. Romanò, L. *et al.* Hepatitis B vaccination. *Hum Vacc Immunother* **11**, 53–57 (2014).
158. Link, A. *et al.* Innate Immunity Mediates Follicular Transport of Particulate but Not Soluble Protein Antigen. *J Immunol* **188**, 3724–3733 (2012).
159. Wesener, D. A. *et al.* Recognition of microbial glycans by human intelectin-1. *Nat Struct Mol Biol* **22**, 603–610 (2015).
160. Schnaar, R. L. Glycans and glycan-binding proteins in immune regulation: A concise introduction to glycobiology for the allergist. *J Allergy Clin Immun* **135**, 609–615 (2015).
161. Zhou, J., Sun, X. Y. & Frazer, I. H. Glycosylation of Human Papillomavirus Type 16 L1 Protein. *Virology* **194**, 210–218 (1993).
162. Chen, Y.-J., Groves, B., Muscat, R. A. & Seelig, G. DNA nanotechnology from the test tube to the cell. *Nat Nanotechnol* **10**, 748–760 (2015).
163. Ke, Y., Castro, C. & Choi, J. H. Structural DNA Nanotechnology: Artificial Nanostructures for Biomedical Research. *Annu Rev Biomed Eng* **20**, 1–27 (2018).
164. Castro, C. E. *et al.* A primer to scaffolded DNA origami. *Nat Methods* **8**, 221–229 (2011).
165. Hong, F., Zhang, F., Liu, Y. & Yan, H. DNA Origami: Scaffolds for Creating Higher Order Structures. *Chem Rev* **117**, 12584–12640 (2017).
166. Jiang, Q., Liu, S., Liu, J., Wang, Z. & Ding, B. Rationally Designed DNA-Origami Nanomaterials for Drug Delivery In Vivo. *Adv Mater* **31**, 1804785 (2019).
167. Wagenbauer, K. F. *et al.* How We Make DNA Origami. *Chembiochem* **18**, 1873–1885 (2017).
168. Fan, S. *et al.* Create Nanoscale Patterns with DNA Origami. *Small* **15**, 1805554 (2019).
169. Shepherd, T. R., Du, R. R., Huang, H., Wamhoff, E.-C. & Bathe, M. Bioproduction of pure, kilobase-scale single-stranded DNA. *Sci Rep-uk* **9**, 6121 (2019).
170. Weaver, G. C. *et al.* In vitro reconstitution of B cell receptor–antigen interactions to evaluate potential vaccine candidates. *Nat Protoc* **11**, 193–213 (2016).

171. Villar, R. F. *et al.* Reconstituted B cell receptor signaling reveals carbohydrate-dependent mode of activation. *Sci Rep-uk* **6**, 36298 (2016).
172. King, L. B. & Freedman, B. D. B-lymphocyte calcium inFlux. *Immunol Rev* **231**, 265–277 (2009).
173. Perrault, S. D. & Shih, W. M. Virus-Inspired Membrane Encapsulation of DNA Nanostructures To Achieve In Vivo Stability. *Acs Nano* **8**, 5132–5140 (2014).
174. Mikkilä, J. *et al.* Virus-Encapsulated DNA Origami Nanostructures for Cellular Delivery. *Nano Lett* **14**, 2196–2200 (2014).
175. Lacroix, A., Edwardson, T. G. W., Hancock, M. A., Dore, M. D. & Sleiman, H. F. Development of DNA Nanostructures for High-Affinity Binding to Human Serum Albumin. *J Am Chem Soc* **139**, 7355–7362 (2017).
176. Hernandez-Garcia, A. *et al.* Precise Coating of a Wide Range of DNA Templates by a Protein Polymer with a DNA Binding Domain. *Acs Nano* **11**, 144–152 (2016).
177. Agarwal, N. P., Matthies, M., Gür, F. N., Osada, K. & Schmidt, T. L. Block Copolymer Micellization as a Protection Strategy for DNA Origami. *Angew Chem-ger Edit* **129**, 5552–5556 (2017).
178. Kiviaho, J. K. *et al.* Cationic polymers for DNA origami coating – examining their binding efficiency and tuning the enzymatic reaction rates. *Nanoscale* **8**, 11674–11680 (2016).
179. Ponnuswamy, N. *et al.* Oligolysine-based coating protects DNA nanostructures from low-salt denaturation and nuclease degradation. *Nat Commun* **8**, 15654 (2017).
180. Eeftens, J. M., Torre, J. van der, Burnham, D. R. & Dekker, C. Copper-free click chemistry for attachment of biomolecules in magnetic tweezers. *Bmc Biophys* **8**, 9 (2015).
181. Russell, D. M. *et al.* Peripheral deletion of self-reactive B cells. *Nature* **354**, 308–311 (1991).
182. Kouskoff, V. *et al.* Antigens Varying in Affinity for the B Cell Receptor Induce Differential B Lymphocyte Responses. *J Exp Med* **188**, 1453–1464 (1998).
183. Braun, U., Rajewsky, K. & Pelanda, R. Different sensitivity to receptor editing of B cells from mice hemizygous or homozygous for targeted Ig transgenes. *Proc National Acad Sci* **97**, 7429–7434 (2000).
184. Kouskoff, V., Lacaud, G. & Nemazee, D. T Cell-Independent Rescue of B Lymphocytes from Peripheral Immune Tolerance. *Science* **287**, 2501–2503 (2000).
185. Veneziano, R. *et al.* Designer nanoscale DNA assemblies programmed from the top down. *Science* **352**, 1534–1534 (2016).
186. Veneziano, R. *et al.* In vitro synthesis of gene-length single-stranded DNA. *Sci Rep-uk* **8**, 6548 (2018).
187. Rothemund, P. W. K. Folding DNA to create nanoscale shapes and patterns. *Nature* **440**, 297–302 (2006).

188. Schneider, C. A., Rasband, W. S. & Eliceiri, K. W. NIH Image to ImageJ: 25 years of image analysis. *Nat Methods* **9**, 671–675 (2012).
189. Tietjen, G. T., Bracaglia, L. G., Saltzman, W. M. & Pober, J. S. Focus on Fundamentals: Achieving Effective Nanoparticle Targeting. *Trends Mol Med* **24**, 598–606 (2018).
190. Alavi, M. & Hamidi, M. Passive and active targeting in cancer therapy by liposomes and lipid nanoparticles. *Drug Metabolism Personalized Ther* **34**, 20180032 (2019).
191. Swain, S., Sahu, P., Beg, S. & Babu, S. Nanoparticles for Cancer Targeting: Current and Future Directions. *Curr Drug Deliv* **13**, 1290–1302 (2016).
192. Amreddy, N. *et al.* Chapter Five Recent Advances in Nanoparticle-Based Cancer Drug and Gene Delivery. *Adv Cancer Res* **137**, 115–170 (2018).
193. Deng, Z., Kalin, G. T., Shi, D. & Kalinichenko, V. V. Nanoparticle Delivery Systems with Cell-Specific Targeting for Pulmonary Diseases. *Am J Resp Cell Mol* **64**, 292–307 (2021).
194. Ji, X., Gewurz, H. & Spear, G. T. Mannose binding lectin (MBL) and HIV. *Mol Immunol* **42**, 145–152 (2005).
195. Klein, N. J. Mannose-binding lectin: do we need it? *Mol Immunol* **42**, 919–924 (2005).
196. Shang, S., Chen, G., Shen, J., Yu, X. & Wang, K. The binding of MBL to common bacteria in infectious diseases of children. *J Zhejiang Univ Sci* **6B**, 53–56 (2005).
197. Thiel, S., Frederiksen, P. D. & Jensenius, J. C. Clinical manifestations of mannan-binding lectin deficiency. *Mol Immunol* **43**, 86–96 (2006).